FRIEDRICH-SCHILLER-
UNIVERSITÄT
JENA
Physikalisch-Astronomische Fakultät

Petawatt-Class Laser Optimization and Ultrashort Probe Pulse Generation for Relativistic Laser-Plasma Interactions

Issa Tamer

DISSERTATION
zur Erlangung des akademischen Grades
DOCTOR RERUM NATURALIUM (DR. RER. NAT.)

Vorgelegt dem Rat der
Physikalich-Astronomischen Fakultät
Friedrich-Schiller-Universität Jena
Geboren am 24.08.1992 in Chicago, IL, USA

Gutachter:

1. **Prof. Dr. Malte C. Kaluza**
   Institut für Optik und Quantenelectronik
   Friedrich-Schiller-Universität Jena
2. **Prof. Dr. Jens Limpert**
   Institut für Angewandte Physik
   Friedrich-Schiller-Universität Jena
3. **Prof. Dr. Franz X. Kärtner**
   Center for Free-Electron Laser Science
   Deutsches Elektronen Synchrotron (DESY) Hamburg

Tag der Disputation: 05.03.2020

Abstract

Advancements in high peak power laser development have resulted in laser systems capable of accelerating charged particles in a plasma to nearly the speed of light. For a comprehensive understanding and optimization of such interactions towards higher experimental yields, further enhancements in the laser system performance are required, along with a method that enables a direct view into the laser-induced plasma with a high spatial and temporal resolution. The work presented in this thesis details the results of multiple investigations regarding upgrades to the petawatt-class POLARIS laser and the development of a multi-beam ultrashort laser system for probing relativistic laser-plasma interactions at Friedrich Schiller University and Helmholtz Institute in Jena, Germany.

As laser pulse intensities are improved worldwide, the spatial, temporal, and temporal intensity contrast profiles of the pulses become increasingly crucial to the experimental performance and future scalability of the laser system. Where possible, an optimization of these parameters should be accomplished using simple, robust methods to avoid large-scale changes to the operational petawatt-class system. To improve the fluence homogeneity of the POLARIS laser pulse, a comprehensive spatio-temporal model of the pump-induced wavefront aberrations was constructed and the results of the verified model were applied to correct the heavily aberrated amplified beam profile in a joule-class multi-pass amplifier through a precise adjustment the pump distribution. Furthermore, the pulse duration post-CPA could be further compressed by a factor of 3 after near field SPM in a highly nonlinear material. In parallel to the spatial and temporal profile improvements, the temporal intensity contrast of the POLARIS laser pulse was enhanced 1000-fold using a plasma mirror.

An insight into the complex dynamics of relativistic laser-plasma interactions produced by the enhanced POLARIS laser can be achieved by employing an additional ultrashort laser system as an optical probe. For this purpose, a multi-beam ultrashort optical probing system, seeded by the POLARIS oscillator and pumped by a dedicated Yb:FP15-based CPA system, has been developed and installed within the petawatt-class laser system. The probing setup simultaneously offers two millijoule-level, nearly 100 fs laser pulses, along with a few-cycle laser pulse for high precision optical probing. Here, noncollinear optical parametric amplification (NOPA) is utilized to generate 20 μJ, 230 nm FWHM bandwidth pulses centered at 820 nm. The nonlinear BBO crystal is employed not only as the gain medium, but also as the pulse compressor, delivering near-FTL 11 fs pulses in a setup smaller than 40 cm × 40 cm. The temporal synchronization of the ultrashort probe pulses with the main POLARIS pulse are characterized using a live diagnostic system that monitors several orders of magnitude of delay. With the enhanced petawatt-class laser pulse, now equipped with a few-cycle optical probe, the intricate details of relativistic laser-plasma interactions can be revealed at the POLARIS laser system.

Zusammenfassung

Fortschritte bei der Entwicklung und Anwendung von Hochleistungslasern haben zu Lasersystemen geführt, die geladene Teilchen in einem Plasma auf nahezu Lichtgeschwindigkeit beschleunigen können. Für ein besseres Verständnis und eine Optimierung solcher Wechselwirkungen sind einerseits weitere Verbesserungen der Leistungsfähigkeit der verwendeten Lasersysteme erforderlich und andererseits Verfahren erwünscht, die einen direkten Blick in das laserinduzierte Plasma mit hoher räumlicher und zeitlicher Auflösung ermöglichen. Die in dieser Dissertation vorgestellten Arbeiten zeigen die Ergebnisse mehrerer Optimierungen des POLARIS Lasersystems und den Aufbau und die Untersuchung eines mehrstrahligen Ultrakurzpulslasersystems, welches zur Untersuchung der relativistischen Laser-Plasma-Wechselwirkungen als sogenannter Probelaser verwendet werden kann.

Da die zur Verfügung stehenden Spitzenintensitäten und Spitzenleistungen kontinuierlich steigen, werden auch die räumlichen, zeitlichen und zeitlichen Intensitätskontrastprofile der Laserpulse immer wichtiger für die experimentelle Leistungsfähigkeit und Skalierbarkeit der Lasersysteme. Wenn möglich, sollte eine Optimierung dieser Parameter mit einfachen, robusten Methoden durchgeführt werden, um weiträumige Änderungen an operativen Systemen zu vermeiden. Um die Nahfeldhomogenität der POLARIS-Laserpulse zu verbessern, wurde ein umfassendes raumzeitliches Modell der pumpinduzierten Wellenfrontaberrationen erstellt und die Ergebnisse des verifizierten Modells angewendet, um das stark deformierte verstärkte Strahlprofil in einem Multipass-Verstärker der Joule-Klasse durch eine genaue Anpassung der Pumpverteilung zu korrigieren. Darüber hinaus konnte die Pulsdauer eines verstärkten und komprimierten Laserpulses nach einer Nahfeld-Selbstphasenmodulation in einem hochgradig nichtlinearen Material um den Faktor 3 verkürzt werden. Parallel zu den räumlichen und zeitlichen Profilverbesserungen wurde der zeitliche Intensitätskontrast der POLARIS-Laserpulse mit einem Plasmaspiegel um das 1.000-fache erhöht.

Ein Einblick in die komplexe Dynamik relativistischer Laser-Plasma-Wechselwirkungen, die durch den weiterentwickelten POLARIS-Laser erzeugt werden, kann durch den Einsatz eines zusätzlichen ultrakurzen Laserpulses als optische Sonde (auf Englisch: *Probe*) gewonnen werden. Zu diesem Zweck wurde ein mehrstrahliges ultrakurzes optisches Probesystem entwickelt und innerhalb des POLARIS Lasersystems installiert. Der vom POLARIS Oszillator geseedete Probelaser bietet gleichzeitig zwei Laserpulse unterschiedlicher Zentralwellenlänge mit 100 fs Pulsdauer und millijoule Pulsenergien, sowie einen Laserpuls mit wenigen optischen Zyklen für hochpräzise zeitliche Messungen. Hierbei wird die nichtkollineare optische parametrische Verstärkung verwendet, um Laserimpulse mit einer Energie von 20 µJ, einer FWHM-Bandbreite von 230 nm bei einer Zentralwellenlänge von 820 nm zu erzeugen. Der nichtlineare BBO-Kristall wird nicht nur als Verstärkungsmedium, sondern auch als Pulskompressor verwendet, der die Impulse nahezu Fourier-limitiert auf eine Pulsdauer von 11 fs komprimiert. Die zeitliche

Synchronisation der ultrakurzen Probeimpulse mit den POLARIS Laserimpulsen wird durch ein Live-Diagnosesystem vermessen, dass mehrere Größenordnungen der zeitlichen Verzögerung überwacht. Mit den erheblich verbesserten POLARIS Laserimpulsen, der jetzt mit einem optischen Probelaser weniger optischer Zyklen ausgestattet sind, können die komplizierten Details relativistischer Laser-Plasma-Wechselwirkungen mit Hilfe des POLARIS-Lasersystems erforscht werden.

Contents

1 Introduction

Since the first experimental confirmation of laser operation in 1960[1], laser technology has become completely integrated into everyday life. The vast number of applications – including optical communications, laser-guided surgery, manufacturing, and even holography – have motivated scientists to continue conducting research on novel methods to produce more powerful lasers. Nowadays, laser systems at the highest level are capable[2,3] of generating focused intensities in excess of 10^{22} W/cm^2, through which plasmas can be formed directly in the laboratory upon interaction with any target material. With such experimental capabilities, an exciting branch of research has been revealed: relativistic laser-plasma physics and the laser-based acceleration of charged particles towards the speed of light.

Accessing and exploring new frontiers in relativistic laser plasma physics requires not only the further development and optimization of high peak and average power laser systems, but the simultaneous implementation of advanced optical diagnostics as well. The possible scientific, industrial, medical, and environmental applications enabled by research using intense laser systems have inspired a rapid increase in the number of petawatt-class (peak power $P \geq 200 \cdot 10^{12}$ W) lasers since the world's first in 1996[4], with over 50[2] systems currently in development or operational. With the successful demonstrations of advanced material processing[5], attosecond XUV generation[6], laser-induced relativistic electron beams[7], energetic laser-generated ion beams[8] for future use in cancer therapy, and the prospect of inertial confinement fusion[9] to produce a self-sustaining energy source, a substantial collective of funding sources and collaboration programs (e.g., LaserNetUS[10] in the USA, ELI[11] in Europe, and ASILS[12] in Asia) have been produced to invest in the worldwide advancement of this promising research field.

To upgrade present-day state-of-the-art laser systems and increase the understanding of the complex dynamics in laser-plasma interactions, many difficult challenges have yet to be overcome. An improvement in the laser performance requires addressing not only the laser pulse energy or pulse duration – typically on the order of joules (J) and femtoseconds (1 fs = 10^{-15} s), respectively, for petawatt-class lasers – but also the near field beam profile quality, focusability, repetition rate, and temporal intensity contrast of the laser system. Furthermore, the laser system optimization should be accomplished explicitly in the context of the desired laser-plasma interaction. For example, with the case of laser-based target normal sheath acceleration (TNSA) using µm-thick foils, a purposeful degradation of the temporal intensity contrast via the controlled introduction of a single pre-pulse may improve[13] the maximum achievable proton energies. Here, equipping the laser system with an ultrashort optical probe that is synchronized with the main laser pulse can reveal intricate details of the interaction with a high spatial and temporal resolution, allowing for a direct view into the laser-induced plasma and a powerful method to determine the optimum experimental laser parameters.

Within the scope of this work, multiple challenges regarding the spatial, temporal, and contrast improvement of the operational petawatt-class POLARIS[14] laser and the development of an ultrashort optical probing system at the Friedrich Schiller University and Helmholtz Institute in Jena, Germany, are investigated and addressed. First, theoretical concepts are presented that encompass the relevant design parameters of ultrashort laser pulses for both high intensity and probing applications. An introduction to the POLARIS laser system is given, along with a description of the issues that must be addressed – not only for POLARIS, but for state-of-the-art systems as well – to improve the laser performance.

The following chapter details the investigation on the limiting factors (spatial, temporal, and temporal intensity contrast) of a laser system at high peak powers. Here, thermal and electronic contributions to the wavefront aberrations induced by the pumping of laser-active materials result in a significant degradation of the near field profile, particularly for the case of large beam diameter, high energy (joule-class) multi-pass amplifiers. The high spatial frequencies present within the distorted, amplified beam can lead to permanent material damage; thus, the final fluence of the laser pulse must be reduced to avoid exceeding the limiting laser-induced damage threshold of the materials within the laser chain. Furthermore, the peak power of the laser is limited by the bandwidth-acceptance of the amplifiers and stretcher-compressor designs, which determine the shortest achievable pulse duration within the CPA system. Overcoming the challenges regarding the fluence and pulse duration must also be accompanied by a simultaneous improvement in the temporal intensity contrast. If left uncontrolled, the ASE pedestal, pre-pulses, and rising edge of the laser pulse can lead to a deterioration of the experimental performance of the laser. For these limiting factors of petawatt-class laser systems, investigations are conducted and solutions are presented.

The design and optimization of the multi-beam probing setup is described in chapter four. A POLARIS oscillator-seeded, Yb-based CPA system is utilized to produce two high energy probe pulses along with a few-cycle NOPA pulse, for use in various probing schemes in upcoming experimental campaigns. Femtosecond pulse synchronization techniques and their successful implementation for the pump (POLARIS main pulse) and probe (NOPA pulse) are also presented. The results of the investigations on petawatt-class laser optimization in conjunction with the ultrashort optical probing system described in this work are designated to improve and deepen the understanding of relativistic laser-plasma interactions worldwide.

2 Fundamentals

2.1 Description of an Ultrashort Laser Pulse

In a simple, one-dimensional representation[16], an ultrashort laser pulse in vacuum can be described as a coherent superposition of monochromatic plane waves with a carrier angular frequency ω_0 and wavenumber $k_0 = \frac{\omega_0}{c_0} = \frac{2\pi}{\lambda_0}$ for a wavelength λ_0, forming a total electric field $E(z,t)$:

$$E(z,t) = \frac{1}{2}A(z,t)\, e^{i(k_0 z - \omega_0 t)} + \text{c.c.} \tag{1}$$

propagating at the speed of light c_0 along the z-axis. The slowly varying envelope function $A(z,t)$ is an expression of the electric field amplitude and can be correlated to the intensity I of the laser pulse via:

$$I = \epsilon_0 c_0 \langle E(z,t)^2 \rangle = \frac{1}{2}\epsilon_0 c_0 \left| A(z,t) \right|^2 , \tag{2}$$

where ϵ_0 is the vacuum permittivity and the function $\langle E(z,t)^2 \rangle$ represents a temporal average of the electric field squared over an optical cycle with a period $T_0 = \frac{2\pi}{\omega_0}$. An ideal, although often not realized, form of the temporal profile of the field amplitude incorporates a Gaussian-shaped envelope[16] with a full-width at half-maximum (FWHM) pulse duration τ:

$$A(t) = A_0 e^{-2\ln 2 \left(\frac{t}{\tau}\right)^2}. \tag{3}$$

The distribution of laser pulse energy in the frequency domain can be expressed via a Fourier transform of the field amplitude, which then also takes on a Gaussian form with a full-width at half-maximum (FWHM) spectral bandwidth $\Delta\omega = 4\ln 2/\tau$:

$$A(\omega) = \frac{A_0 \tau}{2\sqrt{\ln 2}} e^{-2\ln 2 \left(\frac{\omega}{\Delta\omega}\right)^2}. \tag{4}$$

Multiplying the profile widths in the temporal (τ) and frequency (with $\Delta\nu = \frac{\Delta\omega}{2\pi}$) domains results in the time-bandwidth product TBP $= \tau \cdot \Delta\nu = \frac{2\ln 2}{\pi} = 0.441$ for a Gaussian pulse. Here, the constant value of the TBP shows that the pulse duration and spectral bandwidth are inversely related; hence, generating an ultrashort laser pulse with a Fourier transform limited (FTL) pulse duration of 100 fs (10^{-13} s) requires a spectral bandwidth (with $\Delta\nu = \frac{c_0 \cdot \Delta\lambda}{\lambda_L^2}$) of at least $\Delta\lambda =$ 15.6 nm at a central wavelength $\lambda_\mathrm{L} =$ 1030 nm. Due to the intense and broadband nature of ultrashort laser pulses, the impact of material dispersion and nonlinearity during propagation must be taken into account and, in some cases, can be used to control the temporal profile for the amplification of laser pulses towards petawatt-level peak powers.

Pulse Propagation in Dispersive Media

The evolution of an oscillating, linearly polarized electric field throughout propagation in a nonlinear and dispersive material is, according to Maxwell's equations, given as:

$$\nabla^2 E(z,t) - \frac{1}{c_0^2}\frac{\partial^2 E(z,t)}{\partial t^2} = \mu_0 \frac{\partial^2 P(z,t)}{\partial t^2}, \tag{5}$$

with μ_0 as the vacuum permeability and the polarization $P(z,t)$ as the material response to the incident electric field. For the case of a material with dispersion – and therefore, absorption, as seen from the Kramers-Kronig relations[17] – the polarization does not only depend on the instantaneous electric field. Here, the relationship between the electric field and the polarization is described by the susceptibility tensor χ and can be expressed in the frequency domain via:

$$P(z,\omega) = \epsilon_0 \left[\chi^{(1)}(\omega)E(z,\omega) + \chi^{(2)}(\omega)E^2(z,\omega) + \chi^{(3)}(\omega)E^3(z,\omega) + ...\right]. \tag{6}$$

The nonlinear second-order $\chi^{(2)}$ and third-order $\chi^{(3)}$ terms are responsible for a wide variety[17] of effects occurring in light-matter interactions, such as sum or difference frequency generation via wave-mixing, self-focusing, spectral broadening, and even nonlinear ultrabroadband amplification. For a sufficiently weak electric field, the nonlinear terms can be ignored and the wave equation (Eq. 5) can be rewritten via a Fourier transform as:

$$\nabla^2 E(z,\omega) = \frac{\omega^2}{c_0^2}\left[1 + \chi^{(1)}\right]E(z,\omega) = \frac{\omega^2}{c_0^2}\epsilon(\omega)E(z,\omega). \tag{7}$$

Here, the linear component of the susceptibility tensor is described by the dielectric permittivity $\epsilon(\omega) = 1 + \chi^{(1)}(\omega)$ of the material, which is related to the refractive index through $n(\omega) = \sqrt{\epsilon(\omega)}$. By inserting Eq. 1 in the frequency domain as a solution to Eq. 7, the dispersion relation can be derived:

$$k(\omega) = \frac{\omega}{c_0}\sqrt{\epsilon(\omega)} = \frac{\omega}{c_0}n(\omega), \tag{8}$$

which reveals the impact of the refractive index $n(\omega)$ of the material on the superposition of plane waves within the laser pulse, each with a frequency-dependent propagation constant $k(\omega)$ and angular frequency ω. As the laser pulse propagates within the material, it accumulates a frequency-dependent spectral phase $\phi(\omega) = k(\omega)z$ that results in dispersion, i.e., a different phase delay for each frequency. Due to the increasing bandwidth present within laser pulses of shorter and shorter pulse duration, the effect of material dispersion on the temporal profile of the pulse becomes less negligible.

To study the impact of dispersion on the temporal shape of the pulse, a Taylor expansion of the propagation constant $k(\omega)$ around the carrier frequency ω_0 can be performed[18]:

$$k(\omega) = k(\omega_0) + \left.\frac{\partial k}{\partial \omega}\right|_{\omega_0} \cdot (\omega - \omega_0) + \left.\frac{\partial^2 k}{\partial^2 \omega}\right|_{\omega_0} \cdot \frac{(\omega - \omega_0)^2}{2} + \left.\frac{\partial^3 k}{\partial^3 \omega}\right|_{\omega_0} \cdot \frac{(\omega - \omega_0)^3}{6} + \ldots . \tag{9}$$

Here, the speed at which the center of the pulse propagates through the material is given by the group velocity:

$$v_g = \left.\frac{\partial \omega}{\partial k}\right|_{\omega_0} = c_0 \left[n(\omega_0) + \omega_0 \left.\frac{\partial n}{\partial \omega}\right|_{\omega_0} \right]^{-1}, \tag{10}$$

which can be expressed in terms of a group delay (GD [fs] $= z/v_\mathrm{g}$) of the pulse after a propagation distance z. The frequency dependence of the group velocity (group velocity dispersion, GVD [fs^2/mm]) directly results in a different propagation time for each frequency within the pulse (group delay dispersion, GDD [fs^2])[18]:

$$\mathrm{GDD} = \mathrm{GVD} \cdot z = \left.\frac{\partial^2 k}{\partial^2 \omega}\right|_{\omega_0} \cdot z = \frac{\partial}{\partial \omega}\left(\frac{1}{v_\mathrm{g}}\right) \cdot z, \tag{11}$$

effectively separating the spectral components and stretching the pulse in time. As the GVD is an even-order term, both positive GVD (with the lower “red” frequencies propagating through the material faster than the higher “blue” frequencies) and negative GVD (blue faster than red) of the same amplitude will equally broaden the pulse. However, this is not the case for odd-order dispersion terms such as third order dispersion TOD [fs^3/mm]:

$$\mathrm{TOD} = \left.\frac{\partial^3 k}{\partial^3 \omega}\right|_{\omega_0} = \left.\frac{\partial \mathrm{GVD}}{\partial \omega}\right|_{\omega_0}, \tag{12}$$

in which the temporal profile is asymmetrically distorted and multiple trailing pulse replicas are formed. Examples of an ultrashort pulse propagating through the dispersive material YAG (yttrium aluminum garnate, $\mathrm{Y_3Al_5O_{12}}$) – a popular host material for high power laser systems – are given in Fig. 1. Here, the temporal intensity profile (top left figure) with a FWHM pulse duration of 10 fs is stretched by a factor of two via GVD (red, bottom left figure) after propagating through 1 mm of YAG. When considering only TOD (blue, bottom left figure), the pulse is stretched by a nearly factor of 1.5 and several additional pulses are generated near the trailing edge after 1 cm YAG. Here, a longer material length is chosen to depict the impact of TOD, which is smaller than that of GVD for YAG at the center wavelength of λ_L = 1030 nm. The odd-order nature of this term results in replica pulses on the leading edge for a TOD of opposite sign.

The effect of dispersive terms such as GVD and TOD on the pulse duration increases with the pulse bandwidth. Therefore, achieving the shortest FTL pulse durations τ_{FTL} requires an extensive effort in controlling the spectral phase $\phi(\omega)$. As seen Fig. 1 (bottom right), a 10 fs pulse passing through 100 mm YAG is stretched to nearly 2 ps, while an input 100 fs pulse experiences only a doubling of its pulse duration. Although the spectral phase of the pulse can be heavily modulated, the spectrum (Fig. 1, top right) in itself is not altered by the material dispersion. This is, however, no longer the case for intense, amplified laser pulses, through which nonlinear effects within the material also influence the spectrum of the ultrashort pulse.

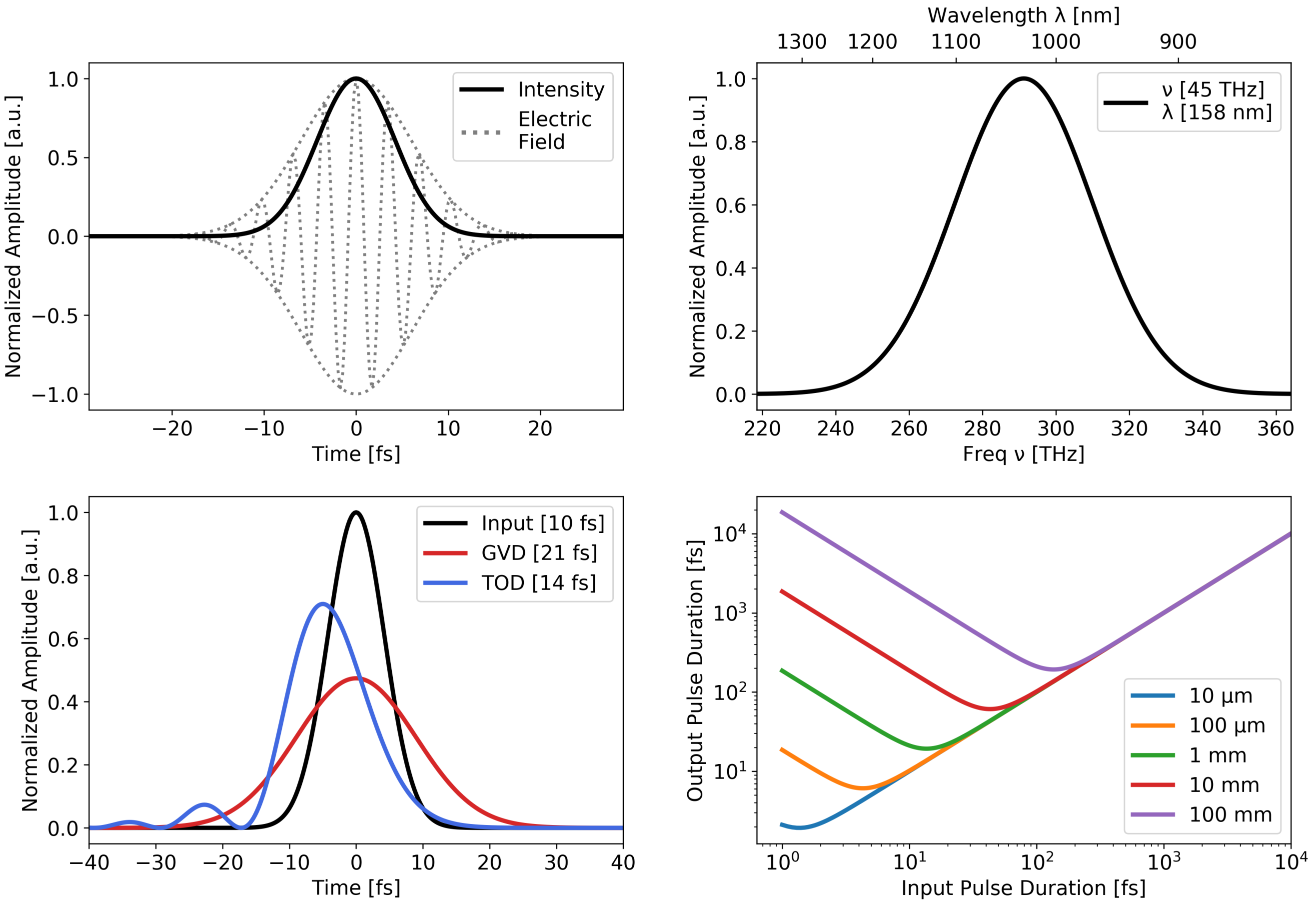

Figure 1: Temporal intensity profile (top left) of a 10 fs pulse, along with its electric field amplitude and oscillating components. In the top right figure, the spectrum is given as a function of frequency $\nu = \omega/2\pi$ (bottom axis) and wavelength $\lambda = c/\nu$ (top axis). Full width at half maximum (FWHM) values are given in brackets within the legends for both frequency and wavelength representations. The impact of pure GVD (red, 1 mm YAG) and pure TOD (blue, 1 cm YAG) on an initial 10 fs FWHM pulse is shown in the bottom left. The bottom right figure depicts the strong dependence of the output (stretched) pulse duration on the input pulse duration via GVD after propagation through various YAG crystal thicknesses.

2.2 Laser Pulse Amplification

To achieve petawatt-class peak powers, ultrashort laser pulses must be amplified – using techniques such as chirped pulse amplification[15] – within laser-active materials that can indirectly transfer energy from a pump laser to the seed laser, well into the joule regime (e.g., $100\,\mathrm{J} / 100\,\mathrm{fs} = 10^{15}\,\mathrm{W} = 1\,\mathrm{PW}$). For this purpose, the ideal laser-active material should fulfill the following criteria:

Absorption cross-section σ_{abs} : The absorption cross-section describes the probability, represented as a cross-sectional area, of photon absorption. A large σ_{abs} value for the pump photon allows for a more efficient absorption and a stronger excitement of the laser-active ions or atoms with a lower required pump intensity. Furthermore, a low σ_{abs} for the seed photon, where applicable, is desired for low seed absorption and an improvement in the laser gain factor.

Emission cross-section σ_{em} : The emission cross-section describes the probability, represented as a cross-sectional area, of photon emission. For ultrashort pulses, a large and broad σ_{em} is required to enable a high laser gain factor over the entire seed spectrum.

Radiative lifetime τ_{rad} : The radiative lifetime defines the time span of pump photon storage within the laser-active material, acting as a rough limit on the allowable pump pulse duration. Increasing the pump pulse duration significantly longer than the radiative lifetime does not necessarily contribute to the total excitement of the laser-active ions or atoms within the material, as the stored energy from the start of the pump pulse is radiated away before the end of the pump pulse arrives. For high energy storage, a long τ_{rad} is preferred to reduce the requirement on the pump pulse peak power. The radiative lifetime is often approximated[19] using the fluorescence lifetime $\tau_{\mathrm{fl}} = \frac{\tau_{\mathrm{rad}} \cdot \tau_{\mathrm{nr}}}{\tau_{\mathrm{rad}} + \tau_{\mathrm{nr}}}$ of the material, which includes the effects of non-radiative transitions τ_{nr} (e.g., multi-phonon relaxation).

Heat fraction η : Due to the spectral displacement between the absorption and emission cross-sections, an energy difference often exists between the pump and seed photons, referred to as the quantum defect, through which non-radiative transitions can occur that transform the excess energy into heat. The temperature change generated via the quantum defect can result in strong thermal gradients, thermally induced stress, and, ultimately, permanent material damage when the laser pulse energy or repetition rate f_{rep} is not adjusted accordingly. For a minimal thermal load within the laser-active material and an improvement in the maximum allowable average power $P_{\mathrm{avg}} = E \cdot f_{\mathrm{rep}}$ of the laser system, a low heat fraction $\eta = 1 - \lambda_{\mathsf{p}} / \lambda_{\mathsf{s}}$ is desirable.

The following brief introduction to laser amplification will show that the ideal material, which can fulfill all of the aforementioned criteria, does not exist. Instead, compromises must be made between these material properties – as they are, in some cases, inversely proportional to each other – depending on the specific design of the laser system.

A laser-active material, which contains a certain density of laser-active ions $N_{\mathrm{dop}}\,[\frac{\mathrm{ions}}{\mathrm{cm}^3}]$ or atoms, can exhibit laser transitions according to the population N_1 in a lower lasing level and N_2 in an upper lasing level. A laser-active ion in the lower lasing level can absorb an incident photon with an energy $h\nu$ and experience an excitation to an allowable upper energy level, where the energy of the photon matches the energy difference between the levels. Conversely, a laser-active ion in the upper lasing level can relax to the lower lasing level by releasing a photon with energy $h\nu$, either though stimulation from an additional incident photon or via spontaneous decay. The rate of change of the population of laser-active ions in the upper and lower lasing levels can be described by the laser rate equation[20]:

$$\frac{\partial N_1}{\partial t} = -\frac{\partial N_2}{\partial t} = A_{21}N_2 + (B_{21}N_2 - B_{12}N_1)\,\rho(\nu), \tag{13}$$

where $\rho(\nu)\,[\frac{\mathrm{J}}{\mathrm{m}^3\mathrm{s}}]$ is the spectral energy density of the radiation field and the Einstein coefficients B_{12}, B_{21}, and A_{21} represent the probability for absorption (loss), stimulated emission (gain), and spontaneous emission (decay), respectively. A steady-state solution of Eq. 13 reveals that lasing cannot occur in such a two-level system at thermal equilibrium – i.e., the laser-active ion population N_2 in the upper lasing level does not exceed the population N_1 in the lower level. Instead, three or even four levels are required, with a population in the pumping level that decays into the upper lasing level and / or a ground level that allows the lower lasing level to depopulate. An example of the energy level scheme for a Yb^{3+}-doped material, which can demonstrate characteristics similar to three-level or four-level systems depending on the temperature, is given in Fig. 2.

In real materials, the energy levels exhibit degeneracies (g_1 and g_2 for the lower and upper lasing levels, respectively), along with a non-discrete energy difference for a particular transition at a central frequency ν_0. Here, the emitted spectral distribution is described by the lineshape function $g(\nu,\nu_0)$, normalized such that $\int_0^\infty g(\nu,\nu_0)\,\mathrm{d}\nu = 1$, which can be broadened[16] due to homogeneous (e.g., Lorentzian-like lifetime broadening) and inhomogeneous (e.g., Gaussian-like Doppler broadening) mechanisms. Implementing the lineshape functions and the Einstein relations for the following coefficients $A_{21} = \tau_{rad}^{-1}$, $A_{21} = \frac{8\pi n^3 h\nu^3}{c_0^3}B_{21}$, and $g_2B_{21} = g_1B_{12}$ into the rate equation (Eq. 13) leads to the Füchtbauer-Ladenburg equation[21]:

$$\sigma_{\mathrm{em}}(\nu) = \frac{c_0^2}{8\pi n^2\nu^2\tau_{rad}} \cdot g(\nu,\nu_0), \tag{14}$$

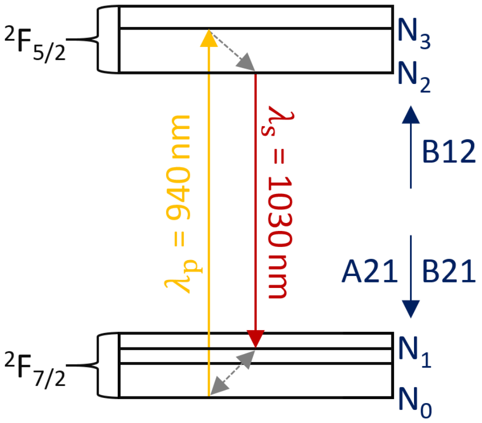

Figure 2: Example of an energy level scheme for a Yb^{3+}-doped material containing two lasing manifolds ($^2F_{5/2}$ and $^2F_{7/2}$) with a laser-active ion population N_3 for the pumping level (with pump wavelength λ_p), N_2 for the upper lasing (with seed wavelength λ_s), N_1 for the lower lasing level, and N_0 for the ground level. The Einstein coefficients B_{12}, B_{21}, and A_{21} describe the probability for absorption, stimulated emission, and spontaneous emission, respectively. The dashed gray lines indicate non-radiative transitions between the energy levels. Here, Yb^{3+} ions initially in the ground state have sufficient energy at room temperature to populate the lower lasing level and subsequently absorb an incident seed photon, thereby reducing the gain.

in which the emission cross section $\sigma_{\mathrm{em}}(\nu)$ [cm^2] is related to the radiative lifetime and emitted spectral distribution of the laser-active ion. Here, an inverse relationship is revealed between the strength of the emission cross-section and the pump energy storage (proportional to the radiative lifetime) of the material. Furthermore, due to the normalization of the lineshape function, a higher emission cross-section amplitude results in a narrower spectrum, thereby limiting the shortest achievable (FTL) pulse duration for an amplified pulse via spectral gain narrowing.

An additional compromise must be considered regarding the quantum defect, which is related to the ratio of the emission $\sigma_{\mathrm{em}}(\nu)$ and absorption $\sigma_{\mathrm{abs}}(\nu)$ cross-sections by the McCumber Relation[21]:

$$\frac{\sigma_{\mathrm{em}}(\nu)}{\sigma_{\mathrm{abs}}(\nu)} = \frac{Z_{\mathrm{l}}}{Z_{\mathrm{u}}} \cdot \exp\left[\frac{E_{\mathrm{ZPL}} - h\nu}{k_B T}\right], \tag{15}$$

where Z_{l} and Z_{u} describe the distribution of energy levels within the upper and lower sets of lasing levels ("manifolds") and E_{ZPL} corresponds to the energy difference between the lowest levels ("zero phonon line") of the upper and lower manifolds. For the case of Yb^{3+}-doped materials, with a quasi-three-level energy scheme at room temperature, the seed photon can be reabsorbed due to an overlapping of the emission and absorption bands, as seen in Fig. 3. As the energy of the seed photon approaches E_{ZPL}, the quantum defect decreases, but the seed absorption increases as well, thereby reducing the net gain. Shifting the energy of the pump photon towards that of the zero phonon line increases the probability of stimulated emission for the pump laser, which also reduces the net gain through a depopulation of the

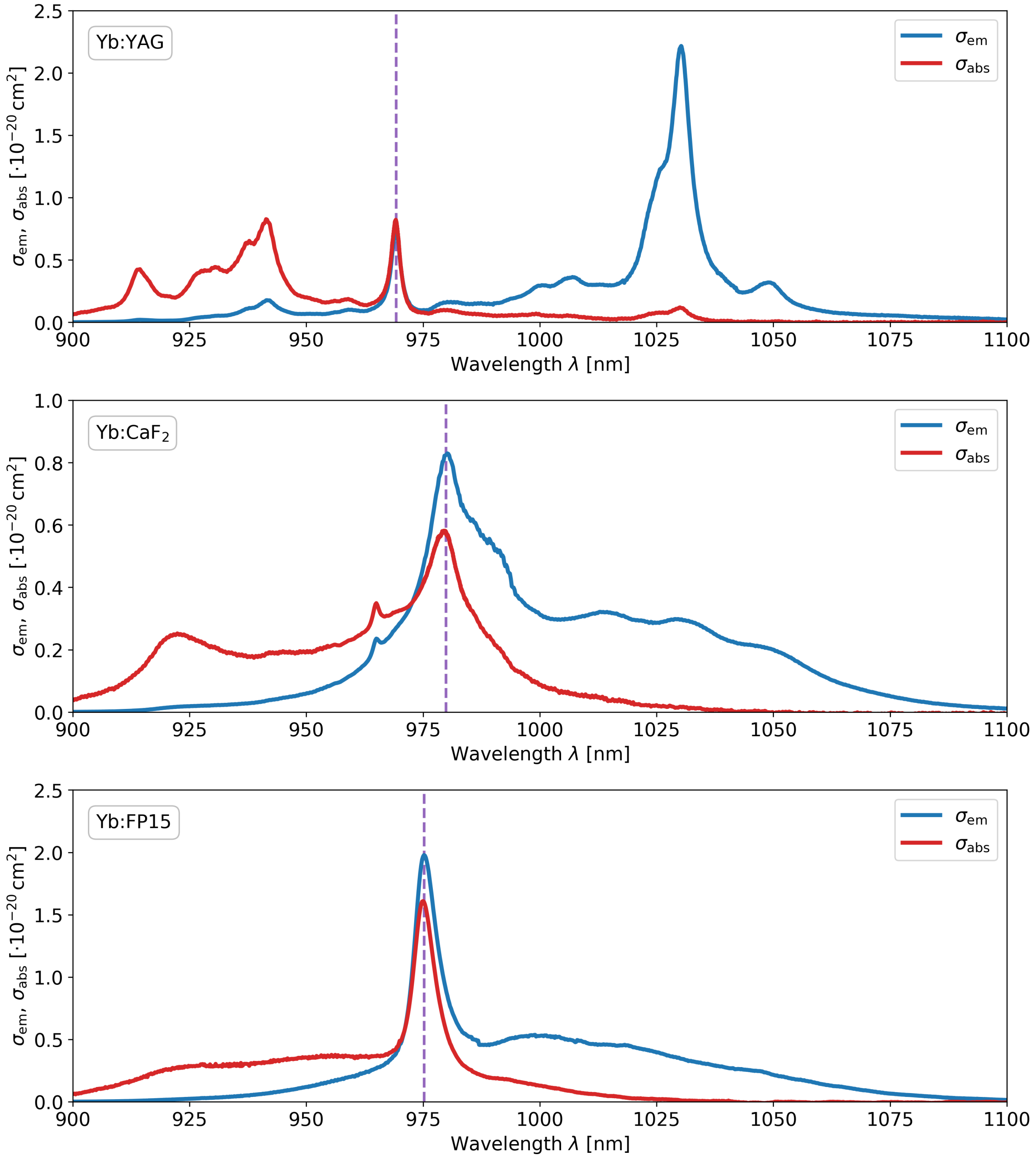

Figure 3: Emission and absorption cross-sections for Yb^{3+}-doped YAG (top), CaF$_2$ (center), and FP15 (bottom). The wavelengths corresponding to the zero phonon line transitions are given by the dashed purple lines.

upper lasing level by the pump and not the seed. Alternatively, separating the pump and seed wavelengths from the ZPL leads to an improvement in amplification for materials with overlapping absorption and emission cross-sections, but at the cost of additional thermal load due to the now increased quantum defect.

As the amplification of ultrashort pulses requires a broadband emission spectrum to maintain the spectral bandwidth, the laser-active material will either, from Eq. 14, exhibit a reduced emission cross-section amplitude (e.g., broadband Yb-doped materials) or a reduced radiative lifetime (e.g., Ti:Sapphire). Additionally, the high pump energies required to amplify such laser pulses to the joule-level result in a large deposition of heat within the laser-active material, increasing the importance of the magnitude of the quantum defect, which not only determines the maximum average power of the laser system, but also influences the generation of various sources of spatial profile degradation[22,23]. Here, Yb^{3+}-doped active materials[19] can demonstrate a low quantum defect (9%, compared to 33% for Ti:Sapphire[24]) with a long fluorescence lifetime in the ms-regime (µs for Ti:Sapphire), allowing for extended pump energy storage with the use of laser diodes. Furthermore, the Yb^{3+} ion can provide a high gain for short (10 ns[25]) pulses as well as a gain bandwidth sufficient to support pulse durations on the order of 100 fs[14]. The emission and absorption spectra of high gain (Yb:YAG[26]) and broadband (Yb:CaF_2[26,27] and Yb:FP15[28,29]) Yb^{3+}-doped materials are displayed in Fig. 3.

Optical Pumping and Gain

For the amplification of ultrashort pulses to the petawatt-level, high pump intensities are required to sufficiently excite a large population of the laser-active ions within the material to the upper lasing level. Here, a modified version[16] of the rate equation (Eq. 13):

$$\frac{\partial N_1}{\partial t} = -\frac{\partial N_2}{\partial t} = \frac{N_2}{\tau_{\mathsf{fl}}} + \Phi_{\mathsf{s}}\left(N_2 - N_1\right)\sigma_{\mathsf{em}}(\nu_{\mathsf{s}})c_0 - \Phi_{\mathsf{p}}\left(N_1 - N_2\right)\sigma_{\mathsf{abs}}(\nu_{\mathsf{p}})c_0, \tag{16}$$

including the pump (Φ_{p}) and seed (Φ_{s}) photon densities and the emission and absorption cross-sections, can be utilized to derive the pump intensity necessary to generate the desired population inversion $\beta = \frac{N_2}{N_{\mathsf{dop}}}$ and gain factor G for a given absorption coefficient $\alpha\,[\mathrm{cm}^{-1}] = \sigma_{\mathsf{abs}}(\nu_{\mathsf{p}}) \cdot N_{\mathsf{dop}}$. The pump depletion along the propagation direction (z-axis) within the active material can be approximated by the Lambert-Beer law:

$$\frac{\partial I(z)}{\partial z} = -\alpha I_{\mathsf{p}}(z) \tag{17}$$

for sufficiently low pump intensities. As the intensity approaches the pump saturation intensity of the active material:

$$I_{\mathsf{sat,p}} = \frac{h\nu_{\mathsf{p}}}{(\sigma_{\mathsf{em}}(\nu_{\mathsf{p}}) + \sigma_{\mathsf{abs}}(\nu_{\mathsf{p}})) \cdot \tau_{\mathsf{fl}}}, \tag{18}$$

the absorption within the material becomes saturated, as the population in the N_1 state is significantly reduced by the pump. Here, the pump intensity distribution in the saturation regime can be described via[16]:

$$\frac{\partial I_\mathrm{p}(z)}{\partial z} = -\frac{\alpha}{1+\frac{I_\mathrm{p}(z)}{I_\mathrm{sat,p}}} I_\mathrm{p}(z). \tag{19}$$

However, in reality, the absorption of the pump will also be directly affected by the evolution of the spatio-temporal inversion profile $\beta(z,t)$ within the active material. Determining the inversion-corrected pump depletion can be accomplished numerically with iterative solutions of the generated inversion $\beta(z,t)$[19]:

$$\frac{\partial \beta(z,t)}{\partial t} = I_\mathrm{p}(z,t) \cdot \frac{\lambda \cdot \sigma_\mathrm{abs}}{h \cdot c_0 \cdot \beta_\mathrm{eq}} \cdot \left(1 - \frac{\beta}{\beta_\mathrm{eq}}\right) - \frac{\beta_\mathrm{eq}}{\tau_\mathrm{fl}}, \tag{20}$$

and remaining pump intensity $I_\mathrm{p}(z,t)$:

$$\frac{\partial I_\mathrm{p}(z,t)}{\partial z} = -N_\mathrm{dop} \cdot \sigma_\mathrm{abs} \cdot \left(1 - \frac{\beta}{\beta_\mathrm{eq}}\right) \cdot I_\mathrm{p}(z,t), \tag{21}$$

where the equilibrium inversion:

$$\beta_\mathsf{eq}(\nu = \nu_\mathsf{p}) = \frac{\sigma_\mathsf{abs}(\nu_\mathsf{p})}{\sigma_\mathsf{em}(\nu_\mathsf{p}) + \sigma_\mathsf{abs}(\nu_\mathsf{p})}, \tag{22}$$

for the pump frequency ν_p is the maximum inversion achievable within the pumped active material. The comparison between the Lambert-Beer, saturated absorption, and inversion-corrected (numerically calculated) pump depletion models are given in Fig. 4 for a Yb:YAG crystal pumped near the saturation intensity of 25.8 $\frac{\mathrm{kW}}{\mathrm{cm}^2}$. The Lambert-Beer model was found to underestimate the remaining pump intensity by $\leq 12\%$, while the saturated absorption model overestimated by $\leq 7\%$ when compared to the numerical model including the spatio-temporal inversion profile.

To achieve amplification (gain factor $G_0 > 1$) for the seed laser, the generated inversion β must be greater the equilibrium inversion $\beta_\mathrm{eq}(\nu = \nu_\mathsf{s})$ for the seed frequency ν_s[19]:

$$\begin{aligned} G_0 &= \exp\left[N_\mathrm{dop} \cdot (\sigma_\mathrm{em}(\nu_\mathsf{s}) + \sigma_\mathrm{abs}(\nu_\mathsf{s})) \cdot (\beta - \beta_\mathrm{eq}(\nu_\mathsf{s})) \cdot z\right] \\ &= \exp\left[N_\mathrm{dop} \cdot (\sigma_\mathrm{em}(\nu_\mathsf{s})\beta - \sigma_\mathrm{abs}(\nu_\mathsf{s})(1-\beta)) \cdot z\right], \end{aligned} \tag{23}$$

such that the stimulated emission induced by the seed overcomes the seed reabsorption within the active material. In a similar fashion to the pump depletion saturation, the gain factor can

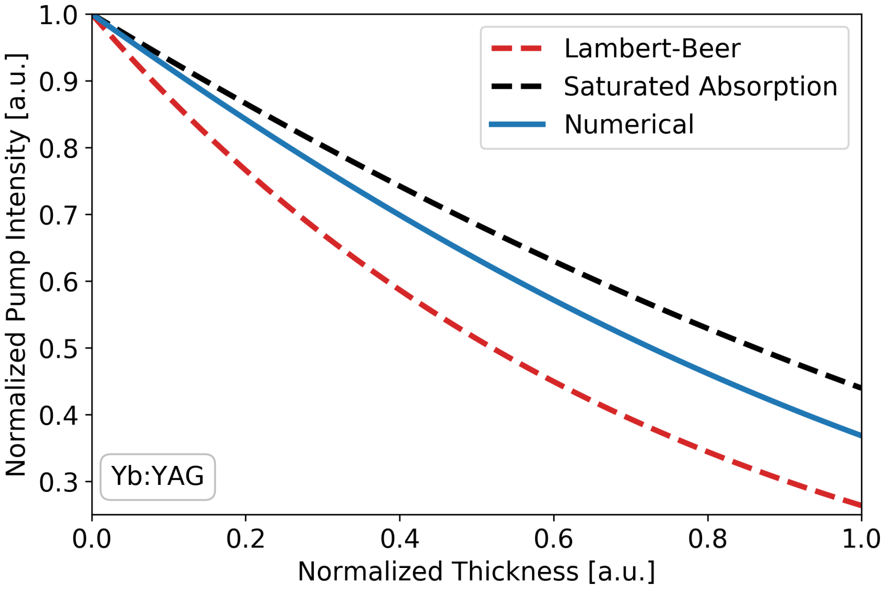

Figure 4: Numerical calculation of the normalized pump intensity within a Yb:YAG crystal in comparison to the Lambert-Beer and saturated absorption models.

be saturated as well. Here, the seed saturation fluence:

$$F_{\text{sat,s}} = \frac{h\nu_\text{s}}{\sigma_\text{em}(\nu_\text{s}) + \sigma_\text{abs}(\nu_\text{s})} \tag{24}$$

is the fluence at which the gain factor is reduced by $1/e$. For laser pulse amplification at high energies, multiple passes through the pumped active material are often required to achieve efficient energy extraction. When the input fluence F_s remains well below the seed saturation fluence $F_{\text{sat,s}}$, the total gain factor G for the amplifier after the final pass m can be approximated using $G = G_0^m$. However, for a large energy extraction (with an initial stored pump fluence F_p) by the seed pulse, the amplifier operates in saturation with a final gain factor[30,31]:

$$G = \left(1 + \frac{F_\text{p}}{F_\text{s}}\right) \cdot \left(1 + \frac{F_\text{p}}{F_\text{s}} \cdot \exp\left[-m \cdot \left(1 + \frac{F_\text{s}}{F_\text{p}}\right) \cdot \frac{F_\text{p}}{F_{\text{sat,s}}}\right]\right)^{-1}. \tag{25}$$

2.3 Nonlinear Ultrabroadband Amplification

2.3.1 Optical Parametric Amplification

The amplification of ultrashort pulses to joule-class energies and above is enabled by the use of broadband laser-active materials, in spite of their multiple disadvantages, such as a low gain (Yb-doped materials) or a short fluorescence lifetime (Ti:Sapphire). However, an alternative amplification scheme using nonlinear materials is available that offers the possibility of strong, broadband amplification with a significantly reduced number of material passes than in conventional amplifiers. Here, optical parametric amplification (OPA), a nonlinear three-wave mixing process, can be utilized to transfer energy from a narrowband, high energy pump pulse to a broadband, low energy seed pulse with a conversion efficiency of up to 20%[32,33]. Using these advantages, the OPA process has a become powerful tool for generating high energy, few-cycle laser pulses both for probing and high intensity applications, with state-of-the-art laser systems capable of 75 PW peak power currently in development[34].

Optical parametric amplification is a non-degenerate form of the $\chi^{(2)}$ difference frequency generation (DFG) process, in which a photon with energy $\hbar\omega_3$ is annihilated to produce two photons with lower energies $\hbar\omega_1$ and $\hbar\omega_2$. In such nonlinear three-wave mixing processes, the nonlinear second-order polarization term $P^{(2)}$ in Eq. 6 for the pump photon with an electric field E_3 oscillating at ω_3:

$$E_3(z,t) = A_3\, e^{i(k_3 z - \omega_3 t)} + \text{c.c.} \tag{26}$$

can be related to the amplitudes A_1 and A_2 of the fields oscillating at ω_1 and ω_2, respectively, via[17]:

$$P_3^{(2)} = 2\epsilon_0 \chi^{(2)} E^2 = 4\epsilon_0 d_{\text{eff}} E_1 E_2 = 4\epsilon_0 d_{\text{eff}} A_1 A_2\, e^{i((k_1+k_2)z - \omega_3 t)} + \text{c.c.}, \tag{27}$$

where $d_{\text{eff}} = \frac{1}{2}\chi^{(2)}$ is the effective nonlinearity scaling factor. Introducing the nonlinear polarization term for the E_3 field into Eq. 5 results in a coupled amplitude equation of the form[17]:

$$\begin{aligned} \left(\frac{\partial^2 A_3}{\partial z^2} + 2ik_3 \frac{\partial A_3}{\partial z} - k_3^2 A_3 + \frac{n^2(\omega_3)\omega_3^2}{c_0^2} A_3 \right) e^{i(k_3 z - \omega_3 t)} + \text{c.c.} \\ = -\frac{4 d_{\text{eff}} \omega_3^2}{c_0^2} A_1 A_2\, e^{i((k_3 - \Delta k)z - \omega_3 t)} + \text{c.c.}, \end{aligned} \tag{28}$$

with the wavevector (phase) mismatch between the three oscillating fields:

$$\Delta k = k_3 - k_2 - k_1 \tag{29}$$

as the dephasing term for the nonlinear mixing process.

Applying the slowly varying envelope approximation (SVEA) $|\frac{\partial^2 A(z,t)}{\partial z^2}| \ll |k\frac{\partial A(z,t)}{\partial z}|$ allows further simplification of Eq. 28 and the analogous coupled amplitude equations for the fields A_1 and A_2. The resulting coupled wave equations[17]:

$$\begin{aligned}\frac{\partial A_3}{\partial z} &= \frac{2id_{\mathrm{eff}}\omega_3^2}{k_3c_0^2}A_1A_2\,e^{-i\Delta kz}\\ \frac{\partial A_1}{\partial z} &= \frac{2id_{\mathrm{eff}}\omega_1^2}{k_1c_0^2}A_3A_2^*\,e^{i\Delta kz}\\ \frac{\partial A_2}{\partial z} &= \frac{2id_{\mathrm{eff}}\omega_2^2}{k_2c_0^2}A_3A_1^*\,e^{i\Delta kz}\end{aligned} \tag{30}$$

reveal the relationship between the spatial evolution of each field in the OPA process. As the fields propagates through the nonlinear medium, an energy exchange takes place that simultaneously alters the amplitudes of each field. Furthermore, in the event of an initially non-existent field (e.g., $A_2(0) = 0$), the OPA process will generate it instantaneously. As with standard OPA notation, the fields will now be defined according to their typical roles: pump $A_3 = A_\mathrm{p}$, signal $A_1 = A_\mathrm{s}$, and idler $A_2 = A_\mathrm{i}$.

An analytical solution to the coupled wave equations can be found in the simplified case, in which pump depletion is negligible $\left(\frac{\partial A_\mathrm{p}}{\partial z} = 0\right)$ and the initial idler amplitude A_i is zero:

$$A_\mathrm{s}(z) = A_\mathrm{s}(0)\left(\cosh\left(g_0z\right) - \frac{i\Delta k}{2g_0}\sinh\left(g_0z\right)\right)e^{i\Delta kz/2}, \tag{31}$$

where the small signal gain g_0 for OPA is defined as[17]:

$$g_0 = \sqrt{\kappa_\mathrm{s}\kappa_\mathrm{i}^* - \left(\frac{\Delta k}{2}\right)^2},\ \text{with}\ \kappa_{\mathrm{s,i}} = \frac{2id_{\mathrm{eff}}\omega_{\mathrm{s,i}}^2}{k_{\mathrm{s,i}}\,c_0^2}A_\mathrm{p}. \tag{32}$$

For the case of large gain ($g_0z \gg 1$) and no phase mismatch ($\Delta k = 0$), Eq. 31 reduces to:

$$A_\mathrm{s}(z) \approx A_\mathrm{s}(0)\frac{e^{g_0z}}{2}. \tag{33}$$

Here, analogously to the case of linear amplification, a gain factor G_0 (at material length L) for the parametric process can be defined, such that[32]:

$$G_0 = \frac{I_\mathrm{s}(L)}{I_\mathrm{s}(0)} \approx \frac{1}{2}\exp\left[\sqrt{\frac{2d_{\mathrm{eff}}^2\omega_\mathrm{s}\omega_\mathrm{i}}{c_0^3\epsilon_0n_\mathrm{p}n_\mathrm{s}n_\mathrm{i}}I_\mathrm{p}}\cdot L\right]. \tag{34}$$

The moderate intensities in the range of 1 - 100 $\frac{\mathrm{GW}}{\mathrm{cm}^2}$ required for OPA result in a substantial scaling of the parametric gain, as seen in Fig. 5, that the signal experiences as it propagates through the OPA crystal. To achieve such a promising amplification, however, the dephasing term Δk between the pump, signal, and idler must be minimized.

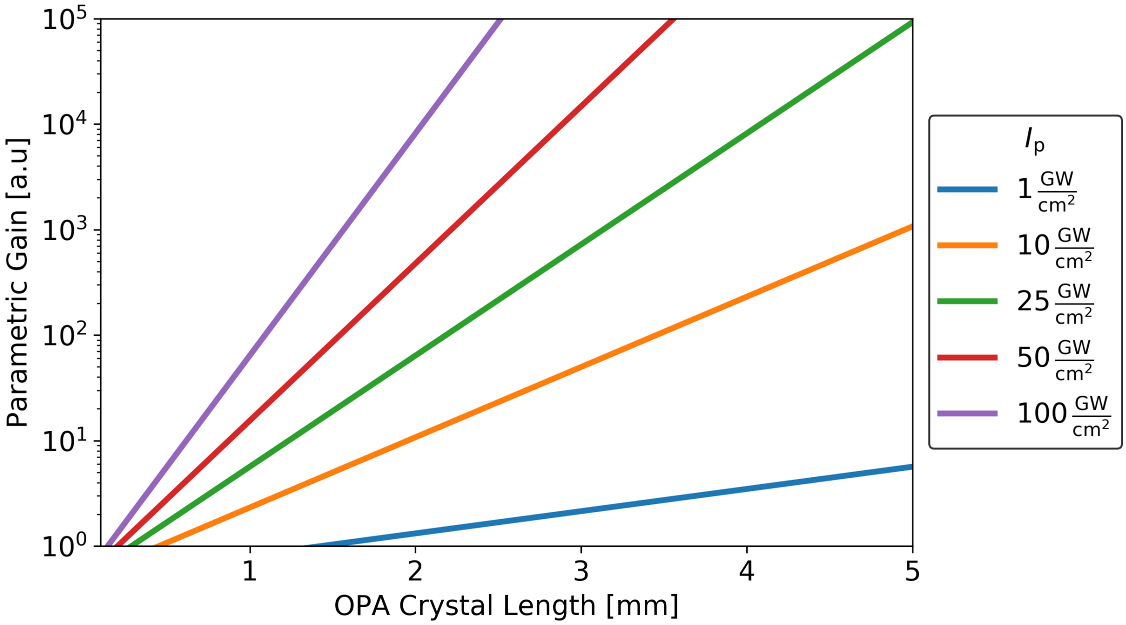

Figure 5: Upper limit of parametric gain (log scale) in an OPA crystal with pump intensity I_p ranging from 1 - 100 $\frac{\mathrm{GW}}{\mathrm{cm}^2}$. In reality, the parametric small signal gain does not exceed $\sim 10^5$, due to pump depletion, cascaded nonlinearities[35] that distort the OPA process, and damage threshold limitations at the amplified seed intensities.

2.3.2 Noncollinear Phase-Matching

Phase-matching for the OPA process can be accomplished collinearly for a small bandwidth by exploiting the birefringent properties, where available, of nonlinear crystals. In a "type I" phase-matching configuration[17], for example, the signal and idler propagate through the crystal with a polarization state perpendicular to the optical axis and experience the ordinary refractive index n_o. The pump, however, has a polarization parallel to the plane formed by the propagation direction $\vec{k}$ and the optical axis. Here, the refractive index n_e experienced by the pump can be tuned between the ordinary (n_o) and extraordinary (n_z) refractive indices of the crystal by changing the angle θ between $\vec{k}$ and the optical axis:

$$\frac{1}{n_\mathrm{e}^2(\theta)} = \frac{\cos^2\theta}{n_\mathrm{o}^2} + \frac{\sin^2\theta}{n_\mathrm{z}^2}. \tag{35}$$

With a proper angle tuning, the dephasing term Δk can be reduced to zero:

$$\Delta k = k_\mathrm{p} - k_\mathrm{s} - k_\mathrm{i} = \frac{\omega_\mathrm{p}}{c} n_\mathrm{p} - \frac{\omega_\mathrm{s}}{c} n_\mathrm{s} - \frac{\omega_\mathrm{i}}{c} n_\mathrm{i} = 0. \tag{36}$$

An example is given in Fig. 6, in which the refractive indices of the signal (n_s) and the idler (n_i) are determined by the crystal dielectric permittivity and input wavelengths. The cut-angle θ of the crystal with respect to the optical axis can be varied to match the refractive index $n_e(\theta)$ for the pump to the value n_p that is required to fulfill Eq. 36.

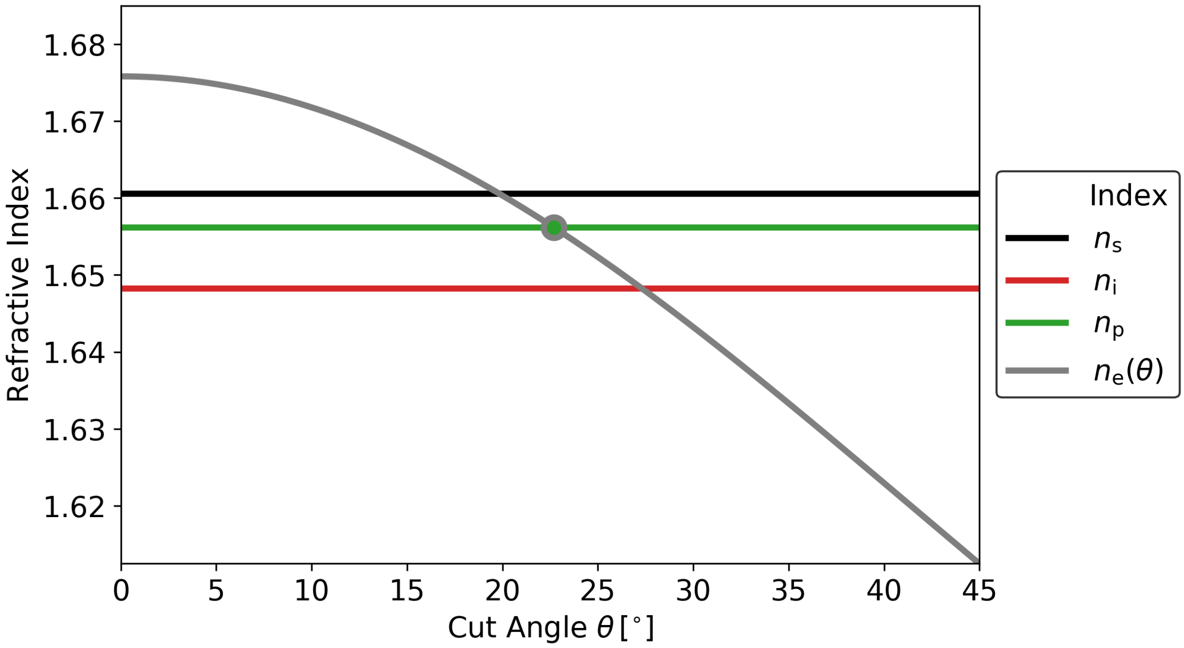

Figure 6: Birefringent phase-matching (type I) in a nonlinear OPA crystal. The refractive index of the pump laser is optimized via angle-tuning ($n_\mathrm{e}(\theta) = n_\mathrm{p}$) to fulfill $\Delta k = 0$.

To achieve phase matching over a broad bandwidth, the phase-mismatch Δk can be expanded around the signal frequency ω_s (with $\Delta k(\omega_\mathrm{s})$ equivalent to Eq. 36):

$$\Delta k(\omega) \approx \Delta k(\omega_\mathrm{s}) + \frac{\partial \Delta k}{\partial \omega_\mathrm{s}} \cdot (\omega - \omega_\mathrm{s}) + \frac{\partial^2 \Delta k}{\partial \omega_\mathrm{s}^2} \cdot \frac{(\omega - \omega_\mathrm{s})^2}{2} + \dots, \tag{37}$$

through which higher order terms can be compensated by introducing an additional set of controls – i.e., angles – between the three waves, thereby transforming the OPA process into a noncollinear interaction. The corresponding wavevector diagram is displayed in Fig. 7, with the phase-matching angle (cut-angle) θ, the pump-signal cross angle α, and the idler angle β, which is automatically generated to fulfill momentum conservation.

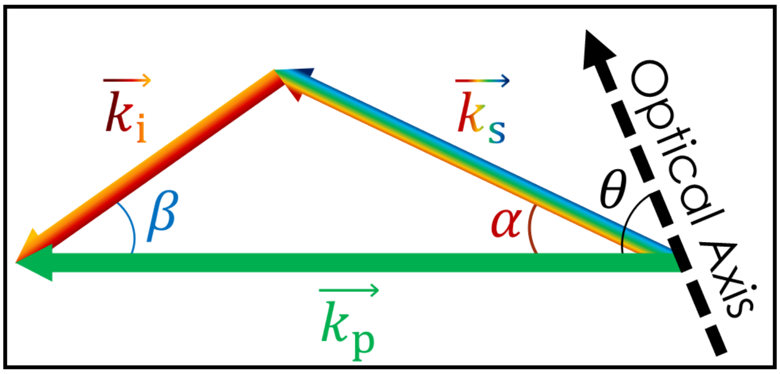

Figure 7: Noncollinear phase-matching diagram with pump-signal cross angle α, idler angle β, and phase-matching angle θ for the signal (k_s), idler (k_i), and pump (k_p) wavevectors.

To incorporate the nonlinear configuration into the phase-matching conditions, the 0^{th}-order term $\Delta k(\omega_{\mathrm{s}})$ in Eq. 37 must first be separated according to its parallel (with respect to the signal wavevector k_{s}) and perpendicular components. For noncollinear phase-matching, the equations:

$$\begin{aligned}\Delta k_{\parallel} &= k_{\mathrm{p}} \cos(\alpha) - k_{\mathrm{s}} - k_{\mathrm{i}} \cos(\alpha + \beta) = 0 \\ \Delta k_{\perp} &= k_{\mathrm{p}} \sin(\alpha) - k_{\mathrm{i}} \sin(\alpha + \beta) = 0\end{aligned} \tag{38}$$

must be fulfilled. To determine the optimum phase-matching and noncollinear angles, the above equations can be differentiated and equated to zero, thereby producing the condition for group velocity matching[36] ($v_{\mathrm{g,s}} = v_{\mathrm{g,i}}$, where $\frac{\partial \Delta k}{\partial \omega} = v_{\mathrm{g}}^{-1}$). Due to the large difference in wavelength between the signal and idler, the two waves propagate through the OPA crystal with different group velocities. This leads to a temporal separation and, consequently, a reduction in parametric gain for the signal, as energy from the pump must be utilized to generate a new idler at the temporal location of the signal and restart (as evident from Eq. 30) the OPA process. However, by angularly projecting the group velocity of the idler along the direction of the signal via[37]:

$$v_{\mathrm{g,s}} = v_{\mathrm{g,i}} \cos(\Omega), \text{ with } \Omega = \alpha + \beta, \tag{39}$$

the group velocity mismatch $(v_{g,s}^{-1} - v_{g,i}^{-1})$ between the signal and idler can be minimized, thereby also reducing the 1^{st}-order term $\frac{\partial \Delta k}{\partial \omega_s}$ of Eq. 37 and improving the phase-matching for a larger wavelength range. In Fig. 8, an example is given for group velocity matching in an OPA crystal with a center signal wavelength $\lambda_{\mathrm{s}} = 800\,\mathrm{nm}$. Introducing the idler angle (optimized for the center wavelength λ_{s}) reduces the group velocity mismatch at λ_{s} to zero

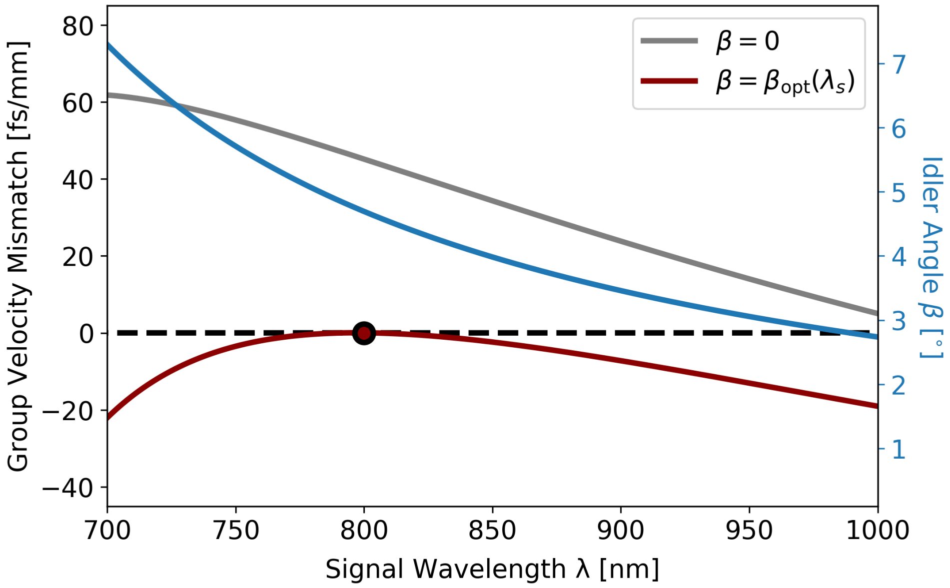

Figure 8: Group velocity matching between the signal and idler with idler projection angle β.

and the maximum magnitude between $700 - 1000$ nm by a factor of 3 (from 60 to 20 fs/mm).

Under the assumption of a non-existent idler at the start of the OPA crystal, the idler angle β is not chosen directly, but instead automatically generated when an angle α between the signal and pump is introduced. As the bandwidth of the idler is directly determined by the signal bandwidth via $\omega_\mathrm{p} = (\omega_\mathrm{s} \pm \Delta\omega) + (\omega_\mathrm{i} \mp \Delta\omega)$, the idler angle must also exhibit a frequency-dependence due to momentum conservation, such that $\beta = \beta(\omega)$. The experimentally tunable pump-signal cross angle α, however, can be assumed to be frequency-independent $\left(\frac{\partial\alpha}{\partial\lambda_\mathrm{s}} = 0\right)$, except in the event of a chirped broadband pump or spatially chirped signal. Here, the angle α can be derived from the phase-matching conditions above and given in two convenient, separable forms for a given center signal wavelength[37,38]:

$$\alpha = \sin^{-1}\left(k_\mathrm{i}\frac{\sin(\pi - \Omega)}{\sqrt{k_\mathrm{s}^2 + k_\mathrm{i}^2 + 2k_\mathrm{s}k_\mathrm{i}\cos(\Omega)}}\right) = \sin^{-1}\left(\frac{k_\mathrm{i}}{k_\mathrm{p}}\sqrt{1 - \left(\frac{v_\mathrm{g,s}}{v_\mathrm{g,i}}\right)^2}\right). \tag{40}$$

By optimizing α, the refractive index of the pump required for phase-matching can be determined by rearranging the above equation:

$$k_\mathrm{p} = \left(\frac{k_\mathrm{i}}{\sin(\alpha)}\sqrt{1 - \left(\frac{v_\mathrm{g,s}}{v_\mathrm{g,i}}\right)^2}\right) = \frac{\omega_\mathrm{p}}{c}n_\mathrm{p} \tag{41}$$

to solve for the phase-matching angle θ using Eq. 35 (with $n_\mathrm{p} = n_\mathrm{e}(\theta)$):

$$\theta = \sin^{-1}\left(\frac{n_\mathrm{p,z}}{n_\mathrm{p}}\sqrt{\frac{n_\mathrm{p,o}^2 - n_\mathrm{p}^2}{n_\mathrm{p,o}^2 - n_\mathrm{p,z}^2}}\right). \tag{42}$$

In Fig. 9, a set of optimized pump-signal cross angles α is given for various center signal wavelengths (shown by the black circles within the plot), from which the phase-matching angles could be determined. Using a pump wavelength of $\lambda_\mathrm{p} = 515$ nm, the angle $\alpha = 2.6^\circ$ at $\lambda_\mathrm{s} = 800$ nm provides a phase-matching angle of approximately 24.5° that remains nearly constant over the range from $700 - 1000$ nm, indicating that the condition for broadband phase-matching can be readily fulfilled with this configuration.

A further increase in the phase-matching bandwidth requires the compensation of the 2nd-order term $\frac{\partial\Delta k}{\partial\omega_\mathrm{s}}$ of Eq. 37. The phase-matching condition therefore becomes[37]:

$$\frac{\partial^2 k_\mathrm{s}}{\partial\omega_\mathrm{s}^2}\cdot\cos(\Omega(\omega_\mathrm{s})) + \frac{\partial^2 k_\mathrm{i}}{\partial\omega_\mathrm{i}^2} - k_i\left(\frac{\partial\Omega}{\partial\omega_\mathrm{s}}\right)^2 = 0, \tag{43}$$

which can be accomplished by introducing an additional control parameter for the variable $\Omega(\omega) = \alpha + \beta(\omega)$. Here, a frequency-dependence on the pump-signal cross angle ($\alpha = \alpha(\omega)$) can be implemented via a spatially chirped signal or a chirped broadband pump.

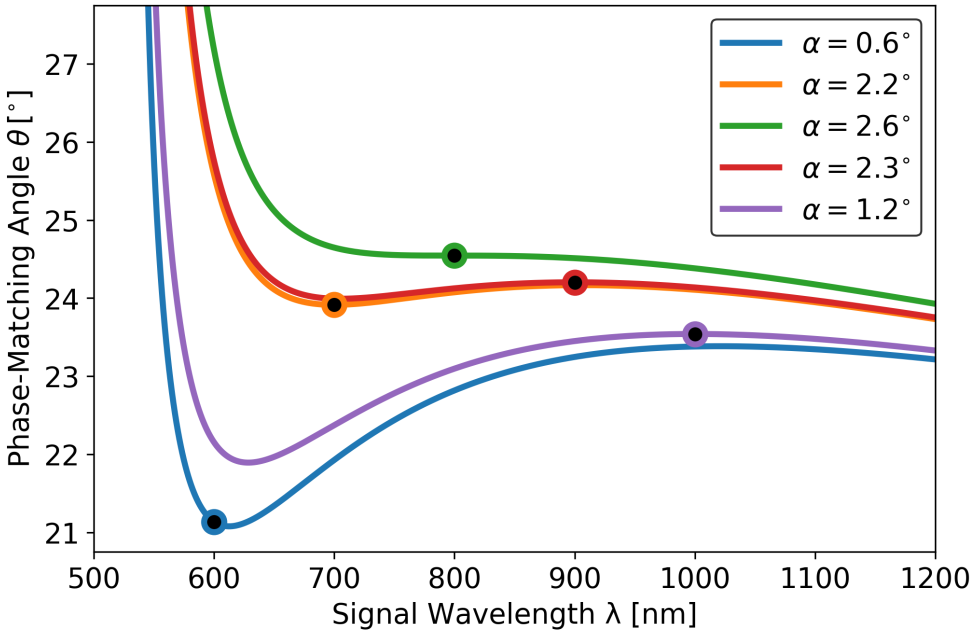

Figure 9: Set of optimized pump-signal cross angles α at multiple design wavelengths (black circles within the plot), from which the phase-matching angles could be determined. The angle $\alpha = 2.6\,^\circ$ at $\lambda_s = 800\,\text{nm}$ resulted in a constant phase-matching angle over the broadest wavelength range throughout the various configurations.

With the above considerations, the coupled wave equations (Eq. 30) can be adjusted to include the noncollinear configuration[32]:

$$\begin{aligned}
\frac{\partial A_\text{p}}{\partial z} + \frac{i}{2}\text{GVD}_\text{p}\frac{\partial^2 A_\text{p}}{\partial t^2} &= \frac{2id_\text{eff}\omega_\text{p}^2}{k_\text{p}c^2}A_\text{s}A_\text{i}\, e^{-i\Delta kz} \\
\frac{\partial A_\text{s}}{\partial z} + \left(\frac{1}{v_\text{g,s}\cos(\alpha)} - \frac{1}{v_\text{g,p}}\right)\frac{\partial A_\text{s}}{\partial t} + \frac{i}{2}\text{GVD}_\text{s}\frac{\partial^2 A_\text{s}}{\partial t^2} &= \frac{2id_\text{eff}\omega_\text{s}^2}{k_\text{s}c^2}A_\text{p}A_\text{i}^*\, e^{i\Delta kz} \\
\frac{\partial A_\text{i}}{\partial z} + \left(\frac{1}{v_\text{g,i}\cos(\beta)} - \frac{1}{v_\text{g,p}}\right)\frac{\partial A_\text{i}}{\partial t} + \frac{i}{2}\text{GVD}_\text{i}\frac{\partial^2 A_\text{i}}{\partial t^2} &= \frac{2id_\text{eff}\omega_\text{i}^2}{k_\text{i}c^2}A_\text{p}A_\text{s}^*\, e^{i\Delta kz}.
\end{aligned} \tag{44}$$

Here, the dispersion terms – in particular, GVD (Eq. 11) – must also be accounted for due to the ultrashort and broadband nature of the interaction. The above modified coupled wave equations can be solved iteratively for the three interacting waves using the RK4IP method[39] (described in section 2.4.3), where transformations between the time and frequency domains can be implemented to efficiently evaluate the nonlinear and dispersion operators. Numerically modeling the noncollinear optical parametric amplification (NOPA) process grants access to further tools for optimization, as detailed in section 4.3.3, including varying the pump-signal temporal delay or utilizing the OPA crystal itself as a pulse compressor. With a wide range of configurations that provide a broad amplification bandwidth at high gain for various wavelength regimes, NOPA is a promising method for the improvement of high peak power laser systems, as well as the generation of ultrashort probe pulses for relativistic laser-plasma interactions.

2.4 Limiting Factors of a Petawatt-Class Laser System

To achieve improvements in experimental results involving relativistic laser-plasma interactions, such as higher electron and proton cutoff energies, several limiting factors for laser systems at the petawatt-class must be understood and addressed. The performance of the laser system can be described in part by the laser pulse energy, repetition rate, spatial beam quality, focusability, pulse duration, and temporal intensity contrast. In the following sections, a brief theoretical overview is given that discusses the limitations on these parameters.

2.4.1 Intensity: B-Integral and the LIDT

The direct amplification of ultrashort pulses towards the high energies required for petawatt-class operation is prevented by the manifestation of nonlinear laser-matter interactions and, ultimately, the laser-induced damage threshold (LIDT) in the optical elements of the laser system itself. As the amplified laser pulse propagates through a large total length of optical materials (e.g., laser-active materials, Pockels cell crystals, and lenses) within the laser chain, the laser pulse experiences an accumulation of nonlinear phase due to the nonlinear refractive index of each element. A figure of merit for the total nonlinear phase is the B-Integral[4]:

$$B = \frac{2\pi}{\lambda} \int_0^L n_2 \, I \, \mathrm{d}z, \tag{45}$$

which is dependent not only on the material thickness L and nonlinear refractive index n_2, but also on the intensity $I(x, y, t)$ of the laser pulse. In real systems, the inhomogeneous[14] intensity profiles result in a spatially and temporally varying nonlinear phase accumulation. For the case of a Gaussian-like spatial profile, the magnitude of the B-Integral is higher in the center of the beam than on the edges, leading to a form for the nonlinear spatial phase resembling that of a positive lens. As a consequence, the laser beam undergoes self-focusing[20], thereby increasing the likelihood of permanent material damage as it propagates towards the remaining optical components within the laser chain. Analogously, the inhomogeneous temporal profile – particularly for chirped pulses, where the optical frequencies are distributed along the stretched pulse duration – leads to a variation in the nonlinear phase amplitude for each spectral component in the form of high frequency spectral phase modulations[40]. Here, recovering the ultrashort pulse duration requires the use of advanced optical components (e.g., acousto-optic programmable dispersive filters[41]) that often exhibit limited optical transmission, resulting in a significant reduction of the output laser energy. To prevent the spatio-temporal intensity profile degradations enabled by a large B-Integral ($B \geq 1$ radian) throughout the laser system, a reduction in the laser pulse intensity is often necessary.

Ultimately, the maximum achievable pre-focus intensity is limited by the laser-induced damage threshold (LIDT), given in units of fluence (J/cm^2) for pulsed lasers[42]. In the nanosecond regime, high energy pulses can be partially absorbed by materials in the beam path and cause permanent damage[43] due to carrier-phonon scattering, dielectric breakdown, or thermally induced stress. In the ultrashort regime, however, electrons can be directly stripped from the material via multiphoton, tunneling, or avalanche ionization. The multiple sources of laser-induced damage results in various LIDT scalings[42] for each material, particularly according to the pulse duration τ and wavelength λ. Preventing damage for all optical components within the laser system can be accomplished by increasing the beam diameter via magnification and the pulse duration using dispersion. After laser pulse amplification, the chirped pulse can be compressed[15] before being focused to achieve a high intensity on-target.

2.4.2 Spatial: Pump-Induced Wavefront Aberrations

The output energy of a high peak power laser system is limited by its spatial beam quality, due to the laser-induced damage threshold (LIDT) of the laser-active materials. Here, large beams with a homogeneous energy distribution are desired to avoid permanent material damage, particularly for energy extraction above the joule-level. During the amplification process, however, the pumped active material imprints an inhomogeneous spatial phase profile[23] in the form of varying optical path differences (OPDs) onto the wavefront of the incident laser pulse. The large propagation distances typical in high energy non-imaging multi-pass amplifiers[14] allow the wavefront aberrations to distort the spatial beam profile, destroying the beam homogeneity and generating localized regions with high energy densities. To ensure that the local fluence remains below the damage threshold, an upper limit must be placed on the achievable final energy of the laser pulse. Therefore, the pump-induced wavefront aberrations limit not only the spatial beam quality, but the final energy and focusability as well. A comprehensive understanding of the thermal and electronic contributions to the pump-induced wavefront aberrations can therefore enable a further energy scaling of petawatt-class laser systems.

Thermal Contributions

Pumping a laser-active material induces a change in the temperature distribution due to the quantum defect, resulting in a modification of the refractive index, stress, and thermal expansion. The combined effect leads to an OPD profile ϕ_{th} that the laser pulse to be amplified experiences as it propagates through the active material[22]:

$$\phi_{\mathrm{th}}(\vec{r},t) = \left[\frac{\mathrm{d}n}{\mathrm{d}T} + 2n_0^3\alpha_T C_r' + (n_0-1)(1+\nu)\alpha_T\right] \cdot \langle T(\vec{r},t) - T_0\rangle L. \tag{46}$$

The spatial form of the thermal contributions to the pump-induced wavefront aberrations is given by the shift in the temperature distribution $T(\vec{r},t)$ from the initial temperature T_0 due to pumping – averaged over the length L of the active material – at the time of laser energy extraction (typically at the end of the pump pulse). The magnitude of the inhomogeneous OPD profile scales with the total thermo-optic coefficient χ[22], which is described by the three terms enclosed within the brackets in Eq. 46. The first and last component of the total thermo-optic coefficient are the dn/dT and thermal expansion $(n_0 - 1)(1+\nu)\alpha_T$ terms, with the initial refractive index n_0 at temperature T_0, Poisson's ratio ν, and coefficient of thermal expansion α_T, which are typically well-characterized in literature for common laser-active materials. However, the amplitude of the stress component, with photoelastic constant[22]:

$$C_r' = \frac{-(1+\nu)(9p_{11} + 15p_{12})}{48}, \tag{47}$$

is often unknown and must be experimentally determined[23] for the doped laser-active materials. Where possible, the photoelastic constant C_r' can be calculated using a reduced form (via crystal symmetry properties[17,44]) of the elasto-optic tensor. For the (undoped) host material CaF$_2$ (cubic crystal of class m3m[45]), the tensor can be simplified to contain three independent variables:

$$\begin{bmatrix} p_{11} & p_{12} & p_{12} & 0 & 0 & 0 \\ p_{12} & p_{11} & p_{12} & 0 & 0 & 0 \\ p_{12} & p_{12} & p_{11} & 0 & 0 & 0 \\ 0 & 0 & 0 & p_{44} & 0 & 0 \\ 0 & 0 & 0 & 0 & p_{44} & 0 \\ 0 & 0 & 0 & 0 & 0 & p_{44} \end{bmatrix},$$

where the elasto-optic coefficients p_{11}, p_{12}, and p_{44} can be determined from measurements of the stress-optic and stiffness coefficients q_{mr} and c_{rn}, respectively, via[44] $p_{\mathrm{mn}} = \sum_{r=1}^{6} q_{\mathrm{mr}} \cdot c_{\mathrm{rn}}$. Employing the tensor symmetry given above, the three independent elasto-optic coefficients can be calculated using[44]:

$$\begin{cases} p_{11} = q_{11} \cdot c_{11} + 2q_{12} \cdot c_{12} \\ p_{12} = q_{11} \cdot c_{12} + q_{12}\left(c_{11} + c_{12}\right) \\ p_{44} = q_{44} \cdot c_{44}, \end{cases} \tag{48}$$

resulting in the values summarized in Table 1 for the stress-induced component ($\chi_{\mathrm{str}} = 2n_0^3 \alpha_T C_r'$) of the total thermo-optic coefficient for undoped CaF$_2$. Here, NIST[46] values for the stress-optic coefficients q_{mn} (measured from $\lambda = 254 - 546\,\mathrm{nm}$) are utilized along with stiffness coefficients[45] $c_{11} = 1.653 \cdot 10^9$ Pa, $c_{12} = 0.445 \cdot 10^9$ Pa, and $c_{11} = 0.338 \cdot 10^9$ Pa to determine the value of χ_{str}. Using extrapolated values for the stress-optic coefficients at the POLARIS laser center wavelength of 1030 nm, a change in χ_{str} of nearly 40% is revealed, purely based on the wavelength dependence. Further considering the anisotropy[47] of CaF$_2$ and the disruption[48] of the lattice structure via Yb^{3+}-doping ensures that a simple imple-

Table 1: Wavelength dependence of the stress-induced thermo-optic coefficient χ_{str}

λ [nm]	q_{11} [Pa^{-1}]	q_{12} [Pa^{-1}]	q_{44} [Pa^{-1}]	p_{11}	p_{12}	p_{44}	χ_{str} [K^{-1}]
546[46]	-0.38·10^{-12}	1.15·10^{-12}	0.75·10^{-12}	0.045	0.226	0.0254	-10.7·10^{-6}
1030*	-0.48·10^{-12}	0.84·10^{-12}	0.78·10^{-12}	0.0240·10^{-2}	0.156	0.0264	-6.6·10^{-6}

*Extrapolated using NIST[46] values.

mentation of the available elasto-optic coefficients will result in an incorrect estimation of the thermal contributions to the pump-induced wavefront aberrations. Here, an experimental characterization of the total thermo-optic coefficient must be conducted using, e.g., a comprehensive, benchmarked thermal profile simulation.

Thermal Profile Modeling

The full 3D spatio-temporal thermal profile of a pumped active material in an amplifier operating in the linear regime (i.e., far from gain saturation) can be numerically modeled by solving the heat transfer equation[22]:

$$\rho C_p \frac{\partial T(x,y,z,t)}{\partial t} - K_{th}\nabla^2 T(x,y,z,t) = \eta_h \alpha I(x,y,t) A(z,t), \tag{49}$$

which describes the dependence of the pump-induced change in the thermal profile on the pump and material parameters. For laser-active materials, the doping level must also be considered, due to the large influence[49] of doping on the thermo-mechanical material properties. The left-most term of Eq. 49 shows that the specific heat capacity C_p $\left[\frac{\mathrm{J}}{\mathrm{kg{\cdot}K}}\right]$ – approximated using the Debye model[50], which takes the doping concentration into account – and density ρ $\left[\frac{\mathrm{kg}}{\mathrm{m}^3}\right]$ impact the temporal variations of the temperature distribution. The magnitude of the spatial change in the thermal profile (the relevant parameter regarding the thermally induced OPDs) scales with the thermal conductivity K_{th} $\left[\frac{\mathrm{W}}{\mathrm{m{\cdot}K}}\right]$. Introducing a doping concentration d into the host material alters the thermal conductivity from the undoped value $K_{\mathrm{th,0}}$ via[49]:

$$K_{th} = B \cdot \sqrt{\frac{K_{th,0}}{d}} \cdot \tan^{-1}\left(\frac{\sqrt{K_{th,0} \cdot d}}{B}\right), \tag{50}$$

with B as an empirically determined fit parameter. Together, the thermal conductivity, specific heat capacity, and density define the thermal diffusivity D of the material. For a known pump area with radius w_{p}, the thermal diffusivity can be utilized to grant an estimation for the relaxation time of the pump-induced change in the thermal profile via the thermal diffusion time τ_{D}[51]:

$$\tau_{\mathrm{D}} = \frac{w_{\mathrm{p}}^2}{4{\cdot}D} = \frac{w_{\mathrm{p}}^2{\cdot}\, C_p{\cdot}\rho}{4{\cdot}K_{\mathrm{th}}}. \tag{51}$$

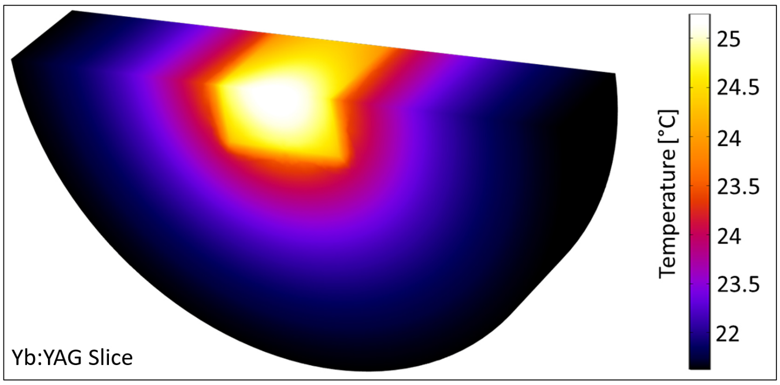

Figure 10: COMSOL simulation of the temperature distribution within a pumped Yb:YAG crystal (cross-sectional view) at the end of the pump pulse.

The change in the thermal profile of the active material is driven by the absorbed power density of the pump laser with intensity $I(x, y, t)$, doping-dependent absorption coefficient α, percentage of pump energy lost to heat η_h due to the quantum defect and other nonradiative transitions, and the pump depletion profile $A(z, t)$. Here, the pump depletion must also include the inversion level (via an iterative solution of Eqs. $20 - 21$) within the material. This is particularly relevant for high pump fluences, in which not only a large inversion, but a strong thermal gradient is generated as well.

The results of the numerical 3D model, an example of which is given in Fig. 10 using the finite element analysis software COMSOL (Version 5.2, Sweden), grant an insight into the evolution of the complete spatio-temporal thermal profile of the pumped active material. A verified model using calibrated temperature measurements can then be applied to characterize the thermal profile of an active material within a high energy laser amplifier to determine the strength and – with the assistance of beam propagation simulations – the impact of the thermally induced wavefront aberrations on the spatial profile of the amplified laser pulse.

Electronic Contributions

In addition to generating a thermal gradient, pumping an active material also produces an inversion in the population of laser-active ions in the lower and upper lasing levels, which is necessary for laser amplification. In such a scenario, the dynamic response to the incident EM-field changes, in the form of a polarizability difference $\Delta\alpha$ between the lasing levels, due to the modification[52,53] of the charge distribution of the laser-active ions. As the polarizability α – with induced dipole density N_p – is directly connected to the refractive index n_0 of the material via[54]:

$$\frac{n_0^2 - 1}{n_0^2 + 2} = \frac{4\pi}{3} N_\mathrm{p} \alpha, \tag{52}$$

a difference in the polarizability consequently alters the refractive index profile within the pumped region of the active material. Therefore, the population inversion $\beta(\vec{r}, t) = \frac{N_2(\vec{r}, t)}{N_\mathrm{dop}}$, a large amount of which is required for laser pulse amplification at the joule-class and above, also results in a spatio-temporally inhomogeneous OPD profile $\phi_{\mathrm{e}}(\vec{r},t)$[55,56]:

$$\phi_{\mathrm{e}}(\vec{r},t) = \frac{2\pi}{n_0}\left(\frac{n_0^2+2}{3}\right)^2 \Delta\alpha\Delta N_2(\vec{r},t)L \tag{53}$$

that increases in magnitude as the gain factor G_0 (Eq. 23, from which changes in the inversion level $\Delta\beta(\vec{r},t) = \frac{\Delta N_2(\vec{r},t)}{N_{\mathsf{dop}}}$ can be extracted) or material length L increases. The amplitude of the electronic contributions to the pump-induced wavefront aberrations decreases with a timescale according to the inversion depletion in the material, i.e., the fluorescence lifetime τ_{fl}, which is typically in the millisecond regime[19] for Yb^{3+}-doped materials. As this differs from the lifetime of the thermal contributions by several orders of magnitude, the two effects can be temporally distinguished[23] from one another due to their relaxation. During the time frame of laser pulse amplification (towards or at the end of the pump pulse duration), however, the independent effects reach their peak magnitude and interact simultaneously to imprint inhomogeneous spatial phase profiles onto the wavefront of the amplified laser beam, leading to significant beam profile distortions and a reduction in the final focusability and fluence of the laser system.

2.4.3 Temporal: Spectral Bandwidth Preservation and Broadening

The shortest achievable laser pulse duration within a CPA laser system is fixed by the emission bandwidth of the laser-active materials and spatio-spectral clipping within the stretcher-compressor designs. Furthermore, a preservation of the temporal fidelity of a laser pulse at the petawatt-class is challenging, particularly due to gain narrowing[57] and spectral phase distortions that occur within the CPA chain. At the front-end of the laser system, for example, regenerative amplifiers are typically utilized to bring the pulse energies to the millijoule regime. Here, a total of 100 material passes is not uncommon in the case of the low gain, broadband Yb:FP15-glass or Yb:CaF$_2$. The combination of the non-uniform spectral gain profile of the active material along with the total gain factor on the order of 10^6 (e.g., for the first regenerative amplifier within the POLARIS[14] laser system) leads to a significant amplification of the central wavelength and a suppression of the spectral edges after the large number of material passes. Consequently, the spectral bandwidth is reduced, thereby lengthening the achievable FTL pulse duration and decreasing the peak power of the laser system. An example of gain narrowing in a Yb:FP15-based regenerative amplifier without spectral shaping components is given in Fig. 11. The gain spectrum, with the emission and absorption profiles taken from Fig. 3, is calculated using Eq. 23 for the Yb:FP15-glass pumped at half the pump saturation intensity ($I_{\mathrm{sat,p}} = 47\,\mathsf{kW/cm}^2$) with a thickness of 1.3 cm, optimized to balance pump absorption and seed reabsorption. Although the gain spectrum (black) is significantly broader than

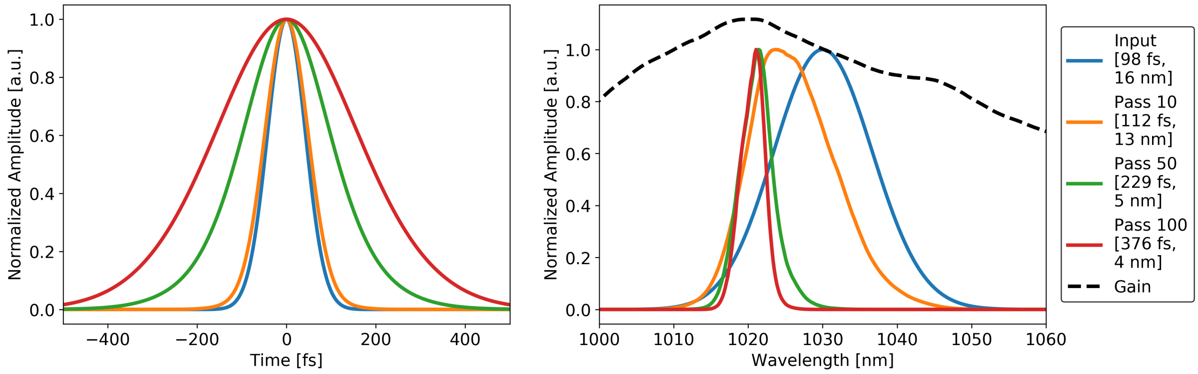

Figure 11: Compressible pulse durations (left) and amplified spectra (right) within a simulated Yb:FP15-based regenerative amplifier exhibiting a gain spectrum (black, normalized according to the gain at the input central wavelength $\lambda_{\mathrm{L}} = 1030\,\mathrm{nm}$) larger than the input laser spectrum (blue). The input bandwidth is significantly reduced after 100 passes through the active material, lengthening the shortest achievable pulse duration by a factor of 4. Values within the legends represent the FWHM pulse durations and spectral bandwidths.

the 16 nm FWHM input spectrum (blue), the bandwidth is reduced by more than a factor of 3 after 50 passes, increasing the compressible pulse duration from 98 fs to 229 fs FWHM. For the case of 100 material passes, only 4 nm of the spectrum remains, while the compressible pulse duration has been lengthened by a factor of 4, leading to a reduction in the peak power of the same factor.

Therefore, during the amplification process itself, the gain spectra of the laser-active material ultimately sets the limit for the shortest pulse durations achievable within the CPA chain. For the case of Yb^{3+}-based high peak power laser systems, which are capable of generating pulse energies in excess of 50 J[14], the compressed 100 fs pulse duration is nevertheless over 3 times longer than that of ultrashort Ti:Sapphire[58] laser systems. To overcome this limitation, a process is required that is capable of broadening the spectral bandwidth of the laser pulse after the CPA chain. At this stage within the laser system, the intense nature of the laser pulse is sufficient to induce processes such as self-phase modulation (SPM) in nonlinear materials. Here, the spectral broadening induced by SPM can directly lead to a final pulse duration following recompression that is shorter than the initial value limited by the laser-active materials. Utilizing such a method offers the possibility of closing the gap between the achievable pulse durations of Yb^{3+}-based and Ti:Sapphire laser systems and can, in general, lead to a significant increase of the laser intensity of petawatt-class lasers post-CPA without the need for additional high energy laser amplifiers.

Self-Phase Modulation

Spectral modifications of the laser pulse can be accomplished through the use of nonlinear processes, which are enabled within a material during an interaction with a laser pulse containing a sufficiently high intensity. In nonlinear optics, the following convention[17] is typically used to mathematically derive the laser and nonlinear material parameters, in which the electric field $E(z,t)$ is given by $E(z,t) = A(z,t)e^{i(k(\omega)z-\omega t)} + c.c.$ and the corresponding intensity by $I = 2n_0\epsilon_0 c_0|A|^2$. Here, the 3rd-order nonlinear term of the polarization $P(z,t)$ in Eq. 6 – the 2nd-order term is only present in anisotropic optical materials, and is described in more detail under the context of nonlinear amplification in section 2.3 – can be written (neglecting conversion processes, such as third harmonic generation) in the frequency domain:

$$P^{(3)}(z,\omega) = 3\epsilon_0\chi^{(3)}(\omega)E^3(z,\omega) = 3\epsilon_0\chi^{(3)}(\omega)|A(z,\omega)|^2A(z,\omega), \tag{54}$$

with the 3rd-order susceptibility $\chi^{(3)}$ related to the nonlinear refractive index n_2 via[17]:

$$n_2 = \frac{3}{4n_0^2\epsilon_0 c_0}\chi^{(3)}. \tag{55}$$

The propagation of an ultrashort laser pulse in a nonlinear dispersive material can be described by the following form of the nonlinear Schrödinger equation (NLSE)[59]:

$$\frac{\partial A(z,t)}{\partial z} = \left[i\sum_{m=1}^{\infty} k_m \frac{i^m}{m!}\frac{\partial^m}{\partial t^m} + \left(i - \frac{1}{\omega_0}\frac{\partial}{\partial t}\right)\frac{\omega_0}{c}n_2 I\right]A(z,t) = [\hat{D} + \hat{N}]A(z,t), \tag{56}$$

which applies the SVEA assumption $|\frac{\partial^2 A(z,t)}{\partial z^2}| \ll |k\frac{\partial A(z,t)}{\partial z}|$ of a laser field with a slowly varying envelope. The NLSE can be separated according to the dispersive and nonlinear operators on the ultrashort laser pulse[39,59]. To optimize the numerical computation, the temporal derivatives can be transformed into a multiplication by $-i\omega$ in the frequency domain via a Fourier transform:

$$\mathcal{F}\{f(t)\} = \frac{1}{\sqrt{2\pi}}\int_{-\infty}^{\infty} f(t)e^{i\omega t}\mathrm{d}t. \tag{57}$$

Here, the dispersion component $\hat{D}_t$ can be rewritten as $\hat{D}_\omega$:

$$\hat{D}_t = i\sum_{m=1}^{\infty}\frac{k_m i^m}{m!}\frac{\partial^m}{\partial t^m} \overset{\mathcal{F}}{\Rightarrow} \hat{D}_\omega = i\sum_{m=1}^{\infty}\frac{k_m}{m!}(\omega-\omega_0)^m, \tag{58}$$

where k_m is the m-th derivative with respect to the angular frequency ω of the propagation constant (given previously in Eq. 9), such that k_2 = GVD and k_3 = TOD.

The nonlinear component $\hat{N}$ in the NLSE:

$$\hat{N} = \hat{N}_{\mathrm{SPM}} + \hat{N}_{\mathrm{SS}} = \frac{2n_2\epsilon_0 n_0}{A(z,t)}\left(i\omega_0|A(z,t)|^2A(z,t) + \mathcal{F}^{-1}\left\{i\omega\mathcal{F}\left\{|A(z,t)|^2A(z,t)\right\}\right\}\right) \tag{59}$$

describes self-phase modulation (SPM, first term on the right-hand side) and self-steepening (SS, second term), both of which alter the spectral distribution during laser pulse propagation.

During self-phase modulation, the spectral phase $\phi(\omega) = k(\omega)z$ of the laser pulse is altered by the factor $\hat{N}_{\mathrm{SPM}}$ (equivalent to the factor $i\frac{\omega_0}{c}n_2 I$ in Eq. 56), resulting in an intensity-dependent change in the instantaneous angular frequency $\omega(t)$ and subsequent generation of new spectral components around the carrier frequency ω_0 according to $\delta\omega(t) = \frac{\partial\phi}{\partial t} - \omega_0 = \frac{\partial \hat{N}_{\mathrm{SPM}}}{\partial t}z$. This nonlinear modification of the spectral phase also leads to an intensity-dependent modulation of the group velocity of the pulse via the self-steepening factor $\hat{N}_{\mathrm{SS}}$. In the temporal domain, the group velocity at the peak of the pulse is lower than at the wings, thereby shifting the peak towards the trailing edge and steepening it. Subsequently, the temporal asymmetry of the pulse results in a shift of the spectral distribution – in this case, towards lower frequencies. To understand the impact of these effects in combination with dispersion, the NLSE can be solved numerically using a modified version of the 4th-order Runge-Kutta in the interaction picture (RK4IP[39]) method, which is superior to the conventional RK4 and split-step methods in both computational speed and accuracy. Here, the ultrashort pulse propagates through the total material thickness L in small steps h, through which a separation of the dispersion $\hat{D}_\omega$ and nonlinear $\hat{N}$ terms are possible:

$$
\begin{aligned}
&A = A(z,t) \\
&\left|\begin{aligned}
A_0 &= \mathcal{F}^{-1}\left\{e^{\frac{h}{2}\hat{D}_\omega}\cdot\mathcal{F}\left\{A\right\}\right\} \\
B_1 &= \mathcal{F}^{-1}\left\{e^{\frac{h}{2}\hat{D}_\omega}\cdot\mathcal{F}\left\{h\hat{N}A\right\}\right\} \\
A_1 &= A_0 + \frac{B_1}{2} \\
B_2 &= h\hat{N}A_1 \\
A_2 &= A_0 + \frac{B_2}{2} \\
B_3 &= h\hat{N}A_2 \\
A_3 &= \mathcal{F}^{-1}\left\{e^{\frac{h}{2}\hat{D}_\omega}\cdot\mathcal{F}\left\{A_0 + B_3\right\}\right\} \\
B_4 &= h\hat{N}A_3 \\
A_4 &= \mathcal{F}^{-1}\left\{e^{\frac{h}{2}\hat{D}_\omega}\cdot\mathcal{F}\left\{A_0 + 3\left(\frac{B_1}{2} + B_2 + B_3\right)\right\}\right\} + \frac{B_4}{6}
\end{aligned}\right. \\
&A(z+h,t) = A_4
\end{aligned}
$$

Using this technique, the propagation of a 1030 nm, 100 fs laser pulse with an intensity of 1 TW/cm^2 through a 4 mm thick fused silica (SiO_2) substrate was simulated, with the results displayed in Fig. 12 for various cases of nonlinear and dispersive effects. In the top left and right figures, the temporal and spectral profiles after nonlinear pulse propagation without dispersion are shown. While both SPM and SS preserve the initial pulse duration, a significant reduction in the Fourier transform limited (FTL) pulse duration is achievable due to the large broadening of the bandwidth after SPM. With the introduction of self-steepening, the pulse peak is shifted towards the trailing edge and the spectral distribution becomes red-shifted.

In the bottom figures, the dispersion of fused silica is included in the simulation. For the case of positive dispersion, the intensity of the pulse decreases as the pulse width increases via GVD, thereby reducing the bandwidth-broadening effect of the intensity-dependent SPM. With negative dispersion (here, for example, with the same magnitude as in the positive case), however, the additional frequencies produced via SPM are temporally shifted towards the peak of the pulse, compressing the pulse and increasing the intensity. As a result, a positive feedback-loop is generated that increases the spectral bandwidth and shortens the pulse duration. With a suitable nonlinear material for spectral broadening and a compact stage that implements negative GVD for pulse compression, this method could be applied to petawatt-class laser pulses post-CPA, with multiple stages offering the possibility to transform the laser pulse duration into the single-cycle regime.

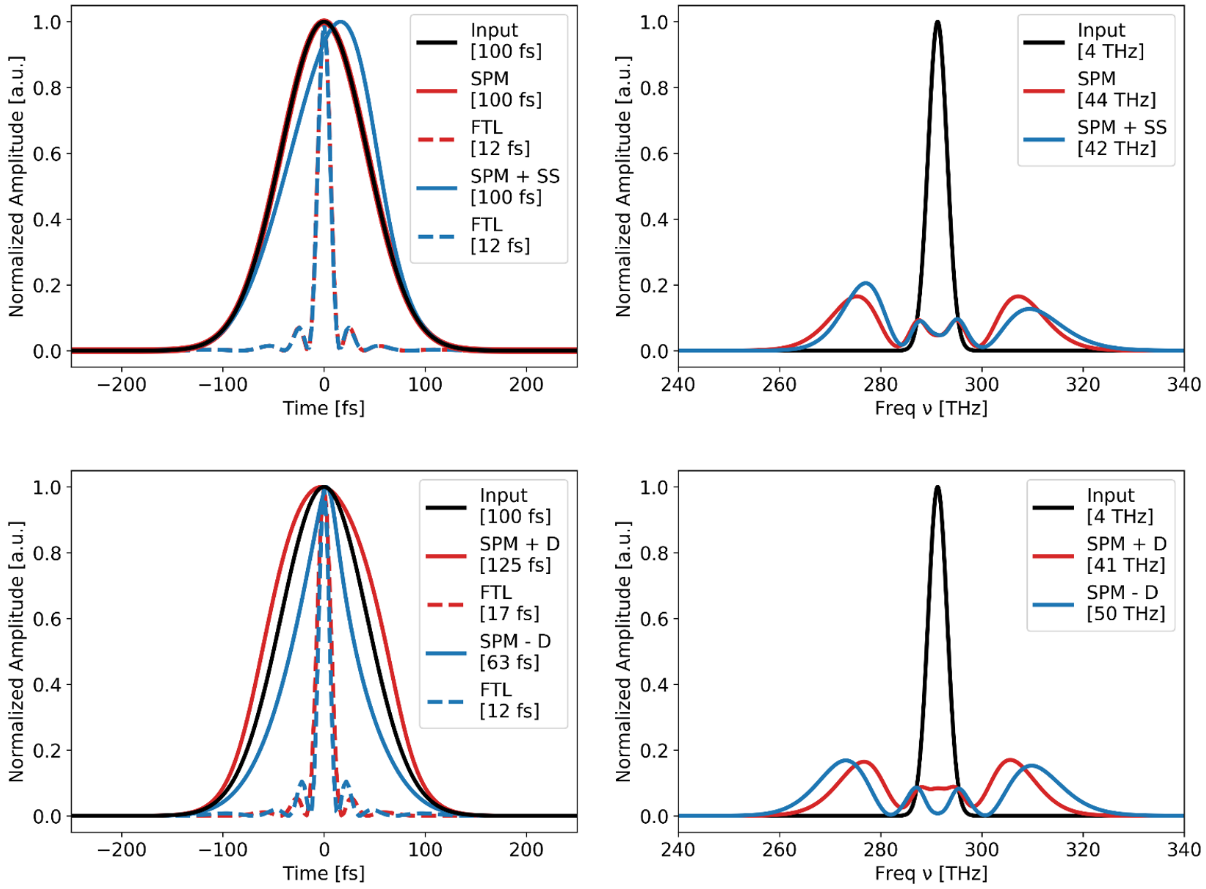

Figure 12: Temporal intensity profile (left) and spectrum (right) of a 100 fs pulse propagating through 4 mm of fused silica. The effect of purely nonlinear propagation (via self-phase modulation and self-steepening) is given in the top figures. The bottom figures depict the interplay between the dispersive (± D for positive or negative GVD) and nonlinear terms and the resulting modifications in the temporal and spectral profiles.

2.4.4 Contrast: Pre-Pulse and Pedestal Suppression

An optimization of petawatt-class laser systems towards higher laser pulse intensities must be accompanied by a further reduction in the rising edge of the laser pulse and a suppression of pre-pulses. Spontaneous emission, for example, generated and amplified[60] within the pumped active material – in a high peak power laser system focused to on-target intensities in excess of $10^{20}\ \frac{\mathrm{W}}{\mathrm{cm}^2}$ – can ionize the target surface before the main pulse and significantly deteriorate[13,61,62] the experimental performance of the desired laser-plasma interaction. Here, a temporal intensity contrast ($TIC = I_0/I(t)$) between the peak intensity I_0 and the amplified spontaneous emission (ASE) pedestal of at least 10^9 is required to prevent the deformation of metal foil targets with ionization thresholds near $10^{11}\ \frac{\mathrm{W}}{\mathrm{cm}^2}$. The relative peak ASE intensity, represented by the parameter TIC^{-1}, generated within a regenerative amplifier in the front-end of the high peak power laser system can be estimated via[63]:

$$TIC_{\mathrm{ASE}}^{-1} = \frac{I_{\mathrm{ASE}}}{I_0} \approx I_{\mathrm{sat}} K_{\Delta\Omega} K_p K_{\Delta\nu} \frac{\tau}{E_0}, \tag{60}$$

with the intensity of the amplified spontaneous emission I_{ASE}, pump saturation intensity I_{sat}, main laser pulse energy entering the amplifier E_0 and final pulse duration τ. The parameters $K_{\Delta\Omega}$, K_p, and $K_{\Delta\nu}$ describe the spatio-angular, spectral, and polarization acceptance of the amplifier, respectively. A comparison[63] of the TIC^{-1} performance of a variety of high power laser systems is given in Fig. 13.

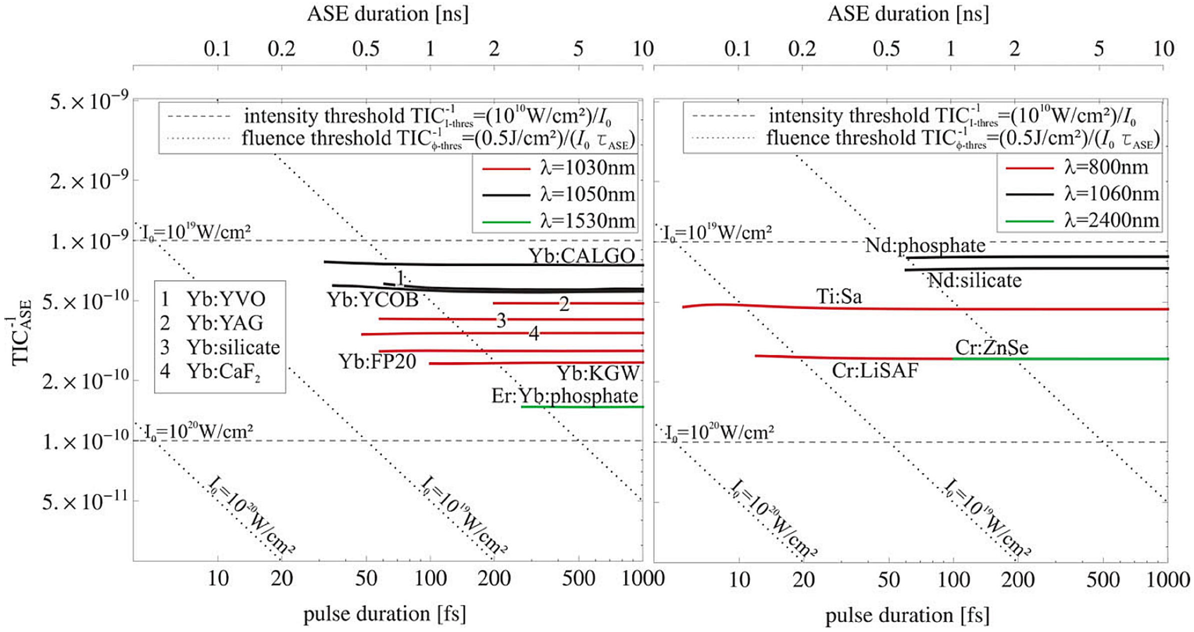

Figure 13: Estimated TIC_{ASE}^{-1} values[63] for laser systems based on low gain Yb-doped (left) and various high gain (right) active materials for focused peak laser intensities between $10^{19} - 10^{20}\ \frac{\mathrm{W}}{\mathrm{cm}^2}$.

In addition to the ASE pedestal, the temporal intensity contrast of a laser system can be degraded by post-pulses generated from back-reflections on plane-parallel surfaces, leading to pre-pulse replicas[64] during pulse compression due to a nonlinear phase accumulation. Furthermore, the pedestal and rising edge of the main pulse itself can be deteriorated[65,66] by high frequency spectral phase modulations and scattering within the stretcher-compressor system. Due to the various sources – and therefore, various temporal separations with respect to the main pulse – of TIC degradation, a robust method is required that is capable of steepening the rising edge and suppressing all pre-pulses by several orders of magnitude with a limited impact on the main laser pulse. Here, a "plasma mirror" (details in section 3.3) after the CPA chain can be utilized to significantly improve the TIC and, consequently, provide the proper conditions for a future increase of the peak intensity and a corresponding enhancement of the experimental performance of the petawatt-class laser system.

2.5 POLARIS: A High Energy, Ultrashort Yb^{3+}-Based Laser System

A powerful tool for investigating laser-plasma interactions at laser intensities exceeding $10^{20}\ \frac{\mathrm{W}}{\mathrm{cm}^2}$ is the fully diode-pumped petawatt-class POLARIS laser system at the Friedrich Schiller University and Helmholtz Institute in Jena, Germany. The Yb^{3+}-based laser system delivers[14] an amplified laser pulse energy of 54 J, a final compressed pulse duration of 98 fs, and a temporal intensity contrast (described in section 2.4.4) for the ASE pedestal greater than 10^{12}. At POLARIS, the high intensity laser pulses are utilized to conduct experiments on laser-based particle acceleration and develop a more detailed understanding of the underlying physics behind such complex acceleration mechanisms.

A schematic of the POLARIS laser system is given in Fig. 14. The laser system begins with a Ti:Sapphire Kerr-lens mode-locked (MIRA 900, Coherent) oscillator – containing a birefringent filter to select the desired wavelength range ($\lambda_{\mathrm{L}} = 1030\,\mathrm{nm}$ with $\Delta\lambda = 20\,\mathrm{nm}$ FWHM) from the Ti:Sapphire emission spectrum – producing a 75 MHz pulse train of 5 nJ, 85 fs pulses. A single pulse is selected from the pulse train utilizing a Pockels cell (synchronized with the master trigger system) and stretched to 20 ps in an Offner-type stretcher[67], amplified to 2 mJ with a total gain on the order of 10^6 in a broadband Yb:FP15-glass[28,29] regenerative amplifier, and compressed to 130 fs in a chirped pulse amplification (CPA[15]) configuration. Here, via CPA, a significant stretching of the pulse before amplification decreases the pulse intensity below the damage threshold of the optics within the laser chain, thereby avoiding permanent material damage and enabling safe laser amplification of multiple orders of magnitude. However, the large total gain of the first regenerative amplifier consequently generates a high noise output in the form of ASE and a train of post-pulses. Furthermore, post-pulses produced within the laser chain that exist temporally inside the stretched duration of the main pulse can directly result in pre-pulse replicas[64] during compression. Improving the signal to noise ratio of the laser system requires an intensity-dependent (nonlinear) temporal pulse cleaning mechanism, such as optical parametric amplification (OPA[68]) or cross-polarized wave

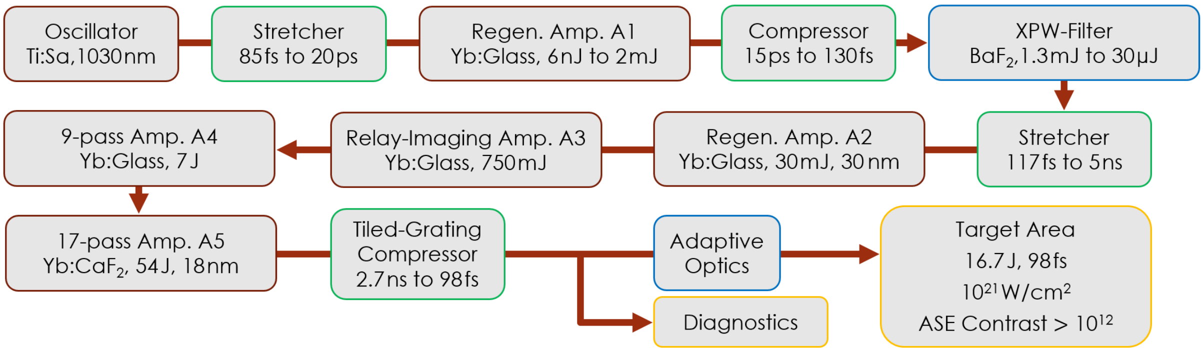

Figure 14: Schematic of the petawatt-class POLARIS laser system, consisting of a double-CPA chain encompassing 5 amplifier stages with temporal pulse cleaning via XPW and wavefront correction using adaptive optics.

generation (XPW[69]). In the case of XPW, an orthogonally polarized version of the laser pulse is generated in a nonlinear material with a typical conversion efficiency of 10% for the high intensity "main" pulse. The pre-pulses, post-pulses, and ASE pedestal surrounding the main pulse, however, experience significantly lower conversion efficiencies due to their lower intensities. The XPW-generated output pulse with an improved temporal intensity contrast profile is then separated from the initial pulse using a polarizer with a high extinction ratio.

The temporally cleaned main pulse then enters the second stage of the double-CPA chain[60], where it is first stretched to 5 ns and amplified in a second regenerative amplifier to 30 mJ[70] with a spectral bandwidth of 30 nm (pre-broadened within the XPW-filter). Here, the intensity of the stretched pulse once again approaches the laser-induced damage threshold (LIDT) of the optics within the laser chain, and must be further decreased via a magnification of the beam size after each amplifier stage. The following amplifier utilizes a multi-pass relay-imaging setup, in which the beam is imaged to the active material through each pass in a rotationally symmetric configuration[71]. Due to the imaging, the spatial quality of the beam is preserved during the 20-pass amplification to nearly 1 J. The ns-pulse is further amplified in a 9-pass "A4" (Yb:FP15 pumped by 40 laser diode stacks) and the final 17-pass "A5" (Yb:CaF$_2$ pumped by 120 laser diode stacks, with schematic[14] given in Fig. 15) amplifier to achieve a maximum energy of 54 J. The laser pulse is then compressed to 98 fs in a tiled-grating compressor[72–74] and the wavefront of the beam is corrected using adaptive optics before being focused onto the target with an intensity exceeding $10^{20}\ \frac{\mathrm{W}}{\mathrm{cm}^2}$.

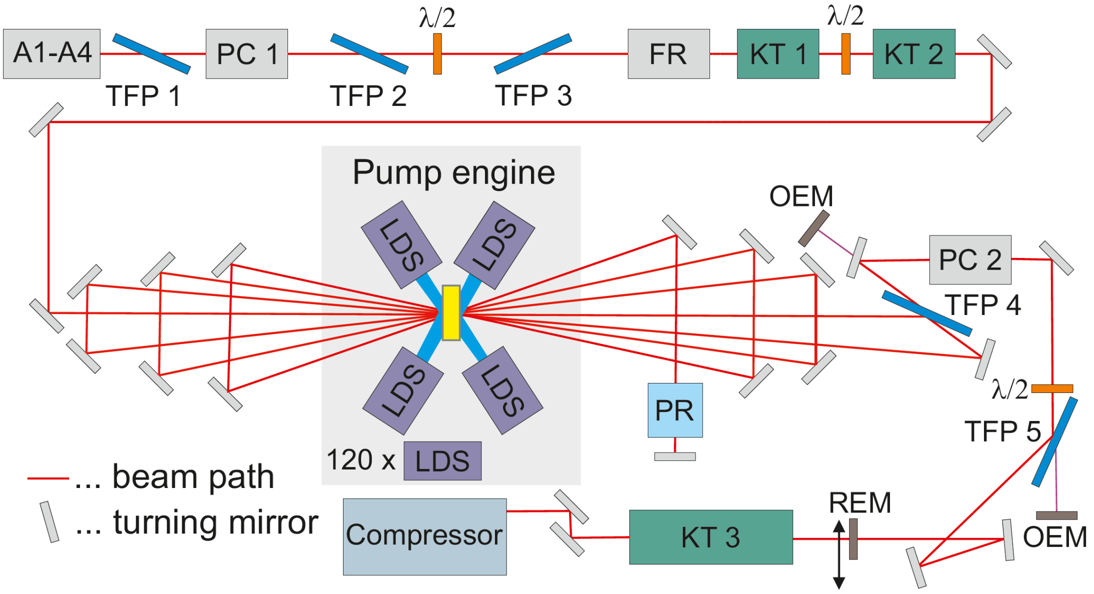

Figure 15: Schematic[14] of the final 17-pass A5 amplifier: TFP - thin film polarizer (TFP 2 and TFP 3 rotated 90° with respect to each other); PC - Pockels cell; $\lambda/2$ - half-wave plate (set for 90° rotation before TFP 3 and TFP 5 and 45° rotation before KT 2); FR - Faraday rotator; KT - Keplerian telescope; LDS - laser diode stack; PR - quarter-wave rotator (reflective); OEM - online energy meter; REM: removable energy meter.

3 Petawatt-Class Laser Optimization

Progress[75,76] and breakthroughs[77,78] in relativistic laser-plasma physics are dependent on the continuous evolution of state-of-the-art laser systems. As these systems are optimized towards higher on-target intensities, the laser pulse's spatial and temporal distribution and temporal intensity contrast profile become increasingly crucial factors[79,80] regarding the experimental performance of the laser system. In this section, multiple investigations are described that address the improvement of these laser parameters for the current and upcoming generation of petawatt-class laser systems.

3.1 Spatial: Pump-Induced Wavefront Aberrations

Due to the limiting laser-induced damage threshold (LIDT) of laser-active materials, large seed beam diameters are typically required in high energy amplifiers[14]. Consequently, to preserve the quality of the large amplified beam, ensuring a spatially homogeneous pump profile becomes increasingly important. Even with a flat-top-like gain profile, however, the spatial profile of a laser pulse passing through a strongly pumped broadband active material such as Yb:CaF$_2$ or Yb:FP15 in a joule-class multi-pass laser amplifier can be heavily degraded by spatio-temporally inhomogeneous optical path differences (OPDs), which are imprinted[23] onto the wavefront of the amplified seed pulse by the pumped active material. During propagation, high frequency spatial phase aberrations can deform the spatial profile – as seen in Fig. 16, for the case of a 9-pass joule-class Yb:FP15-based amplifier at POLARIS seeded by a Gaussian-like beam profile – enough to result in damage to optical components within the laser chain when the local beam fluence exceeds the LIDT. Hence, the spatial beam quality is often the limiting parameter for the final fluence and focusability of the laser pulse. To optimize the performance of state-of-the-art high peak power lasers, a comprehensive understanding of the spatio-temporal profiles of pump-induced OPDs is critical.

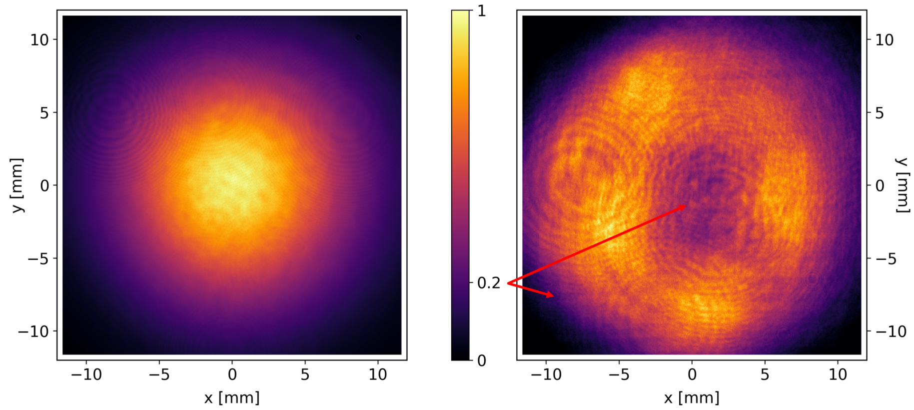

Figure 16: Comparison of beam profiles at the input (left) and output (right) of a Yb:FP15-based joule-class multi-pass laser amplifier in the POLARIS laser system.

3.1.1 Phase Profile Measurements

Pumping an active material alters the temperature profile within the material and introduces a region of excited laser-active ions, resulting in both thermally[22] and electronically[55] induced changes in the refractive index. This pump-induced inhomogeneous refractive index profile is transferred, as depicted in Fig. 17, in the form of locally varying optical path differences (OPDs) to the wavefront of the amplified seed pulse, thereby distorting it upon propagation. For the case of Yb^{3+}-doped materials, the minimal quantum defect of 9%[19] leads to a relatively low amplitude – when compared to Ti^{3+}-doped (33%[24]) or Nd^{3+}-doped (24%[81]) active materials – for the thermal contributions to the OPD profile and a corresponding increase in the significance of the electronic contributions. The wavefront aberrations resulting from the thermally induced OPDs are typically assumed to be parabolic in form, according to the shape of the temperature profile[82] under uniform pumping conditions, effectively resulting in a focusing or defocusing of the full beam profile. The impact of the electronic OPD contributions on the incident wavefront, however, have only been characterized temporally[55,56] for a limited number of Yb^{3+}-doped materials utilizing small (50 µm radius), Gaussian-like beams. For the large beam diameters within petawatt-class laser systems, the assumption of a purely parabolic change in the wavefront no longer holds, as high spatial frequency components induced by the total OPD profile significantly distort the beam profile throughout the long propagation distances typically required for high energy multi-pass amplifiers[14]. Here, a comprehensive spatio-temporal investigation on the thermally and electronically induced OPD profiles is required to model – and, where possible, mitigate – the wavefront degradation of the amplified laser pulse.

To characterize the complete pump-induced OPD profiles, time-resolved interferometric measurements have been conducted for multiple pumped Yb^{3+}-doped materials employed in diode-pumped high power laser systems: Yb:YAG[26] (high gain, narrowband crystal),

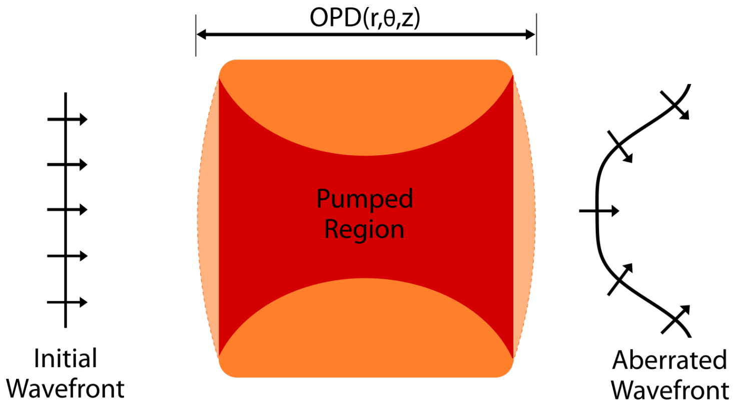

Figure 17: Depiction of laser pulse wavefront distortion after propagation through the pumped region (red) of an active material (orange).

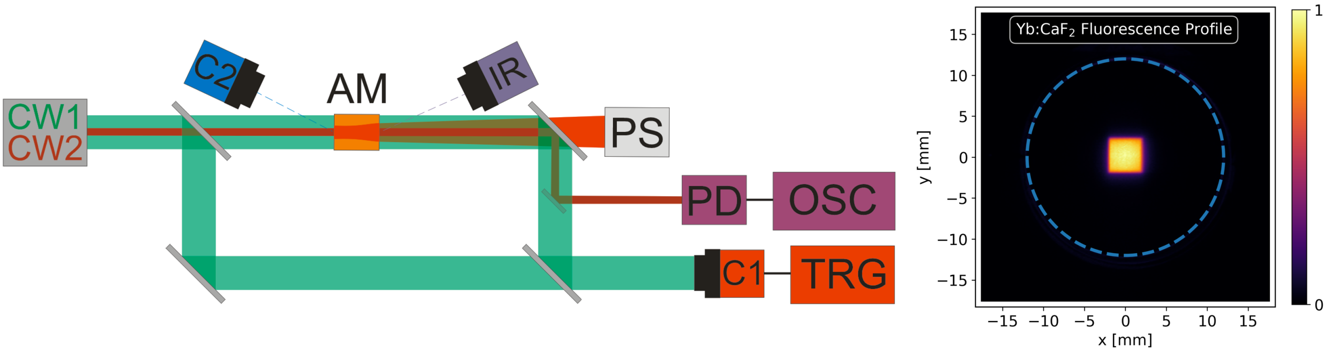

Figure 18: Experimental setup schematic (left): AM - active material; CW1/CW2 - continuous wave laser; IR - thermal (infrared) camera; C1/C2 - CCD + objective; TRG - trigger/delay; PD - photodiode; OSC - oscilloscope; PS - pump source; fluorescence profile of a pumped Yb:CaF$_2$ (right, perimeter outlined in blue).

Yb:CaF$_2$[26,27] (low gain, broadband crystal), and Yb:FP15[28,29] (low gain, broadband glass). As these materials exhibit significant differences (detailed in the following sections) in their thermal and optical properties, they are well-suited for an investigation into the various possible forms of the pump-induced OPD profiles.

The experimental setup utilized to measure the full OPD profiles across the free aperture of the pumped active materials is depicted in Fig. 18. The water-cooled Yb^{3+}-doped active materials were end-pumped by a 6.8 kW, 940 nm laser diode source (PS) containing a microlens array setup to homogenize the spatial profile. The pump pulse durations τ_{p} and repetition rates were chosen according to the fluorescence lifetimes[19,29] and thermal diffusivities[29,49,50] of the materials (Yb:YAG: 0.9 ms / 2 Hz, Yb:CaF$_2$: 2 ms / 4 Hz, and Yb:FP15: 1.4 ms / 0.2 Hz). A 532 nm continuous wave laser (CW1) was aligned in a Mach-Zehnder configuration with the pumped active material located in one arm of the interferometer. Using a camera setup (C1: Allied Vision Manta G-032B CCD with an exposure time of 26 µs, equipped with an F/1.8 objective and 2x focal length extender) with a variable delay with respect to the pump pulse, the OPD profiles imprinted onto the phase of the CW1 laser directly after passing through the pumped active material could be extracted from the interferometric measurements throughout the pump cycle (spanning both the pumping and cooling period). The measurements were taken after the materials entered a thermalized state ($\approx$100 pump pulses), in which the average temperature no longer increased with each successive pump pulse. The phase changes induced by the pumped active material were extracted from fringes via the Fourier transform method[83].

In Fig. 19, the full pump-induced OPD profiles for each material are displayed, with the 2D profiles (left) at $t = \tau_{\text{p}}$ and multiple center lineouts (right) throughout the pump cycle. For Yb:YAG and Yb:FP15, the square-shaped pump profile is directly imprinted onto the phase of the seed laser during the pump pulse, where the amplitude of the OPD profile increases in a positive manner. During the cooling phase, the OPD profile returns to the thermalized state. For Yb:CaF$_2$, however, the phase imprint of the pump profile is washed out and the temporal variation in the OPD profile follows a more complicated progression. For a comprehensive understanding of the spatio-temporally inhomogeneous pump-induced OPD profiles, the thermal and electronic contributions must first be independently characterized.

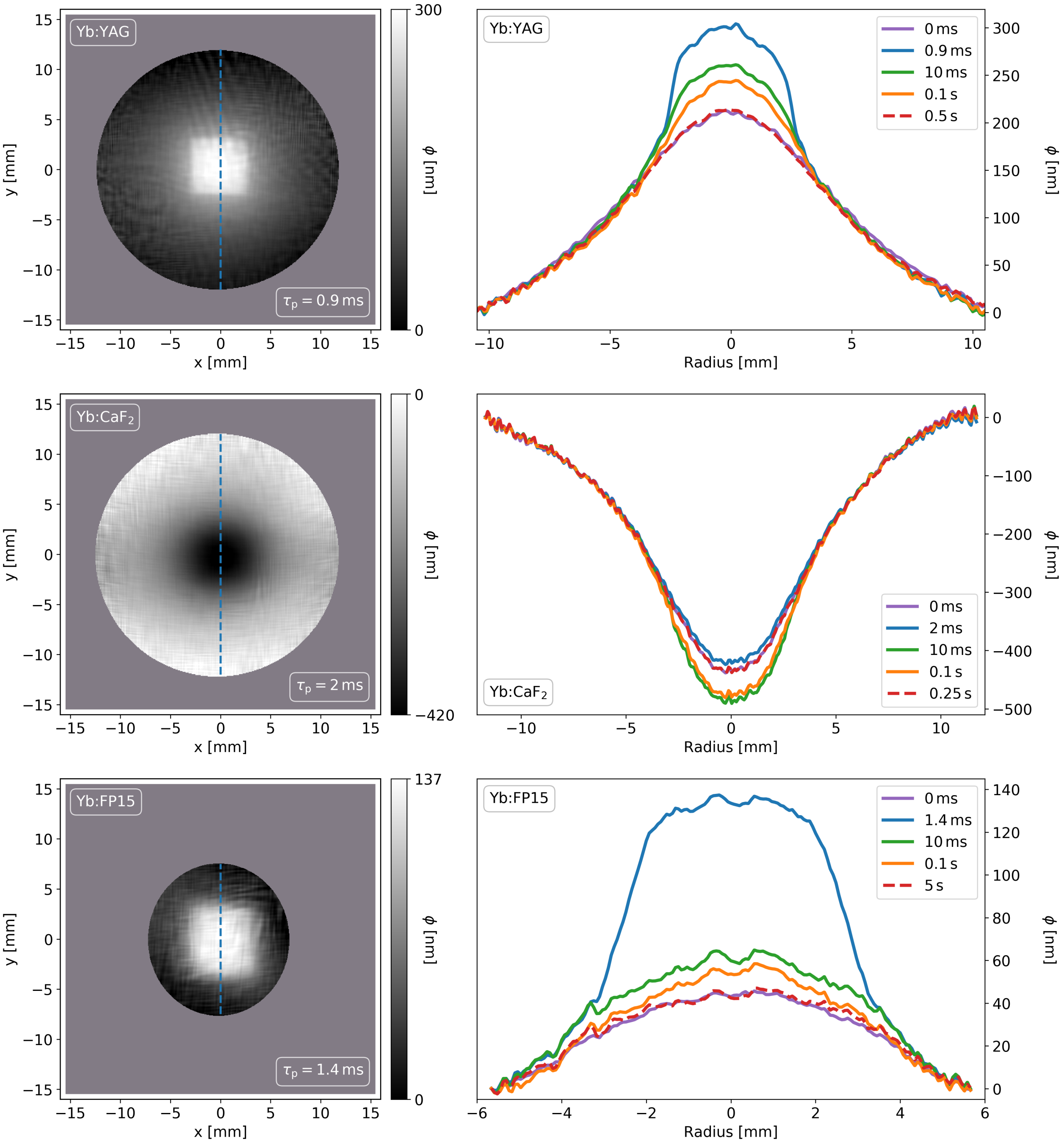

Figure 19: Pump-induced OPD profiles (left) for Yb:YAG (top), Yb:CaF$_2$ (center), and Yb:FP15 (bottom) at the end of the pump pulse (denoted by the timestamps), along with lineouts (right) taken along the vertical dashed blue line of the OPD profiles at various times during the pumping and cooling periods.

3.1.2 Thermal Phase Contributions

The temperature gradient induced within an active material by pumping alters the refractive index and causes thermal expansion and stress, which introduce an inhomogeneous[22] OPD profile $\phi_{\mathrm{th}}(\vec{r},t)$ within the material. As described in section 2.4.2, this thermal contribution to the pump-induced wavefront aberrations can be modeled with the knowledge of the total thermo-optic coefficient χ and the mean temperature shift $\langle T(\vec{r},t) - T_0 \rangle$ along the active material length L. To determine the relative impact of the thermal contributions, the spatio-temporal thermal phase model can be compared to the measurements of the full pump-induced OPD profiles.

Spatio-Temporal Thermal Profile Modeling

The 3D spatio-temporal thermal profile of each characterized Yb^{3+}-doped material was simulated numerically using the finite element analysis software COMSOL[84] (Version 5.2, Sweden). Here, the heat transfer equation (Eq. 49) was employed to solve for the 3D spatial and temporal thermal distribution within the active materials under the same pumping and cooling conditions present in the experimental setup (Fig 18).

The values of the material properties necessary for the numerical simulation – thermal conductivity K_{th}, specific heat capacity C_p, density ρ, thermal expansion coefficient α_T, absorption coefficient α, and the percentage η_{h} of pump energy converted to heat via the quantum defect and other non-radiative transitions – are given in Table 2. These parameters have been corrected according to their doping-dependence where appropriate (e.g., Eq. 50 for K_{th}). To ensure an accurate modeling of the absorbed energy density throughout the material, the inversion-corrected pump depletion along the material thickness was determined numerically via iterative solutions of Eqs. 20 – 21. Further details regarding the thermal modeling process can be found in section 2.4.2. After the completion of the steady-state thermalization process within the numerical model, the thermal profiles of the simulated materials were extracted and tested for accuracy by comparing the results to measurements of the temperature distribution along the accessible (front and back) surfaces of the pumped active materials.

Table 2: Relevant optical and thermal properties of the considered active materials.

Material	Yb^{3+}-Doping $[\frac{\mathrm{ions}}{\mathrm{cm}^3}]$	$K_{\mathrm{th}}\,[\frac{\mathrm{W}}{\mathrm{m \cdot K}}]$	$C_p\,[\frac{\mathrm{J}}{\mathrm{kg \cdot K}}]$	$\rho\,[\frac{\mathrm{kg}}{\mathrm{m}^3}]$	$\alpha_T\,[\cdot 10^{-6}\mathrm{K}^{-1}]$	$\alpha\ [\mathrm{m}^{-1}]$	η_{h}
Yb:YAG[26,50]	$4.2 \cdot 10^{20}$	9.2	615	4660	7	296	0.07
Yb:CaF$_2$[26,49,50,85]	$3.8 \cdot 10^{20}$	6.3	816	3180	18.5	67	0.06
Yb:FP15[29,86]	$6 \cdot 10^{20}$	0.88	720	3800	14	187	0.13

A thermal infrared imaging camera FLIR P620[87] (IR in Fig 18, with 640 × 480 pixels and a thermal sensitivity of 0.04 K) was utilized to record the front and back thermal profiles of the pumped Yb^{3+}-doped materials throughout the pumping and cooling times. The temperature measurements were calibrated using the experimentally determined emissivity ϵ of the materials. Here, black electrical tape (a simple, cost-efficient method[88]) was fixed onto the water-cooled mount with a pre-determined $T_0 = 20.5$°C and the emissivity setting of the thermal infrared camera was corrected to recover the known mount temperature. Furthermore, the temperature of the active materials was increased from 20°C to 50°C and measured using a separate temperature sensor along with the thermal camera. The high emissivity value $\epsilon = 0.94$ of the active materials, determined independently by both calibration methods, limits the ability of the thermal camera to detect the temperature distribution inside the materials. Nevertheless, the front and back surface temperature measurements at the minimum integration time of 30 ms allow for a spatio-temporal characterization of the thermal profile of the pumped active materials and a verification of the numerical model. For all three considered materials, the simulated and measured results show an excellent agreement, with a maximum relative discrepancy of less than ±3 %. In Fig 20, a thermal image, a section view of the 3D model, and the results of the thermal profile characterization for the case of the pumped Yb:FP15 are presented.

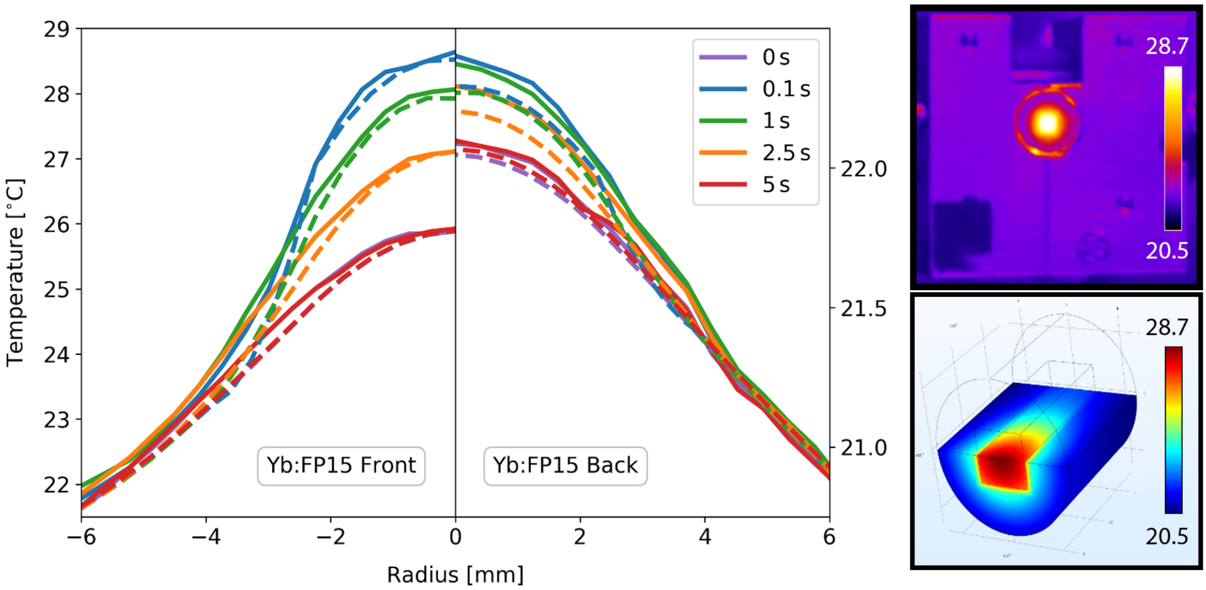

Figure 20: Comparison (left) of measured (solid) and simulated (dashed) Yb:FP15 front and back thermal profiles, displayed for times 0, 0.1, 1, 2.5, and 5 seconds within the pump cycle (rep. rate 0.2 Hz; pump cycle = 5 s). A thermal image (top right) of the pumped Yb:FP15 along with a slice through the pumped Yb:FP15 model (bottom right) in COMSOL are shown.

The Total Thermo-Optic Coefficient

To determine the amplitude of the thermal contributions to the pump-induced wavefront aberrations, the results from the verified thermal model as well as the magnitude of the total thermo-optic coefficient χ – comprised of the thermo-optic coefficient $\mathrm{d}n/\mathrm{d}T$, photoelastic stress constant $C_r^{\prime}$, and thermal expansion α_T – for the considered materials are required. While the $\mathrm{d}n/\mathrm{d}T$ and thermal expansion terms are readily available in literature, the photoelastic constant is – following the discussion in section 2.4.2 – unknown for the Yb^{3+}-doped versions of the materials. Due to the verification of the thermal model, however, the $C_r^{\prime}$ values 3.2·10^{-3} for Yb:YAG, -3.7·10^{-2} for Yb:CaF$_2$, and 1.9·10^{-3} for Yb:FP15 could be directly extracted by comparing the simulated thermally induced OPD profiles (Eq. 46, with $C_r^{\prime}$ as the variable to be solved) to the measured OPD profiles of each pumped and thermalized material directly before the arrival of the pump pulse. Table 3 displays the total thermo-optic coefficients for the three characterized materials. The comparison between the simulated and measured thermal contributions to the OPD profiles are shown in Fig. 21.

The experimental determined χ value for Yb:YAG agrees well with published results[22], while the photoelastic constant for Yb:FP15 was found to be similar to that of other Yb-doped phosphate and silicate glasses ($C_r^{\prime} = 1{\cdot}10^{-3}$[51]). For Yb:CaF$_2$, however, the literature (undoped) value[49] of the stress component is 2.75 times larger than the experimental result. Here, the exchange of 2 Yb-ions and 3 Ca-ions during the doping process strongly affects[48] the face-centered-cubic lattice, and thus, as evident with the doping-dependence of the thermal conductivity[49], the thermal and stress management properties of CaF$_2$ are altered. To ensure the validity of the experimentally determined value, the thermal-stress-induced birefringence of the pumped and thermalized Yb:CaF$_2$ sample (with an experimentally confirmed $\langle 111 \rangle$ crystal orientation using the Laue X-Ray diffraction method[89]), placed between two crossed polarizers, was measured by capturing the spatial profile of the CW1 laser passing through the setup immediately before (50 µs resolution) the pump pulse. As seen in Fig. 22, the transmitted amplitude and profile agree with the expected[22,90] results using the $C_r^{\prime}$ value established from the comparison of the thermal profile simulations and interferometric measurements.

Table 3: Total thermo-optic coefficient $\chi\,[\cdot 10^{-6}$ K$^{-1}]$

	Yb:YAG[22]	Yb:CaF$_2$[49]	Yb:FP15[29,51]
$\mathrm{d}n/\mathrm{d}T$	9.0	-10.1	-8.3
stress	0.3* $\pm$ 1.5 %	-4.0* $\pm$ 1.8 %	0.2* $\pm$ 5.6 %
stress (lit.)	0.3	-11.0	–
expansion	7.1	10.0	9.6
χ	16.4	-4.1	1.5

*Experimentally determined during this investigation.

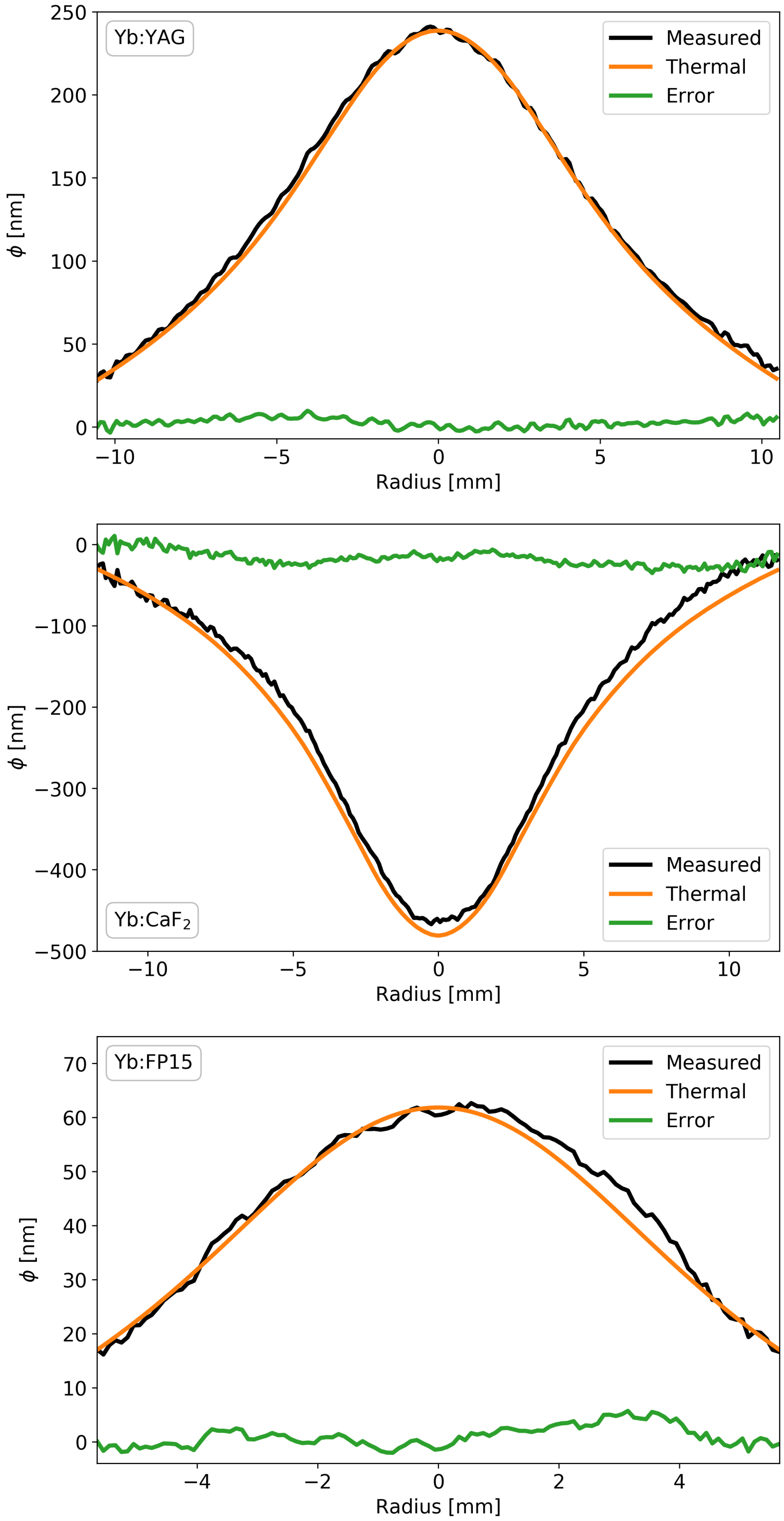

Figure 21: Comparison of the measured (black) and thermal (orange) OPD profiles at the thermalized state directly before the pump pulse arrival for Yb:YAG (top), Yb:CaF$_2$ (center), and Yb:FP15 (bottom). The discrepancy between the measured and thermal profiles is shown in green.

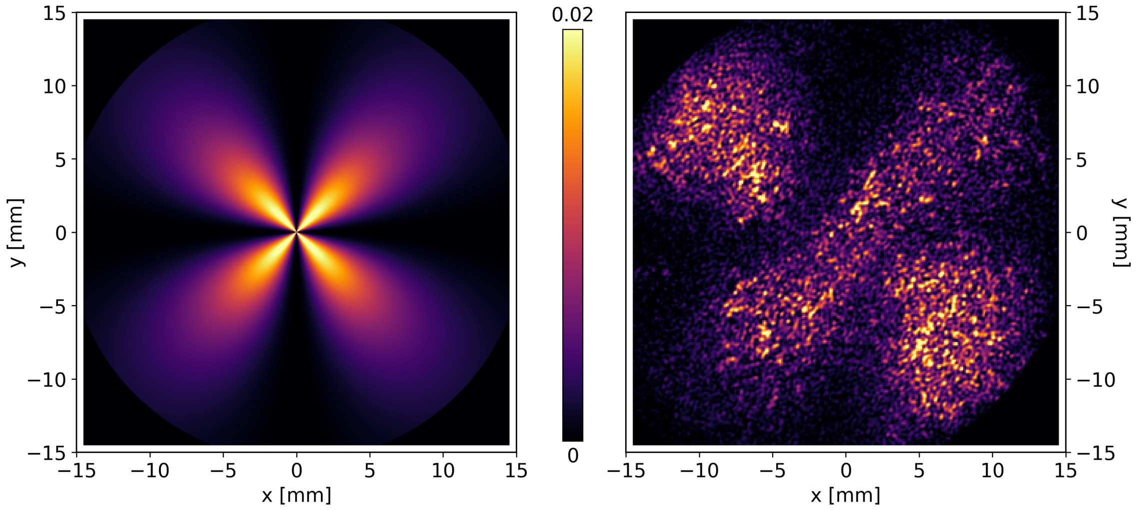

Figure 22: Comparison of simulated (left) and measured (right) Yb:CaF$_2$ birefringence spatial profiles and relative amplitudes. The color scale represents the ratio of laser light passing through the crossed polarizers due to the thermal-stress-induced birefringence.

3.1.3 Electronic Phase Contributions

The electronic contributions to the pump-induced wavefront aberrations cannot be neglected when compared to the thermal contributions, particularly for the case of Yb-doped active materials, due to the low quantum defect. During the pumping process, a region of excited laser-active ions is generated within the active material, which consequently alters the response of the material to external fields in the form of a polarizability difference $\Delta\alpha$ between the excited states. This results in a local modification in the refractive index – and therefore, an inhomogeneous OPD profile $\phi_\mathrm{e}(\vec{r},t)$ (Eq. 53) – that depends linearly on the population inversion $\Delta\beta(\vec{r},t)$ in the pumped active material. Similarly to the strong doping dependence of the thermal and stress management properties of the materials, the polarizability difference of the Yb^{3+}-ions, as seen in Table 4, can vary over an order of magnitude between host materials. The polarizability difference values for many common active materials, including Yb:CaF$_2$ and Yb:FP15 prior to this investigation, were not yet available in literature.

As evident in Eq. 53, the electronic phase contributions induced by the pump pulse relax as the population inversion in the pumped active material decreases, i.e., according to the fluorescence lifetime τ_fl. The spatio-temporal profile of the population inversion generated within each considered Yb^{3+}-doped material could be extracted from measurements of the

Table 4: Previously reported magnitudes of the polarizability difference $\Delta\alpha$ for various Yb^{3+}-doped active materials

	Yb:YAG[55]	Yb:KGW[91]	Yb:YVO$_4$[91]	Yb:Lu$_2$O$_3$[52]	Yb:Sc$_2$O$_3$[52]
$\Delta\alpha\,[\cdot 10^{-26}\ \mathrm{cm}^3]$	1.95 ± 12.8%	10.3 ± 4.9%	8.1 ± 4.9%	2.6 ± 23.1%	1.9 ± 26.3%

small signal gain (Eq. 23) and the fluorescence profile. Here, the fluorescence profile integrated along the material thickness (displayed in Fig. 18 for Yb:CaF$_2$) was captured with a CCD (C2) with an exposure time of 26 μs that was synchronized with the pump pulse. The temporally resolved small signal gain was measured by directing a 2.2 mm ($1/e^2$ diameter) continuous wave (CW2) laser operating at 1030 nm through the center of the pumped area and onto a Thorlabs DET36A/M photodiode (PD) coupled to an oscilloscope (OSC). With the measurements for the spatial and temporal forms of the population inversion, only the amplitude of the polarizability difference remains to determine (from Eq. 53) the strength of the electronic contributions to the total OPD profiles.

Since the thermal phase contributions relax along a different timescale (i.e., according to the thermal diffusion time) than that of the electronic contributions, the two effects can be separated temporally within the interferometric measurements of the full pump-induced OPD profiles. In Fig. 23, the temporal profiles of the pump-induced OPDs at the beam center (averaged between $\pm$ 1 mm) introduced by a single pump pulse are shown. The black markers within the plot correspond to the total pump-induced OPD profiles from the interferometric measurements, averaged over 10 data sets, with the standard deviation in grey. To isolate the individual thermal (amplitude A_{th}, lifetime τ_{th}) and electronic (amplitude A_{e}, lifetime τ_{e}) contributions, a relaxation function for the total pump-induced OPD profiles (starting from $t = \tau_{\mathrm{p}}$, designated by the red lines in Fig. 23) in the form of two superimposed exponential decay functions was fitted to the experimental results.

In Table 5, the parameters of the OPD relaxation function $\phi_{\mathrm{relax}}(t)$ are given. For each considered material, the lifetime of the thermal contributions τ_{th} resembles the thermal diffusion time τ_D (Eq. 51), while the lifetime of the electronic contributions matches the fluorescence lifetime – albeit slightly longer due to reabsorption in Yb^{3+}-doped materials. Discrepancies between the extracted lifetimes and expected values for the thermally induced OPDs occur due to an approximation within the thermal diffusion time derivation, in which the heat transfer through the unpumped portion of the material is omitted. The error produced via this approximation becomes more evident with an increase in the volume of the unpumped region (total volume / pumped volume: Yb:YAG ≈ 20, Yb:CaF$_2$ ≈ 30, and Yb:FP15 ≈ 6).

Table 5: OPD relaxation $\phi_{\mathrm{relax}}(t) = A_{\mathrm{e}}e^{-\frac{t}{\tau_{\mathrm{e}}}} + A_{\mathrm{th}}e^{-\frac{t}{\tau_{\mathrm{th}}}}$

	Yb:YAG	Yb:CaF$_2$	Yb:FP15
A_{th} / A_{e} [nm]	46.6 / 46.0	-50.6 / 65.8	19.5 / 68.2
τ_{th} [s] / τ_{e} [ms]	0.49 / 1.0	0.25 / 2.7	4.9 / 2.3
Fit R^2-value	0.98	0.96	0.92
τ_D [s]	0.43[50]	0.46[49]	4.86[29]
τ_{fl} [ms]	0.95[19]	1.9[19]	1.4[29]

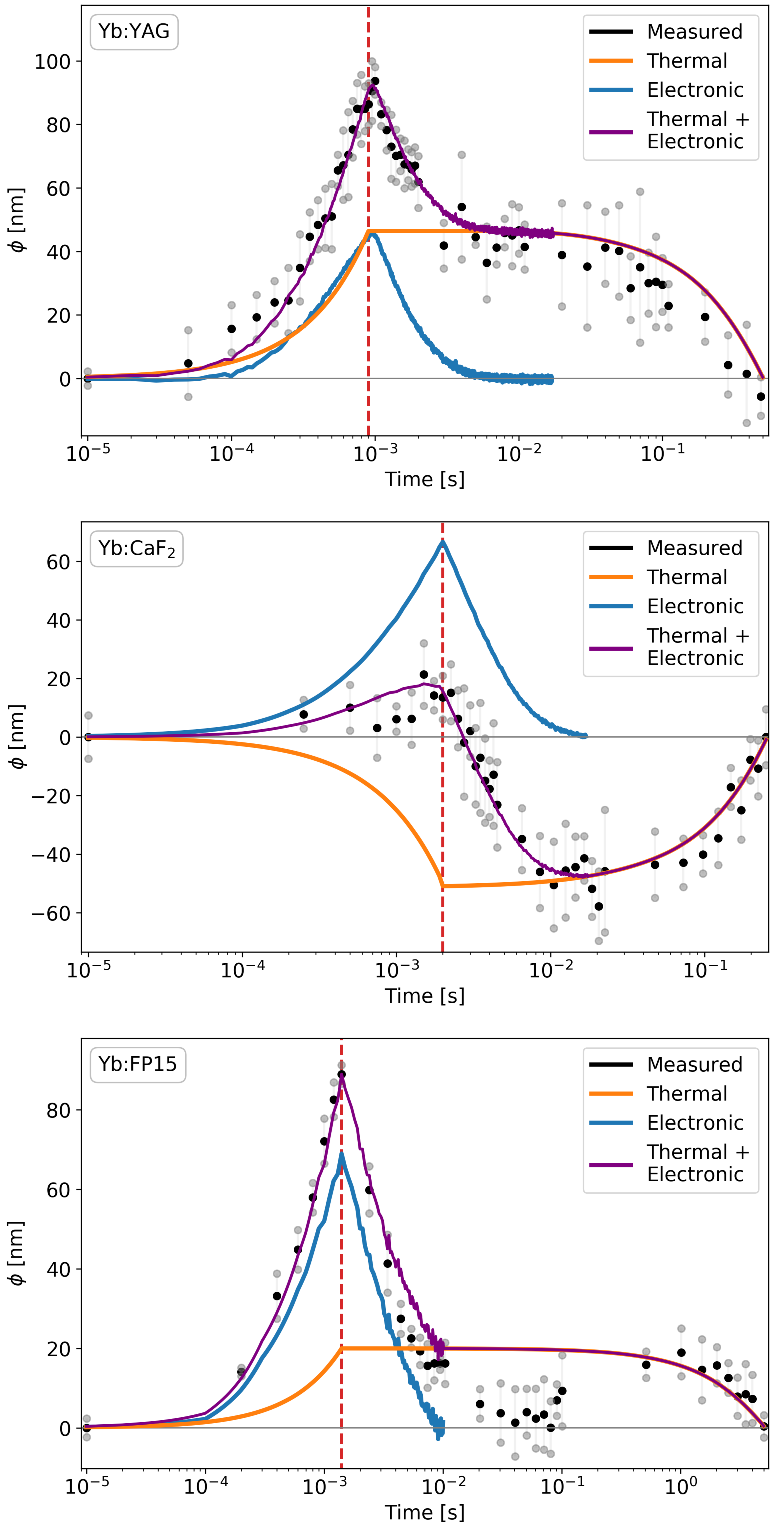

Figure 23: Temporal comparison of the measured (black) and superposition (purple) of the thermal (orange) and electronic (blue) OPDs for Yb:YAG (top), Yb:CaF$_2$ (center), and Yb:FP15 (bottom). The temporal profiles display the magnitude of the OPD profiles generated per pump pulse, shown along a logarithmic time axis. The dashed red lines designate the end of the pump pulse and the start of the OPD relaxation.

To complete the temporal model of the electronic contributions, the temporal profiles of the thermally induced (detailed in section 3.1.2) and electronically induced (using Eq. 53, with the population inversion extracted from temporal gain measurements) OPDs were superimposed by setting the polarizability difference as the variable to be solved. Similarly to the procedure utilized to recover the photoelastic constant C_r' values in section 3.1.2, the combined profiles (purple curves in Fig. 23) were compared to the results from the interferometric measurements and the polarizabilty difference values ($\Delta\alpha$, given in units of 10^{-26} [cm^3]) were extracted: 1.93 ± 3.7 % for Yb:YAG (consistent with the literature value of 1.95 ± 12.8 %[55]), 0.79 ± 2.9 % for Yb:CaF$_2$, and 1.15 ± 6.8 % for Yb:FP15.

As evident in Fig. 23, the electronic contributions (blue) to the pump-induced OPD profiles generated with each pump pulse are far from negligible when compared to the thermal contributions (orange). For Yb:YAG, both contributions share the same sign and nearly the same amplitude. For Yb:CaF$_2$, the amplitudes of the thermal and electronic contributions are similar but opposite in sign, resulting in a complete compensation of the pump-induced OPDs per pump pulse near $t \approx \tau_\mathrm{p}$. For Yb:FP15, the electronically induced OPDs per pump pulse are nearly three times larger in amplitude than the thermally induced OPDs. Here, due to the reduced value of the total thermo-optic coefficient in Yb:CaF$_2$ and Yb:FP15 – caused by the balancing of the negative $\mathrm{d}n/\mathrm{d}T$ with the positive thermal expansion term – the role of the electronic contributions for the total pump-induced OPDs is significantly increased.

3.1.4 Pump-Induced Wavefront Aberrations

During the time frame of laser pulse amplification (near $t = \tau_\mathrm{p}$), the incident seed pulse passing through the pumped active material experiences the spatio-temporal superposition of both thermal and electronic contributions per pump pulse, along with an additional thermally induced OPD profile due to the steady-state temperature gradient within the thermalized material. The difference in temperature between the unpumped and thermalized states on the edges of the material additionally produces a phase offset that, although initially lost within the interferometric results due to the phase unwrapping procedure, can be recovered by correcting the baseline of the measured OPD profiles using the verified thermal simulations.

In Fig. 24, by removing the thermally induced OPDs (orange) – from both the thermalized state and the incident pump pulse – from the total pump-induced OPDs (black), the spatial profile of the electronic contributions (blue) are revealed, which closely resemble the spatial profile of the calculated electronic contributions (red, using Eq. 53) with the spatial form extracted from fluorescence profile measurements. Hence, the total pump-induced OPD profiles are characterized by a spatial and temporal superposition of the individual thermal and electronic contributions, which can be directly modeled by thermal simulations and measurements of the single-pass gain and fluorescence profile.

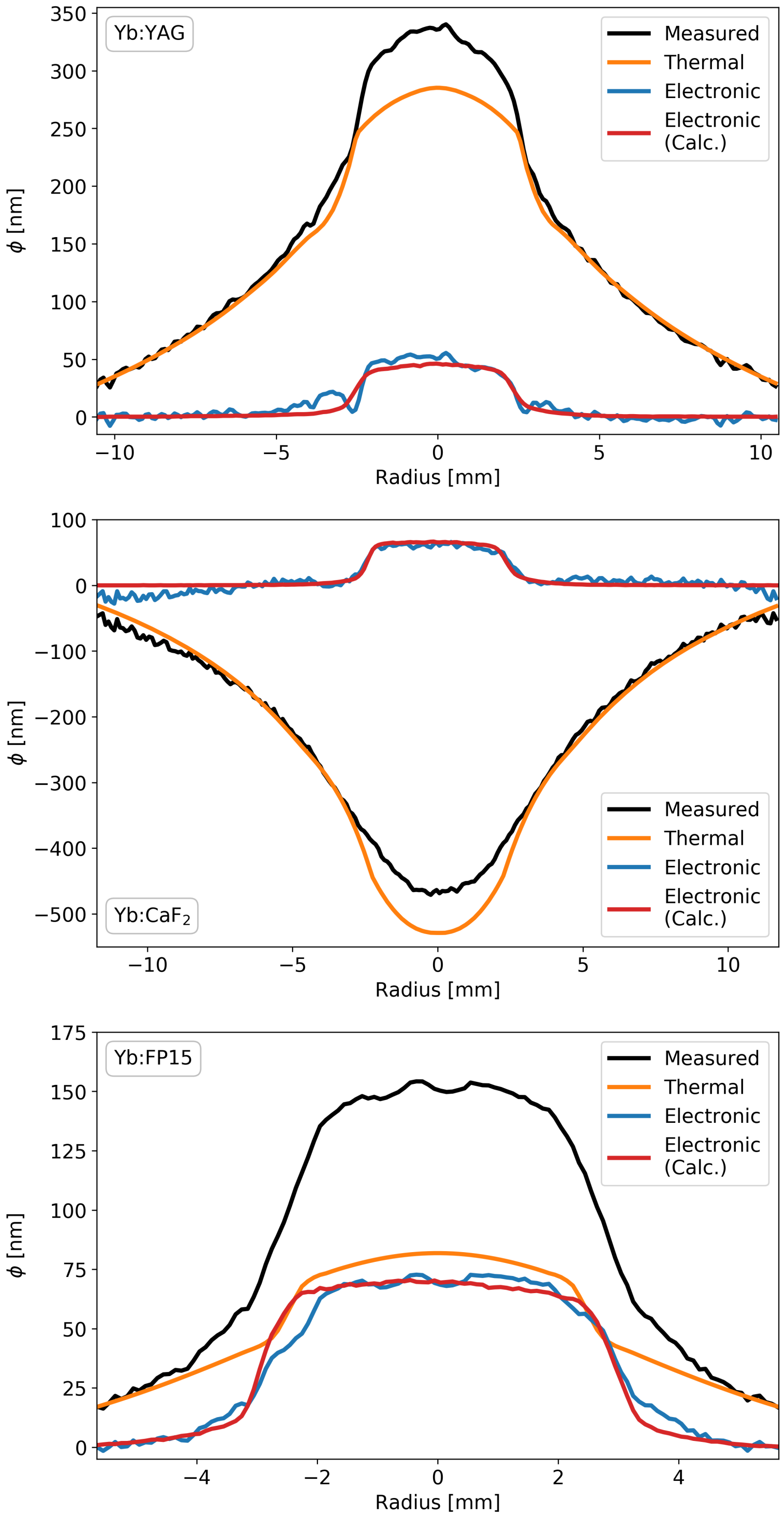

Figure 24: Spatial profiles of the measured (black), thermal (orange), and electronic (blue; calculated - red) OPDs at the end of the pump pulse for the thermalized Yb:YAG (top), Yb:CaF$_2$ (center), and Yb:FP15 (bottom). By removing the thermal (orange) OPD profile from the measured (black) OPD profile, the spatial profile of the electronic OPDs (blue) is revealed, which matches the calculated electronic OPD profile (red) for each considered material.

To determine the effect of the total OPD profile on the wavefront of an incident seed pulse, the spatial profile can be separated into low and high frequency terms. The low frequency term of the pump-induced wavefront aberrations is designated by a parabolic curvature (i.e., defocus), which was fitted within the pumped region of the OPD profiles previously given in Fig. 24. Here, an effective focal length (EFL), corresponding to the strength of the defocus, was set as the variable to be solved. The determined EFL values were $31\,\mathrm{m} \pm 1.4\,\%$ for Yb:YAG, $-35\,\mathrm{m} \pm 0.5\,\%$ for Yb:CaF_2, and $53\,\mathrm{m} \pm 1.5\,\%$ for Yb:FP15. Subtracting the low frequency defocus term (blue) from the total OPD profile (black) in Fig. 25 results in the form of the high frequency spatial phase distortions (red) that aberrate the wavefront of the amplified seed pulse passing through the pumped material.

For Yb:YAG and Yb:FP15, these phase distortions imprint an oscillating OPD pattern on the incident wavefront that changes signs from the center to the edge of the pump profile. For the case of high energy Yb^{3+}-based amplifiers, the low gain of broadband Yb^{3+}-doped materials leads to the requirement of up to 20[14,71] passes through the pumped region. Consequently, the peak-to-valley amplitudes of these phase distortions of $\sim 0.03\,\lambda$ (with $\lambda = 1030\,\mathrm{nm}$) add up with each pass and significantly deteriorate – by introducing alternating regions of focusing and defocusing, as evident in Fig. 16 – the spatial profile throughout the long propagation distances typically found in high energy multi-pass amplifiers. For Yb:CaF_2, however, the compensation of the electronic and thermal aberrations per pump pulse heavily suppresses the high frequency spatial phase distortions, leaving a defocus term that can be easily attenuated or removed in the laboratory via corrective curved surfaces or by implementing a counteracting defocus with an imaging setup. With the knowledge gained from this comprehensive investigation on pump-induced wavefront aberrations, a model can be constructed to optimize the resulting spatial profile of an amplified seed pulse – passing through, for example, a joule-class multi-pass amplifier – within any laser system employing Yb^{3+}-doped active materials.

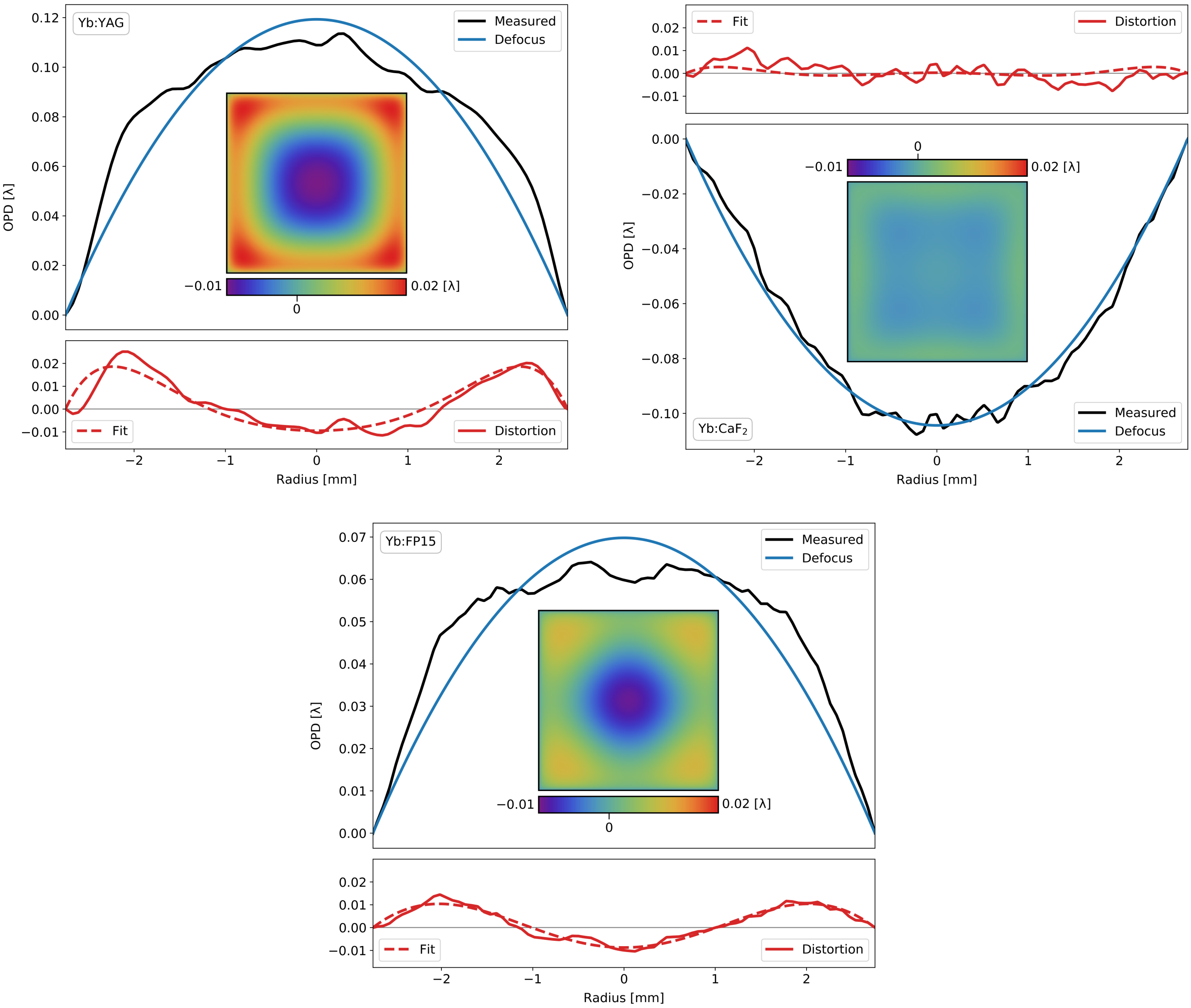

Figure 25: Residual spatial phase distortions for a single pass at the end of the pump pulse for the thermalized Yb:YAG (top, left), Yb:CaF$_2$ (top, right), and Yb:FP15 (bottom). The phase distortions (red) within the pumped region – with the calculated spatial profiles displayed in the rainbow color scale – were isolated from the total pump-induced OPD profiles (black) by removing the parabolic defocus component (blue) with a fitted EFL (31 m for Yb:YAG, -35 m for Yb:CaF$_2$, and 53 m for Yb:FP15). A fit of the phase distortions is additionally displayed (dashed, red) for clarity. The amplitude scale is given in waves with $\lambda = 1030$ nm.

3.1.5 Spatial Profile Degradation in a Joule-Class Multi-Pass Amplifier

To produce the population inversion necessary for laser pulse amplification into and above the joule-regime, high pump densities are required that can lead to a significant deterioration of the spatial profile of the amplified seed pulse as a result of thermally and electronically induced wavefront aberrations (section 3.1.4). The high spatial frequencies generated within the seed beam profile consequently limit the final fluence and focusability of the high peak power laser system. In addition to the pump-induced OPD profiles, however, the strong thermal gradient within the pumped active material can lead to spatial deformations and energy loss via spatially inhomogeneous stress-induced birefringence[22], which locally distorts the polarization – and, therefore, the spatial profile and energy after interacting with polarization-sensitive components – of the amplified beam, along with a reshaping of the transverse gain profile[19], due to thermally induced spatial variations in the absorption and emission cross-sections. Furthermore, a spatially inhomogeneous amplified spectrum, due to the local changes in the emission cross-section, deforms the spatio-temporal profile upon pulse compression, resulting in a spatially varying pulse duration[92,93] along the near field beam profile. Ultimately, a strong thermal gradient within the pumped active material can, in the worst case, lead to material fracture due to thermal stress and therefore sets a hard upper limit on the repetition rate of the full laser system. To model the effect of the pump-induced influences on the spatial profile and to prevent permanent material damage in a joule-class amplifier, the full 3D spatio-temporal thermal profile of the pumped active material must be characterized.

3D Spatio-Temporal Thermal Profile Characterization

Measurements of the temperature distribution within the pumped active material are often restricted to averaged profiles along the length of the material[94] or, due to the high emissivity of the pumped active materials, only surface thermal profiles, which provide largely inadequate information on the strength of the thermal gradient deep within the strongly pumped active material. Scanning methods[95], in which a 3D thermal profile can be extracted, are currently inapplicable to high energy laser amplifiers such as those at POLARIS, due to the very low repetition rates and large active material radius and thickness within the laser system.

However, using the calibrated measurement method along with knowledge of the doping-dependent material parameters and inversion-corrected pump depletion described in sections 2.4.2 and 3.1.2, the complete 3D spatio-temporal thermal profile of the pumped active material in a Yb^{3+}-based joule-class multi-pass amplifier – such as the “A4” amplifier within the POLARIS[14] laser system – can be characterized by the verified numerical thermal model.

Within the A4 amplifier, a complex double-sided 3D pumping configuration[96], depicted in Fig. 26, is utilized, in which the position of each of the 40 pump spots are individually adjusted to obtain the designated pump profile. The 2.7 ms pump pulses are generated from

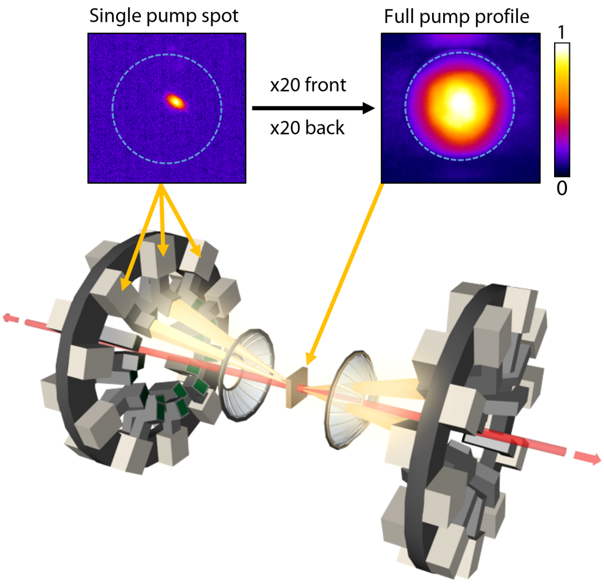

Figure 26: Schematic[97] of the 3D pumping configuration of the Yb:FP15-based (perimeter in blue) A4 multi-pass amplifier at POLARIS with thermal images of an example of a single pump spot (top left) and the full pump profile (top right). The colorbar is scaled according to the normalized pump beam intensity.

2.5 kW laser diode modules delivering an average beam size of 7.2 mm × 3.1 mm FWHM and a total beam diameter of 21 mm, containing a combined energy of over 250 J. The seed beam is amplified within the pumped and water-cooled Yb:FP15 active material (45 mm diameter, 13 mm thickness) up to 7 J in 9 passes, with the pump beam orientation set to produce a flat-top-like transverse gain profile.

The spatial profile of each pump beam on both the front and back side of the active material was recorded by the triggered FLIR P620 thermal infrared imaging camera. Here, the individual thermal profiles (Fig. 26, top left) generated on the material surfaces are quasi-static within the thermal camera's integration time, due to the high emissivity and very low thermal conductivity[29] of Yb:FP15, and can therefore be utilized to adequately recover the individual spatial profiles of the 40 pump beams. The beams were each defined by an intensity profile exhibiting an elliptical Gaussian-like spatial distribution with orthogonal beam radii ω_{max} and ω_{min}, central positions x_{c} and y_{c}, rotation angle θ with respect to the xy-frame, incidence angles ϕ_x and ϕ_y, pump pulse duration τ_{p}, energy E_i, and numerically calculated (Eqs. 20 – 21) pump depletion profile $A_i(z)$:

$$
\begin{aligned}
I(x,y,z,t) = \sum_{i=1}^{40} E_i \cdot \exp\Bigg[-\Bigg(\left(\frac{\cos(\theta_i)\cdot X_i + \sin(\theta_i)\cdot Y_i}{\omega_{\mathsf{max},i}} \right)^2 \\
+ \left(\frac{-\sin(\theta_i)\cdot X_i + \cos(\theta_i)\cdot Y_i}{\omega_{\mathsf{min},i}} \right)^2 \Bigg) \Bigg] \cdot A_i(z) \cdot \mathrm{rect}\left(\frac{t}{\tau_{\mathsf{p}}}\right),
\end{aligned}
\tag{61}
$$

$$
\text{where } X_i = x - (x_{\mathsf{c}} - z\cdot\tan(\phi_x));\; Y_i = y - (y_{\mathsf{c}} - z\cdot\tan(\phi_y)).
$$

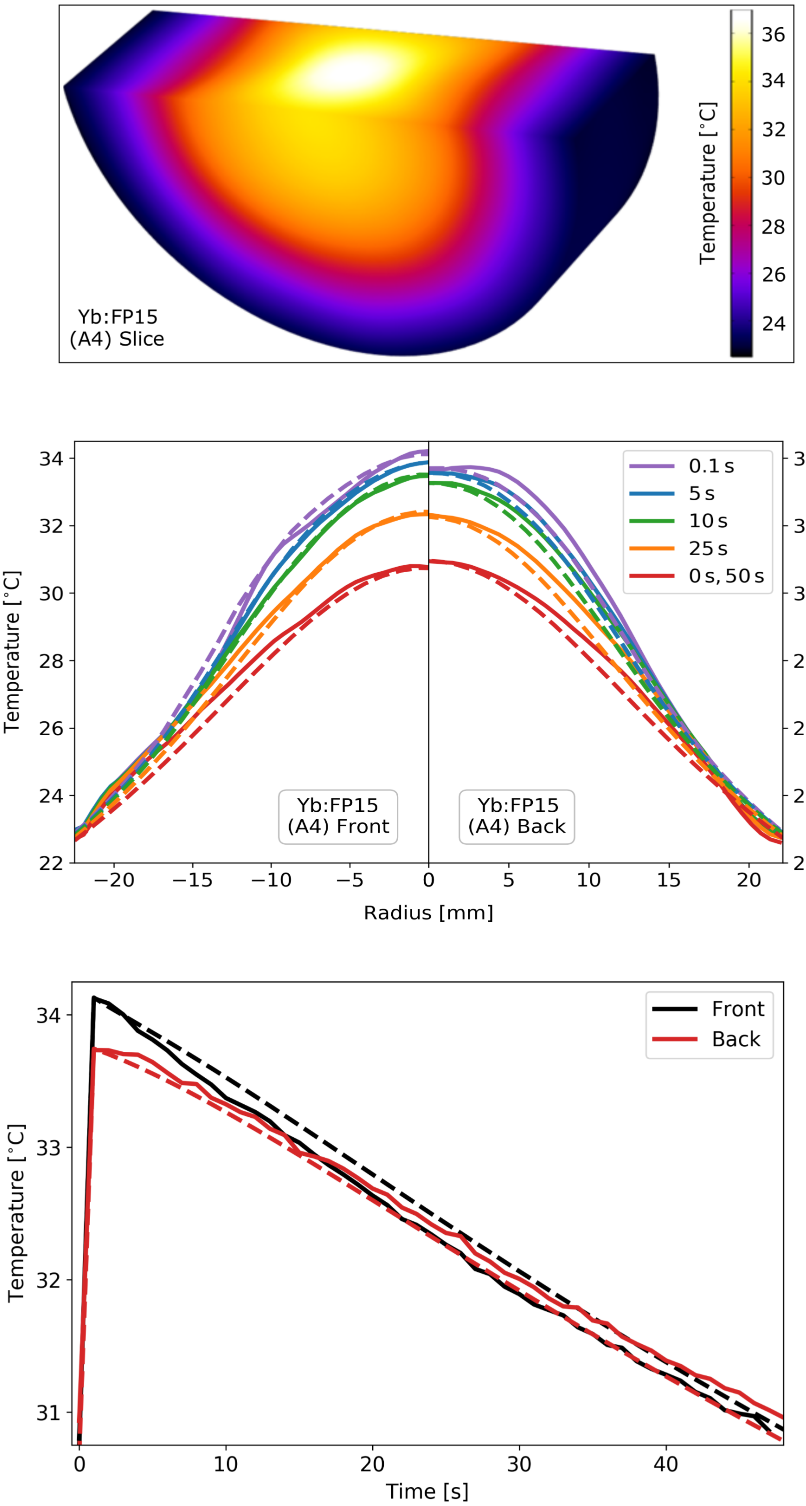

Figure 27: Comparison of measured (solid) and simulated (dashed) thermal profiles of the pumped and thermalized Yb:FP15 within the A4 amplifier. A slice through the pumped Yb:FP15 model in COMSOL is shown (top). The front and back Yb:FP15 profiles are displayed (center) for times 0 (directly before the 2.7 ms pump pulse), 0.1, 5, 10, 25, and 50 seconds within the pump cycle (rep. rate 0.02 Hz). The temperature on the front and back surface centers of the Yb:FP15 material is plotted (bottom) throughout the pump cycle.

Based on the techniques described in section 2.4.2, a numerical thermal model was constructed using the 40 individual beam intensity profiles $I(x, y, z, t)$ in Eq. 61 as the input for the pump beam. Surface temperature measurements using the thermal infrared imaging camera of the fully pumped and thermalized Yb:FP15 (Fig. 26, top right) on both the front and back surfaces, as seen in Fig. 27 agree well with the simulated thermal profiles with an RMS discrepancy of less than 1.5% of the peak temperature throughout the entire pump cycle.

With the verified results of the thermal model, the inner temperature distribution of the pumped Yb:FP15 can be accessed and compared to the measurable surface thermal profiles. In Fig. 28, it is evident that the present pump configuration, designed to generate a homogeneous transverse gain profile on the front and back surfaces, leads to a thermal gradient (temperature difference ΔT between radius $= 0\,\mathrm{mm}$ and radius $= \pm 22.5\,\mathrm{mm}$) in the middle of the active material that is 24% larger than those on the front and back surfaces. Consequently, the thermal contributions to the pump-induced OPD profile imprinted onto the wavefront of the amplified seed pulse within each material pass along with the thermal stress are significantly higher than otherwise anticipated when considering the measurable surfaces. With this 3D spatio-temporal thermal profile characterization[97], the influences that lead to spatial profile degradation can be accurately modeled and controlled, thereby increasing the final fluence and repetition rate in joule-class multi-pass amplifiers.

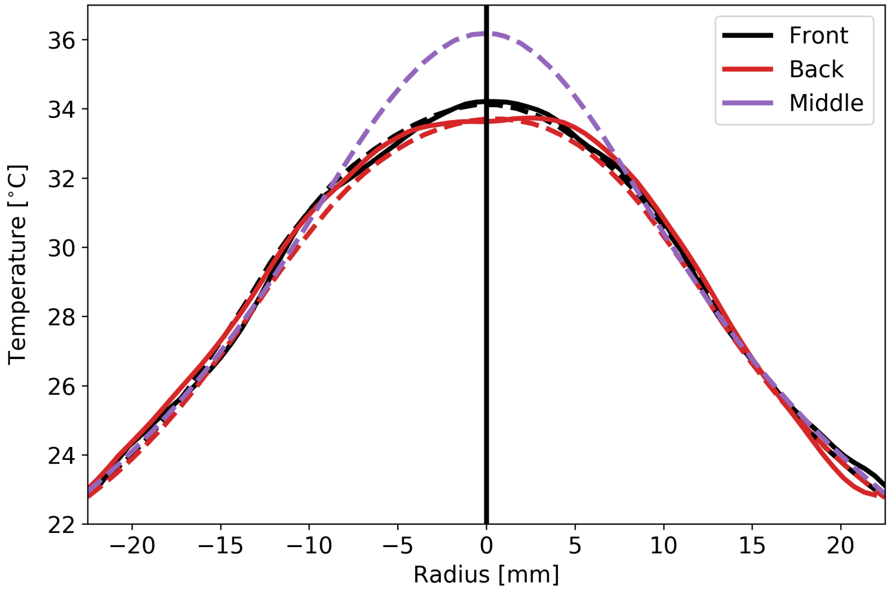

Figure 28: Comparison of the measured (solid) and simulated (dashed) front, back, and middle thermal profiles of the pumped Yb:FP15 within the A4 amplifier. The results of the verified numerical simulation reveal a strong thermal gradient within the material that is inaccessible from the surface thermal measurements.

Pump-Induced Wavefront Aberrations at the Joule-Level

By coupling the knowledge of the thermal and electronic contributions to the pump-induced wavefront aberrations with the verified numerical thermal simulation described in sections 3.1.2 and 3.1.4, a powerful tool can be created to model and optimize the output beam profile of a seed pulse amplified within a high energy laser amplifier. For the case of the joule-class, multi-pass “A4” amplifier, with the spatio-temporal thermal profile characterized in section 3.1.5, a Gaussian-shaped seed beam entering the amplifier experiences a spatial transformation (seen in Fig. 16) into a donut-like pattern throughout propagation, due to the high frequency spatial phase distortions produced by the pump-induced OPDs, as varying portions of the beam profile are inhomogeneously focused and defocused. Here, the local fluence within these focused regions can become high enough to permanently damage the active material or compressor gratings within the petawatt-class CPA configuration of POLARIS. This consequence is commonly avoided in such laser systems by decreasing the total fluence, i.e., setting an undesirable upper limit on the final energy or increasing the beam diameter – that, as a result, further worsens the impact of the pump-induced wavefront aberrations on the beam profile. Instead, however, a novel approach can be implemented, in which the pump profile is adapted to compensate the effects of the high frequency spatial phase distortions, leading to a more homogeneous amplified beam profile, even in the absence of the ideal flat-top transverse gain profile.

To demonstrate this in the context of a joule-class laser pulse, the 40 individual pump beams of the A4 amplifier were configured to produce beam profiles for two pump cases, as seen in Fig. 29. In the initial (blue) case, the pump distribution was optimized solely according to the gain profile. Following the discussion in section 3.1.4, the resulting spatial phase distortions form with a peak-to-valley amplitude of nearly 0.4 λ (with $\lambda = 1030\,\text{nm}$) after 9 passes that vary in sign across the beam radius. To determine the impact on the

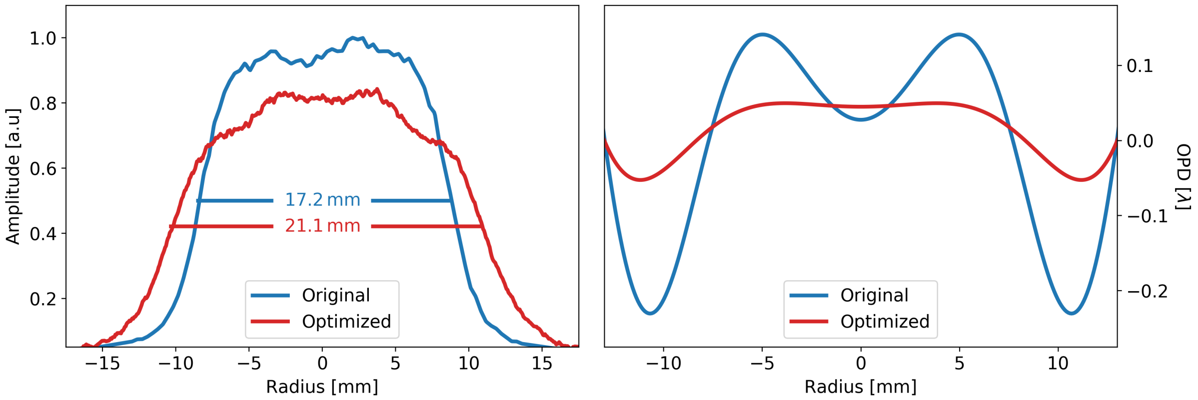

Figure 29: Two pump profile cases (left) for the A4 amplifier, in which the gain distribution (blue) and the pump-induced wavefront aberrations (red) are considered. The resulting spatial phase distortion profiles (right) are given in units of waves, with $\lambda = 1030\,\text{nm}$.

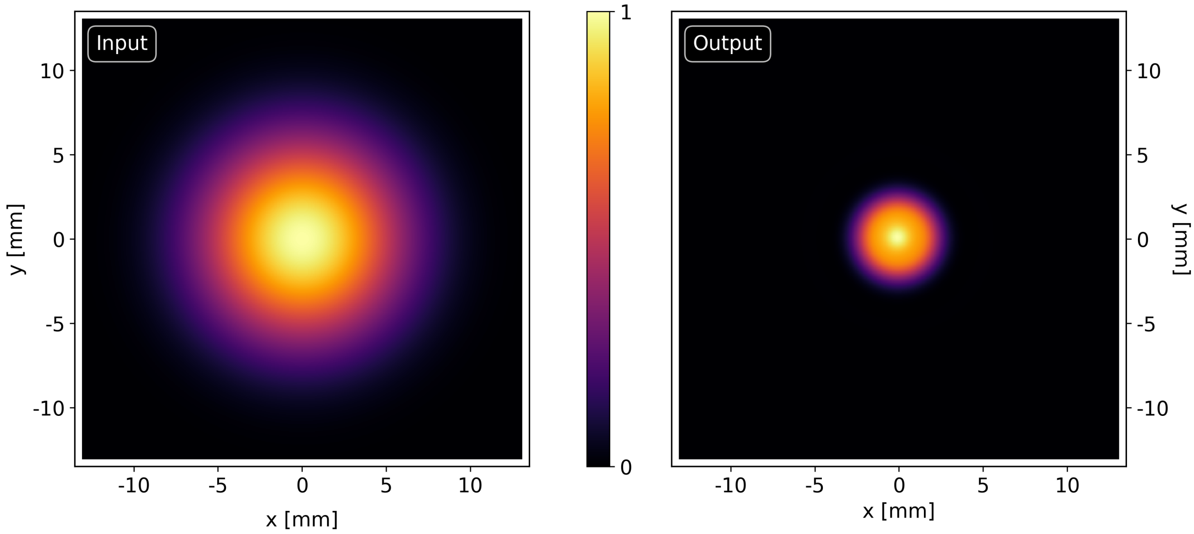

Figure 30: Simulated beam profiles at the input (left) and output (right) of the A4 amplifier with a total pump profile optimized for gain homogeneity. As the initially collimated beam propagates within the 9-pass joule-class amplifier, a strong focusing effect is produced due to the large thermal contributions to the pump-induced OPD profile.

amplified spatial profile, a numerical model of the beam propagation within the 9-pass A4 amplifier was developed. The simulated A4 amplifier is initially seeded by a collimated 9 mm $1/e^2$ radius Gaussian-like beam (Fig. 30, left). Here, the large temperature gradient formed by the 264 J pump pulse generates a thermally induced OPD profile with an effective focal length of f = 66 m for the 9 material passes. After the total propagation distance of 33.5 m within the A4 amplifier, the beam size (Fig. 30, right) is significantly reduced, bringing the fluence of the amplified pulse well above the maximum operating range of 3 J/cm^2.

The impact of the thermally induced OPD profile can be mitigated by introducing a telescope at the entrance of the amplifier, with the distance between the two lenses adjusted to provide a divergence corresponding to a focal length of f = -15 m. The combined effect of the induced divergence, spatial gain narrowing, and the thermally induced OPD profile allows for a near recovery the initial beam size at the final pass. However, the large amplified beam profile is also susceptible to the full wavefront aberrations, with positive OPD profiles for both thermal and electronic contributions in Yb:FP15, produced by the flat-top-like pump profile. As seen in Fig. 31, the alternating signs of the wavefront aberrations across the beam diameter begin to shape the beam profile during the high energy passes within the amplifier. At the amplifier output, the spatial phase distortions displayed in Fig. 29 (blue) focus the inner and outer portions of the beam profile into a localized, ring-like structure. Here, the maximum achievable laser pulse energy is limited by the high fluence within the ring.

To optimize the beam profile according to the pump-induced wavefront aberrations, the 40 individual pump beams must be configured (Fig 29, red) to counteract the sharp OPD variations across the spatial profile of the amplified beam. Here, regions of positive and negative high frequency wavefront aberrations can be compensated by introducing controlled changes in the spatial pump – and, consequently, the population inversion profile – thereby directly (via Eq. 53) impacting the amplitude of the electronic contributions. In this scenario, the pump beam area has been expanded by nearly 20%, and an additional peak in the pump intensity of 15% within the radius $r = \pm 5\,\mathrm{mm}$ was introduced to fill the local reduction in the OPD profile (Fig. 29, blue). As a result, the total form of the OPD profile more closely resembles the parabolic defocus term, with a near-complete compensation of the high frequency spatial phase distortions (Fig 29, red).

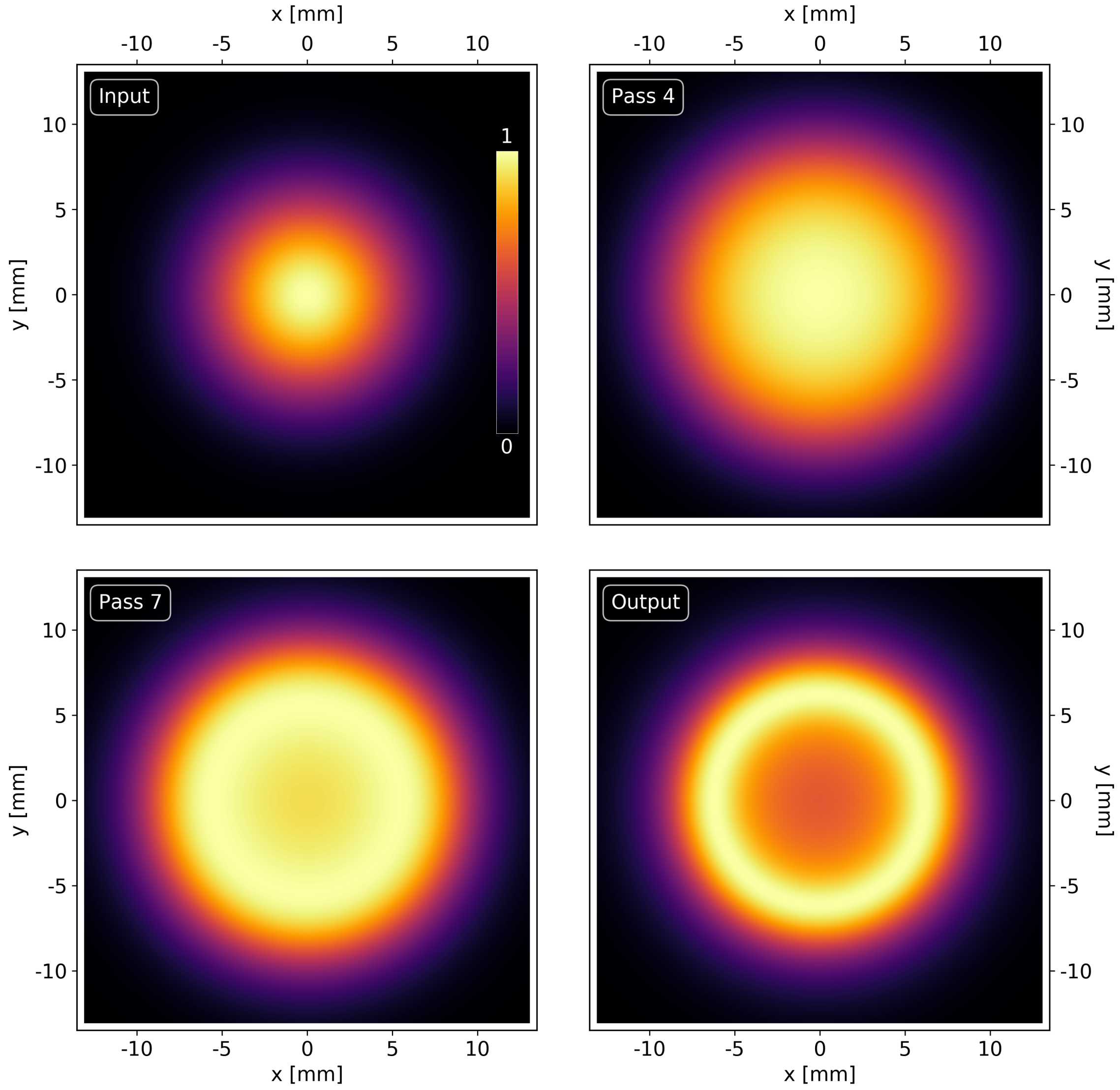

Figure 31: Simulation of an initially Gaussian-like beam (top left) propagating through the joule-class A4 amplifier. The beam profile intensity for each subplot has been normalized to improve the visibility. The spatial beam quality is maintained until approximately 20 m of propagation, in which the inner and outer regions of the beam profile begin to concentrate in a ring-like pattern. At the amplifier output (bottom right), the fluence homogeneity is significantly degraded by the pump-induced wavefront aberrations.

The simulation was recomputed to model the expected output beam profile with the optimized pump configuration. The initially Gaussian-like beam, as seen in Fig. 32, maintains its spatial beam quality as it propagates through the 9-pass amplifier. Additionally, the compensation of the wavefront aberrations along with the high divergence and gain narrowing within the amplifier leads to an increase in the fluence homogeneity at the amplifier output. Although the change in the pump profile between the original and optimized cases reduces the total gain (via Eq. 25) by approximately 20%, the improved homogeneity allows the seed

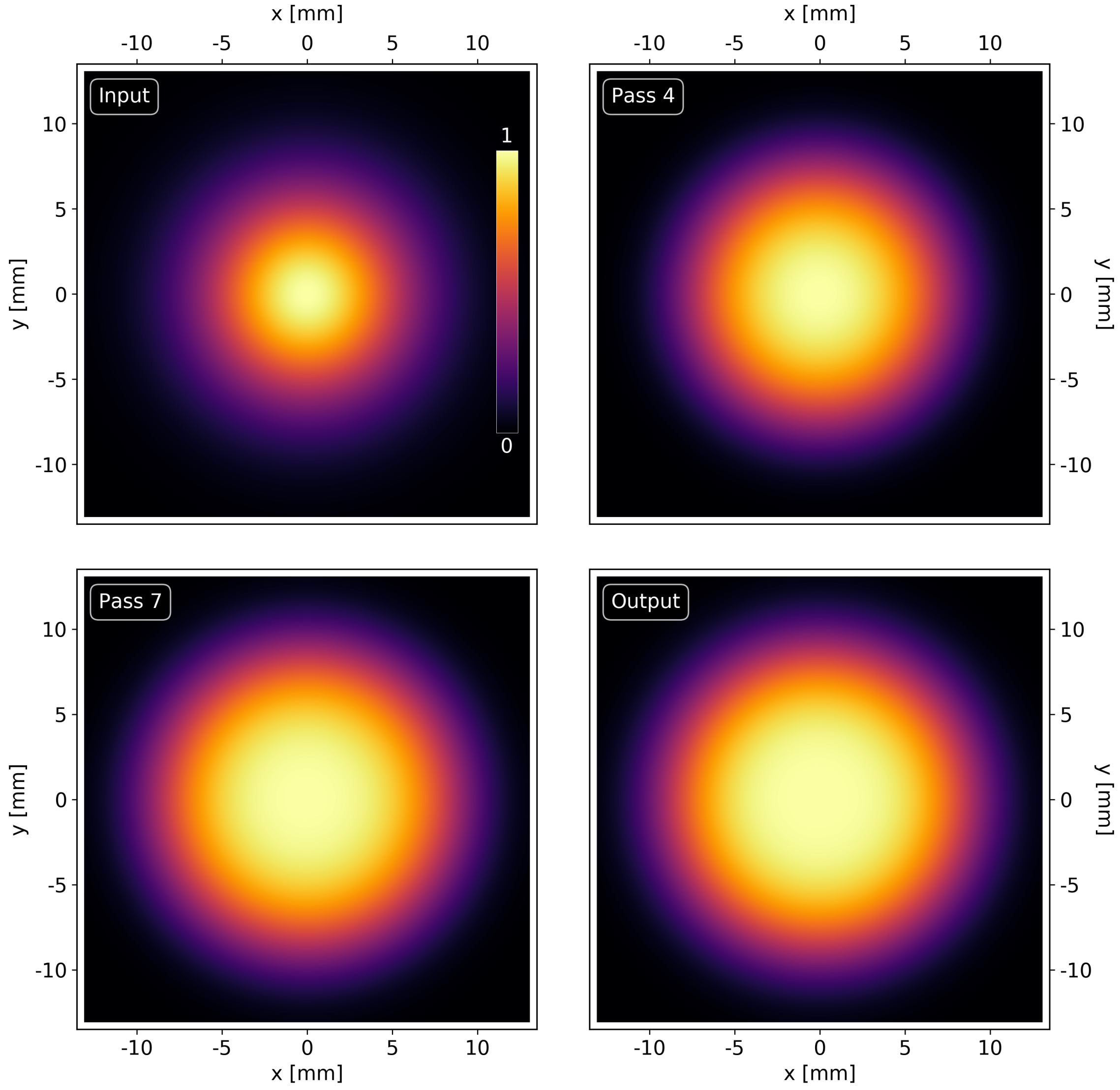

Figure 32: Simulation of an initially Gaussian-like beam (top left) propagating through the joule-class A4 amplifier with a pump beam profile corrected for the pump-induced wavefront aberrations. The beam profile intensity for each subplot has been normalized to improve the visibility. Contrary to the case in Fig. 31, the spatial beam quality is maintained throughout the entire propagation distance. Furthermore, the fluence homogeneity is improved with respect to the input beam, due to the compensation of the high frequency spatial phase distortions, in addition to the effects of high divergence and spatial gain narrowing.

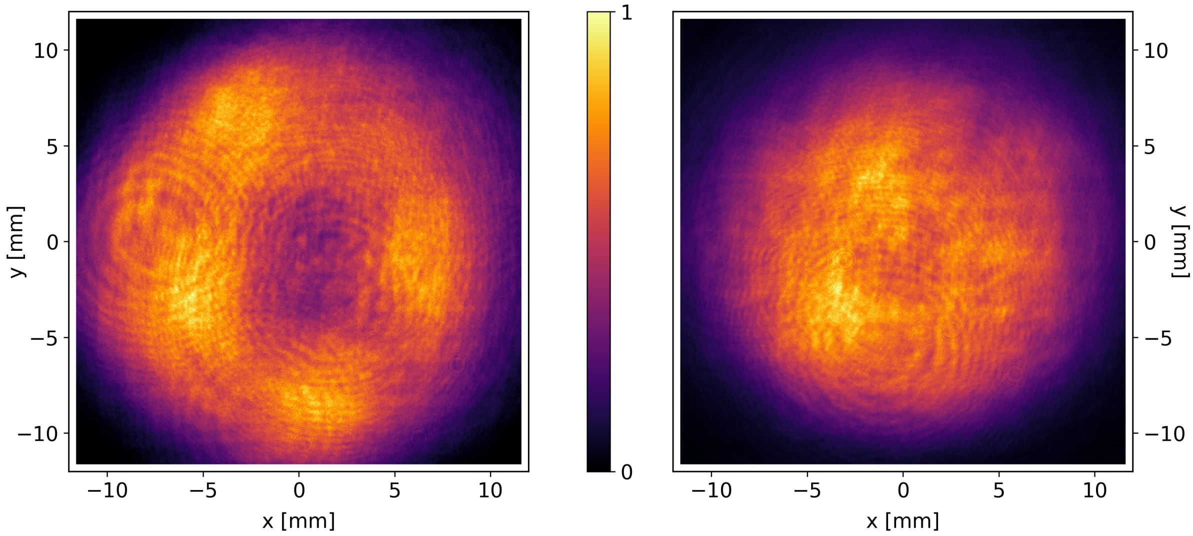

Figure 33: Beam profiles at the output of the A4 amplifier for pump profiles optimized for gain homogeneity (left) and spatial phase distortion mitigation (right).

fluence to be increased by 40% to achieve a final energy at least 15% higher than the original case for the joule-class amplifier operating at a maximum fluence of 3 J/cm^2.

With the knowledge gained from the results of the beam propagation simulation, the optimized pump configuration was implemented on the 9-pass A4 amplifier. As seen in Fig. 33 for the original case, the orientation of the 40 pump beams with respect to the spatial gain profile resulted in pump-induced OPD profiles that transformed the Gaussian-like input beam into a ring-like structure after amplification (Fig. 33, left). Altering the pump beams (Fig. 29) to compensate for the high frequency component of the OPD profiles enabled a significant improvement (Fig. 33, right) in the fluence homogeneity of the now amplified flat-top-like beam, which is used to seed the final “A5” POLARIS amplifier[14] with output pulse energies in excess of 50 J. Here, the compensation of pump-induced wavefront aberrations is a necessary step to optimize the spatial profile of the amplified pulses, particularly at the joule-level and beyond, thereby increasing the focusability and maximum achievable energy within high peak power laser systems.

3.2 Temporal: Post-CPA Pulse Compression

An energy scaling of a petawatt-class laser system is a promising, albeit costly process of increasing the peak intensity of the laser pulse. To restrict the fluence below the LIDT of the optical components within the laser chain, the final amplifiers, compressor, and beamline optics must be enlarged to support the expanded amplified laser beam. Additionally, as seen in section 3.1.5, the influences of pump-induced wavefront aberrations cannot be neglected for these large diameter beams, particularly in high energy multi-pass amplifiers.

Alternatively, the laser pulse intensity can be increased by further shortening the pulse duration, which is limited by the unamplified laser pulse bandwidth, the gain bandwidth of the active materials, and the stretcher and compressor designs within the CPA chain. In the context of ultrashort Yb^{3+}-based lasers, for example, approximately three times the energy is required to achieve the same peak power as that of Ti:Sapphire systems, due to the significantly smaller spectral bandwidth. Techniques such as cross-polarized wave generation (XPW), already used in high peak power laser systems for contrast enhancement[98], can also be employed for pulse shortening by a factor of $\sqrt{3}$[98]. Here, however, the conversion efficiencies on the order of 10% results in an overall reduction of the peak power. Decreasing the pulse durations of ultrashort Yb^{3+}-based laser systems while maintaining the high pulse energies requires a low-loss spectral broadening mechanism, such as nonlinear self-phase modulation (SPM, described in section 2.4.3), which can be readily enabled by the substantial laser pulse intensities within the system. Through SPM, the spectral bandwidth can be increased and the laser pulse subsequently compressed to pulse durations shorter than the initial value using, for example, a compact chirped mirror pair. With this method, optimizing the laser towards higher peak powers by factors of two or more can be accomplished directly after the CPA chain, thereby bypassing the costly necessity of enlarging the back-end of the laser system.

Thus far, spectral broadening techniques post-CPA have been typically conducted in the far field regime, in which the laser pulse is focused into a pressure-controlled gas[99] to generate sufficient self-phase modulation. Although pulse compression of a 200 TW pulse by a factor of two[100] has also been successfully achieved in a laser-generated plasma wakefield, the final intensity remained relatively unchanged due to the output energy transmission of approximately 50%. Several further disadvantages limit the applicability of this approach to petawatt-class laser systems, including a degradation of the spatial beam quality and temporal intensity contrast during laser pulse propagation within the gas or plasma.

Recently, however, a class of highly nonlinear materials has been reported[101] that provides the potential to accomplish spectral broadening in the near field regime[102], while retaining the energy and spatial beam quality of the high peak power laser pulse. Here, near field post-CPA pulse compression offers a simple, low-cost method of significantly optimizing[103] the pulse durations of state-of-the-art laser systems.

3.2.1 Characterization of Highly Nonlinear, Transparent Media

To generate strong self-phase modulation and increase the peak power of the laser pulse after subsequent pulse compression without the multiple disadvantages of using a gas or plasma, low-absorption thin plastics with high nonlinear refractive indices can be employed. In this section, a small group of commercial plastics including allyl diglycol carbonate (CR39[104]), polyethylene terephthalate (amorphous PET[105]), polymethyl methacrylate (PMMA[106]), and cellulose acetate (CA[107]) are investigated that exhibit nonlinear refractive indices larger than that of common optical glasses[108,109] (e.g., fused silica for the VIS-IR regime) and several orders of magnitude larger than the gases[110,111] (Argon, Neon) utilized for SPM in hollow-core fibers[112,113]. Consequently, these plastics films can be used for self-phase modulation outside of the focal plane – even in the near field for intense laser pulses – with thicknesses of approximately 1 mm to minimize absorption losses. Furthermore, the high damage threshold of 5 TW/cm^2 [114,115], minuscule cost, and abundance in large sizes ($>$10 cm) at a high optical quality make the plastics described within this section promising candidates as nonlinear materials for post-CPA pulse compression.

To determine the optimum sample for the post-CPA pulse compression method, the nonlinear refractive indices n_2 must first be characterized. The commonly utilized Z-Scan method[51,116,117] is not suitable for n_2 measurements in thin nonlinear plastics, as the high intensities required to induce a significant nonlinear phase accumulation within the minuscule thickness of the material can heavily influence the amplitude of the extracted n_2 values, e.g., due to long-term refractive index modifications[118] and thermal effects. Instead, the degenerate four-wave-mixing (DFWM) technique[119], with the measurement setup depicted in Fig. 34, can be applied as an appropriate and simple alternative for the low-absorption materials[120,121]. Here, a reduced energy (75 µJ), 130 fs laser pulse from the first POLARIS

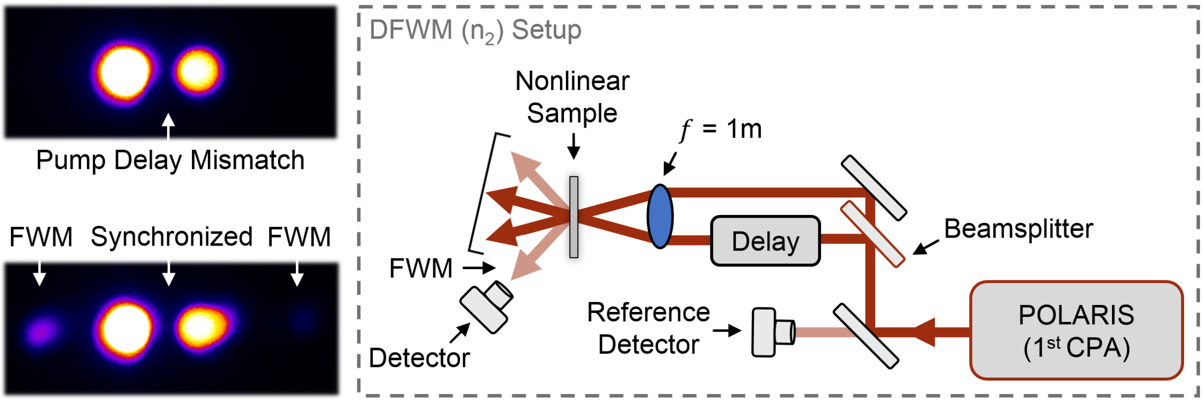

Figure 34: Schematic of the DFWM-based measurement setup for the nonlinear refractive indices of the thin plastics. A laser pulse from 1st POLARIS CPA is split into two and focused into the nonlinear sample. The temporally synchronized pump beams generate a background-free DFWM signal that can be correlated to the n_2 value using a known reference.

CPA system is split into two with a beamsplitter and focused (focal length $f = 1\,\mathrm{m}$) into the nonlinear sample with a delay stage in one arm of the setup to correct for differences in the optical path between the two pump beams. The DFWM signal, with each photon generated using two photons from one pump beam and one photon from the second, is emitted from the nonlinear material at an angle from the pump beams due to momentum conservation[119] – analogous to the case of idler generation in noncollinear OPA (Fig. 7 in section 2.3.2). Here, the background-free DFWM yield can be measured with a detector (Thorlabs DET36A/M) and corrected for minor fluctuations in the pump beam energy using an additional reference detector at the entrance of the setup. Furthermore, with the DFWM-based n_2 characterization technique, absolute intensity values of the pump pulse are not required. Using a reference sample with a well-known nonlinear refractive index amplitude $n_{2,\mathrm{ref}}$ and thickness L_{ref}, the ratio between the DFWM yield of the known (A_{ref}) and unknown (A) materials can be utilized to determine the n_2 value of the desired sample with thickness L via[119,120]:

$$n_2 = n_{2,\mathrm{ref}} \cdot \frac{L_{\mathrm{ref}}}{L} \cdot \left(\frac{A}{A_{\mathrm{ref}}}\right)^{0.5}, \tag{62}$$

under the assumption of thin, low-absorption materials, which is fulfilled by the samples in this investigation. Before the DFWM technique is applied to measure the n_2 values of the nonlinear plastics, however, the reliability of the setup must be validated by observing the scaling behavior of the DWFM signal. Using fused silica as the well-known reference sample, the characteristic intensity (I^3) and thickness (L^2) scaling[119] of the DFWM amplitude was confirmed within the measurement setup. As shown in Table 6, the setup parameters were varied over 3 intensities – via the incident laser pulse energy, with the pump signal measured on the calibrated reference detector in Fig. 34 – and 3 sample thicknesses. The DFWM signal amplitudes on the detector were compared to the expected changes, with the results normalized with respect to the DFWM signal amplitude of the 1 mm sample with a pump signal amplitude of 58.1 mV.

Due to the excellent agreement between the measured and expected values, the DFWM technique was applied to characterize the nonlinear refractive indices of CR39, PET, PMMA, and CA, with fused silica (FS) as the reference sample. The results, displayed in Table 7, are

Table 6: DFWM I^3 and L^2 scaling validation with fused silica

Thickness [mm]	0.25	1.0	1.0	1.0	3.0
Pump Signal [mV]	58.1	58.1	97.5	171.0	59.3
DFWM Signal [mV]	1.79	32.3	146	845	289
Normalized [a.u]	0.06	1	4.5	26.2	8.9
Expected [a.u]	0.06	1	4.7	25.5	9

Table 7: DFWM characterization of n_2 values at $\lambda = 1030\,\mathrm{nm}$

Material	FS	CR39	PET	PMMA	CA	Ar/Ne
Thickness [mm]	0.99	1.00	0.98	0.51	0.52	–
DFWM (Norm.) [a.u.]	1.00	5.18	21.9	0.91	1.23	–
Experimental $n_2\,[\cdot 10^{-7}\,\frac{\mathrm{cm}^2}{\mathrm{GW}}]$	(Ref)	6.24	13.1	5.13	5.85	–
Literature $n_2\,[\cdot 10^{-7}\,\frac{\mathrm{cm}^2}{\mathrm{GW}}]$	2.77[109]	–	–	4.18[122]*	5.00[122]*	10^{-3}[110,111]*

*Available literature n_2 values for $\lambda = 800\,\mathrm{nm}$.

consistent with previously estimated n_2 values found in literature for PMMA and CA. While references for CR39 and PET are not yet available in literature, the DFWM characterization reveals that CR39 and PET exhibit the highest potential for spectral broadening out of the samples, with n_2 magnitudes approximately 2 and 5 times larger than that of fused silica[109], and 1000 times larger than the gases employed for SPM in hollow-core fibers[112,113] (e.g., Argon or Neon at 1 bar[110,111]).

In addition to the high nonlinearity, a decisive criteria for the characterized samples is the absorption across the laser pulse spectrum. Despite the high damage threshold of the plastics, a high absorption would significantly limit the allowable thickness of the samples, particularly for the high fluences present within high peak power laser pulses. For this purpose, transmission measurements, seen in Fig. 35, of the uncoated samples were conducted at

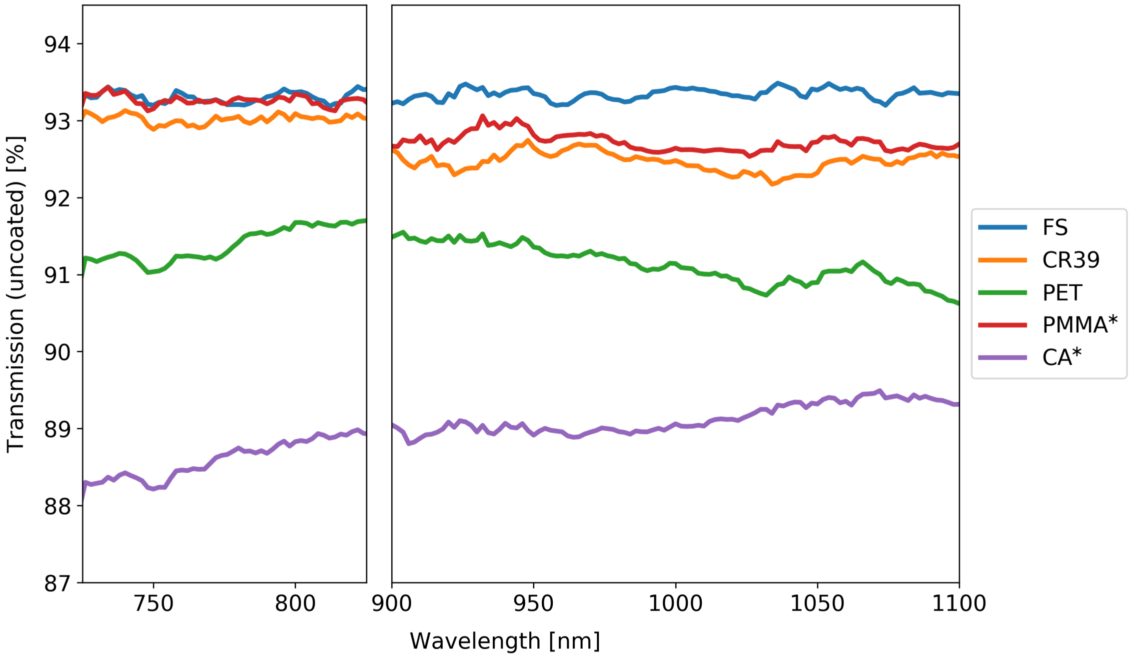

Figure 35: Transmission measurements of the 1 mm thick (*0.5 mm for PMMA and CA) nonlinear samples using the Shimadzu SolidSpec-3700 spectrophotometer. Data within a small spectral region, designated by the break in the plot, was unavailable due to an unavoidable detector switch during the measurement.

normal incidence with a UV-VIS-NIR spectrophotometer (Shimadzu SolidSpec-3700) over a spectral range exceeding 300 nm, including 800 nm and 1030 nm – relevant for Ti:Sapphire and Yb-based systems, respectively. Here, due to the lack of refractive index values across the measured spectrum in literature, the Fresnel reflections could not be adequately accounted for. Nevertheless, under the assumption of an average double-sided Fresnel reflection loss of 7.6% for CR39 and PMMA ($n \approx 1.49$), an anti-reflection (AR) coating of the two samples is expected to result in a near unity transmission. This is, however, not the case for PET, which exhibited the highest nonlinear refractive index between the samples, or CA. Here, CR39 offers the optimal combination of both high transmission and nonlinearity, and can be utilized to overcome the bandwidth limitations within the laser system by generating significant SPM in the near field for further pulse compression post-CPA.

3.2.2 Self-Phase Modulation in Thin Nonlinear Plastics

With the knowledge of the nonlinear refractive indices and transmission, a simulation of the spectral broadening of the ultrashort POLARIS laser pulse within the CR39 sample was constructed by solving the generalized nonlinear Schrödinger equation with the RK4IP method (Eq. 56, described in detail in section 2.4.3). The input pulse intensity was set to 1 TW/cm^2 to resemble the POLARIS pre-focus intensity. The results of the simulation, displayed in Fig. 36, predict a best-case increase in the spectral bandwidth from 12 nm to 44 nm after propagation through 1 mm of CR39. The 130 fs output pulse is compressible to a pulse duration of 41 fs. Here, the compact setup consisting of a 1 mm plastic sample and a chirped mirror pair for pulse compression effectively increases the peak power by a factor of 3.

To experimentally confirm the spectral broadening potential of the nonlinear plastics, the laser pulse generated from the 1st POLARIS CPA system, previously utilized for the DFWM-

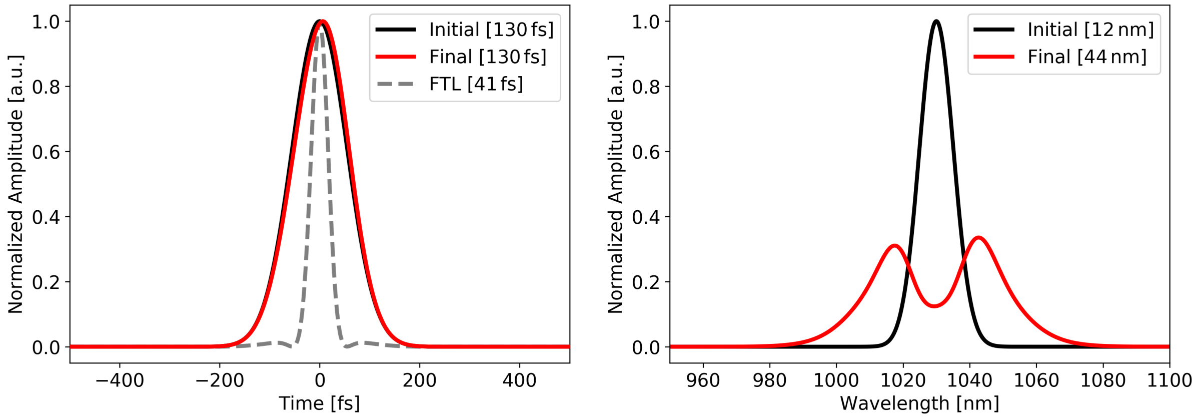

Figure 36: Simulation of the temporal (left) and spectral profiles (right) of the pre-focus 1 TW/cm^2 POLARIS laser pulse propagating through 1 mm of CR39. After a spectral broadening of approximately 3.7 times the initial bandwidth, an FTL pulse duration of 41 fs is achievable.

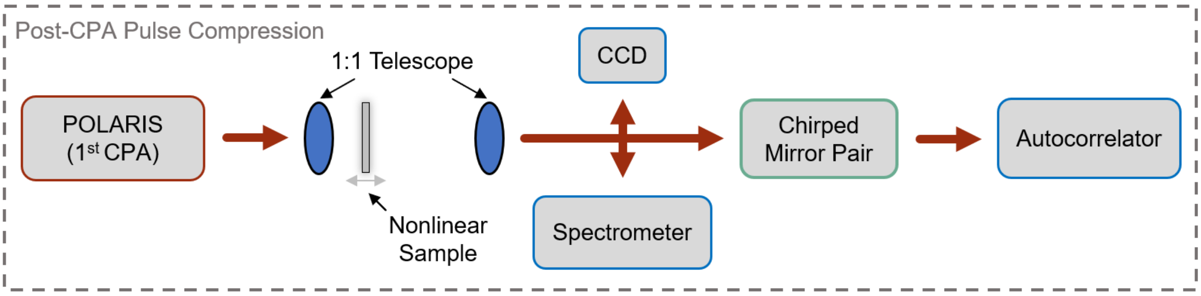

Figure 37: Schematic of the post-CPA pulse compression setup. A pulse from the 1st POLARIS CPA is directed into the thin nonlinear plastic, after which the spectrally broadened pulse is compressed by a pair of chirped mirrors. The diagnostics include spectral, spatial, and pulse duration measurements.

based n_2 characterization, was directed into a measurement setup, depicted in Fig. 37, consisting of a 1:1 Keplerian telescope (2 PCX lenses with 200 mm focal length) followed by a VIS-NIR spectrometer (Ocean Optics Flame-S). Without the plastic samples in the beam path, the intensity of the 75 µJ, 130 fs (FWHM) laser pulse was not sufficient to produce SPM in air, as seen by the initial spectrum in Fig. 38. The characterized nonlinear plastics were then individually inserted into the telescope at the location where the beam size (0.225 mm FWHM – approximately 15 mm from the focal plane) corresponded to the simulated intensity of 1 TW/cm^2, and the resulting spectra were measured. The significant spectral broadening displayed in Fig. 38 enables the application of the 1 mm thin nonlinear plastics to the post-CPA pulse compression method, with CR39 and PET exhibiting the highest spectral broadening

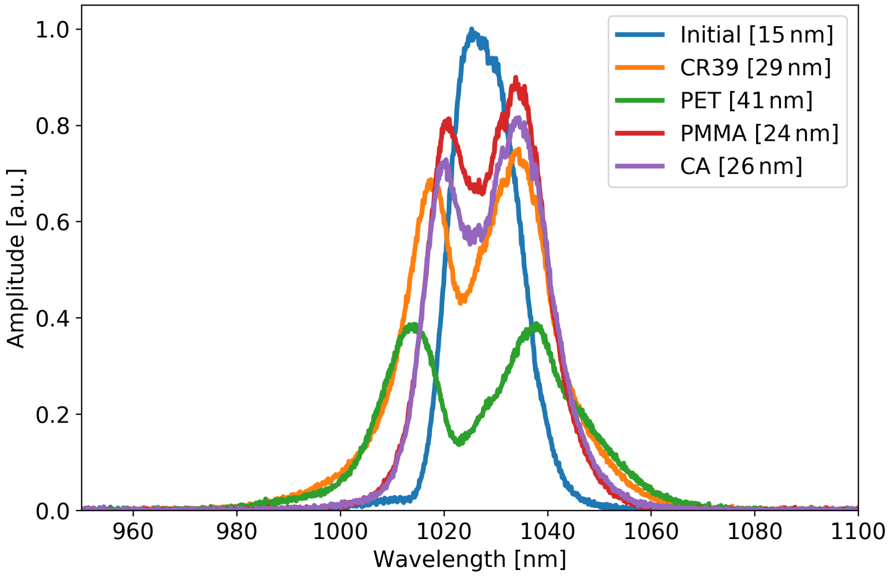

Figure 38: Self-phase modulation induced in 1 mm CR39, PET, PMMA, and CA, with the initial spectrum shown in blue. CR39 and PET exhibit the highest single-pass spectral broadening factors of 2 and 3, respectively, between the samples. Values given in the legend correspond to the FWHM spectral bandwidth.

factors – as expected from the DFWM-based n_2 characterization – of nearly 2 and 3, respectively. Additional measurements utilizing the maximum available energy of the laser pulse – 2 mJ with a beam size at the location of the nonlinear plastics of 1.1 mm FWHM (75 mm from the focal plane) – at the same laser pulse intensity of 1 TW/cm^2 did not produce an observable difference in the spectral profiles found in Fig. 38, further supporting the reproducibility of spectral broadening across various combinations of laser pulse energies and beam sizes. For mJ-level energies, however, neutral density filters were placed directly after the plastic sample to prevent ionizing the surrounding air at the laser focus.

Despite the large spectral broadening potential of PET, the lower transmission (evident in Fig. 35) limits the effectiveness of the nonlinear plastic for high energy or high repetition rate laser systems – particularly due to thermal effects, which can potentially deform the thin plastic. Here, CR39 offers a more promising combination of high spectral broadening and transmission. Nevertheless, the application of PET as a nonlinear material for spectral broadening within an amplifier can resolve, for example, gain narrowing issues (detailed in section 2.4.3) that are relevant for CPA systems involving ultrashort pulses. Using a separate Yb:FP15-based amplifier within the POLARIS laboratory, the potential spectral bandwidth broadening of the 1 mm PET sample inside the amplifier was tested. The amplifier was seeded with 5 nJ, 20 ps (stretched from 85 fs) pulses that were amplified to 2 mJ after 60 round trips. In Fig 39, the output spectrum and beam profile after intracavity SPM using the nonlinear plastic are displayed. The high nonlinear refractive index of PET is successfully able to compensate for gain narrowing through self-phase modulation, with an increase in the spectral bandwidth of 40% using the single 1 mm plastic sample. The energy loss due to the imperfect transmission of the nonlinear plastic can be recovered by increasing the pump density

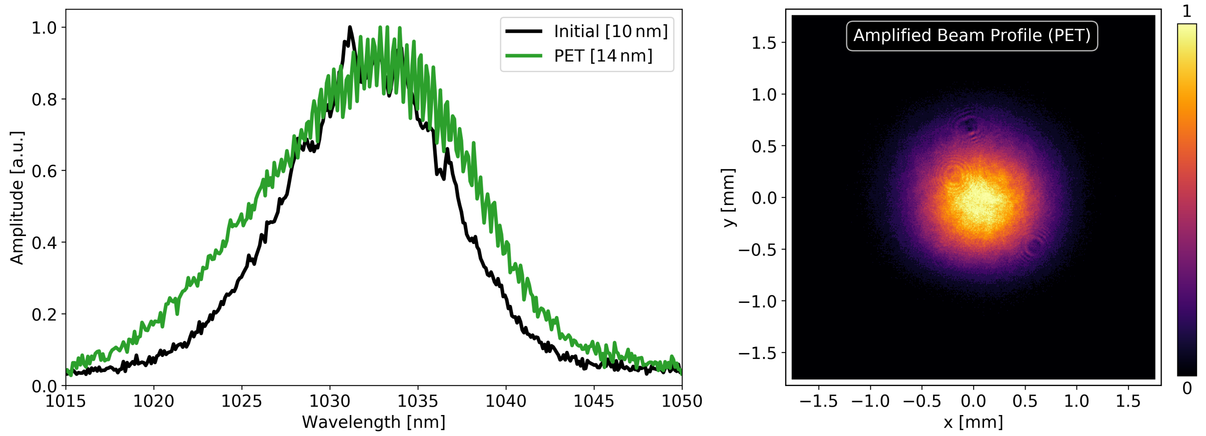

Figure 39: Spectral (left) and spatial (right) profiles of an amplified laser pulse with intracavity SPM using 1 mm thin PET. Spectral broadening of 40% was achieved for gain-narrowing compensation. The fringes present within the broadened spectrum are due to interference of the stretched pulse with Fresnel reflections from the uncoated PET, which can be corrected with an AR coating.

or the number of round trips within the amplifier. Furthermore, the amplified beam profile retains the desired Gaussian-like shape after the multiple (once per round trip) PET passes. However, the increase in the B-integral within the amplified and spectrally broadened laser pulse can deteriorate the rising edge[40] through the nonlinear spectral phase accumulation. For high temporal intensity contrast applications, the large spectral broadening generated within the PET-equipped amplifier can be accompanied by a post-amplifier acousto-optic modulator or by providing an intracavity effective negative nonlinear refractive index (e.g., via second harmonic generation[123]) to correct for the nonlinear accumulation within the spectral phase.

To determine the compressibility of the spectrally broadened pulses, the laser pulse from the 1st POLARIS CPA was directed through the previously described 1:1 telescope containing the 1 mm CR39 sample, which exhibits the highest potential out of the characterized plastics for use in the post-CPA pulse compression method. The nonlinear plastic was individually placed at two locations within the telescope to generate a broadening factor of 2 and 3 (approximately 30 nm and 45 nm FWHM, respectively). The output pulse was then compressed in a 6-bounce chirped mirror pair compressor (Layertec GTI mirrors with -250 fs^2/bounce) and the resulting pulse duration was measured with a second-order single-shot autocorrelator (TOPAG GmbH). As seen in Fig. 40, the initial 126 fs pulse was successfully compressed to 52 fs for the 30 nm variant and 40 fs for the 45 nm variant. The peak power enhancement of the ultrashort POLARIS pulse after the 1st CPA system – solely by this simple, compact setup – corresponds to approximately 2.4 and 3.2, respectively.

The proof-of-principle verification of the post-CPA pulse compression method can not only be replicated on the petawatt-class POLARIS laser system after the final CPA, as the near field intensity is above the required 1 TW/cm^2 for a doubling of the spectral bandwidth, but can

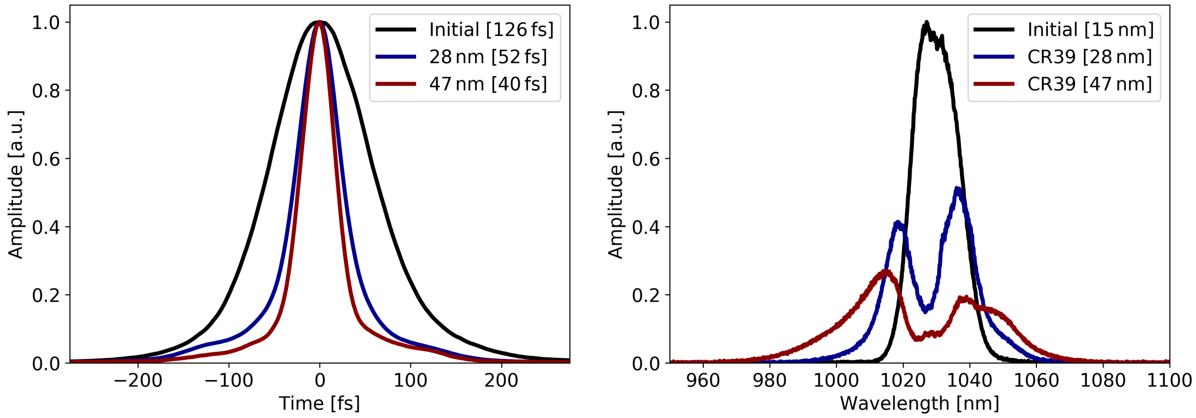

Figure 40: Temporal (left) and spectral (right) profiles of the POLARIS laser pulse from the 1st CPA. The post-CPA pulse compression method using 1 mm CR39 and a 6-bounce chirped mirror pair increased the laser pulse intensity by factors of 2.4 and 3.2 for two broadening configurations.

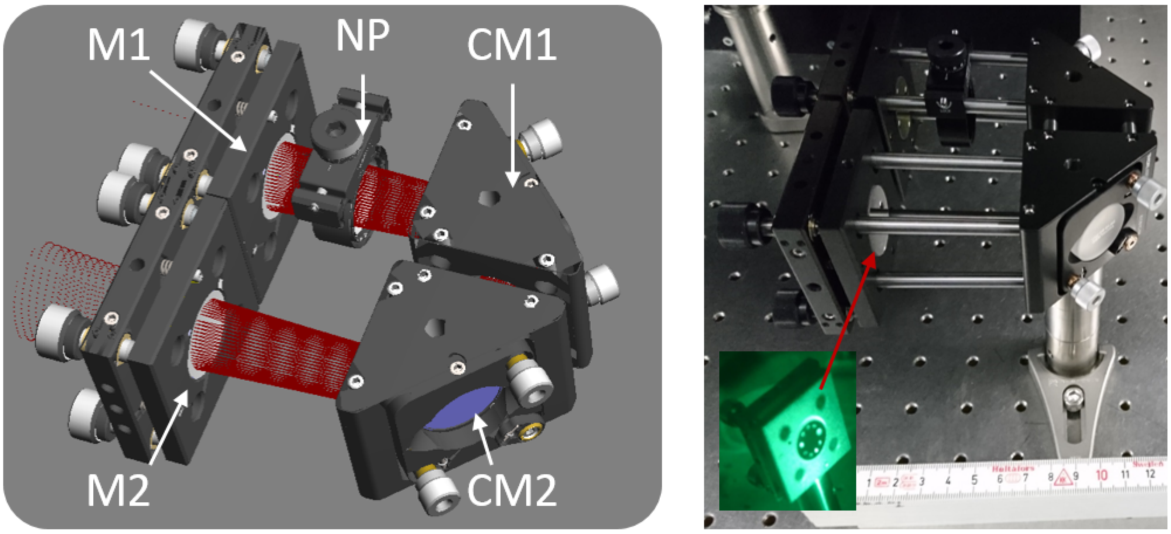

Figure 41: Possible application of the nonlinear plastic (NP), in which a laser pulse enters a multi-pass Herriott cell (curved mirrors M1 and M2) containing chirped mirrors (CM1 and CM2). As seen in the FRED model (left) and preliminary testing (right), the input pulse exits the device after a set number of passes determined by the distance between M1 and M2, with spectral broadening and compression in each pass.

also be applied in a compact multi-pass configuration to transform a 130 fs laser pulse into a few-cycle probe for laser-plasma interactions. A potential example of an additional application is given in Fig. 41 (left: FRED model, right: prototype), in which the thin nonlinear plastic can be built into a folded Herriott cell with chirped mirrors already installed for multi-pass spectral broadening and compression. The input pulse enters and exits through a hole in M1, with the number of passes – optimized for a combination of spectral broadening and pulse compression – adjustable via the spacing between M1 and M2.

Optimizing the temporal profile of a high peak power laser pulse towards shorter pulse durations by the implementation of thin nonlinear plastics is a compact and efficient alternative to increase the laser pulse intensity without the costly process involved in an energy and aperture scaling of the laser system. Further investigations to improve and characterize the results of this promising method under full operating conditions at the petawatt-class POLARIS laser system are currently underway.

3.3 Contrast: Plasma Mirror

At the POLARIS laser system, high peak power pulses are delivered on-target with focused intensities in excess of $10^{20}\,\mathrm{W/cm^2}$. Picoseconds or even nanoseconds before the arrival of the 100 fs main pulse, as seen in Fig. 42, the ASE pedestal or pre-pulses (described in section 2.4.4) present within the laser chain with intensities 10^{-7} times lower than that of the main laser pulse can generate a pre-plasma on the target surface, significantly deforming the target (e.g., nm-thin DLC[124] or µm-thick Al[125] foils utilized for proton acceleration) and disturbing the desired laser-plasma interaction. Therefore, an increase in the intensity of petawatt-class laser systems must be accompanied by a subsequent optimization of the laser pulse rising edge and temporal intensity contrast (TIC) – the ratio between the laser pulse peak intensity and the intensity of ASE and pre-pulses.

Degradation of the temporal intensity contrast of a high peak power laser system can occur in part due to the imperfect contrast ratio of pulse pickers within the laser chain or regenerative amplifiers, spontaneous emission that is produced and amplified within each amplifier stage[63], post-pulses formed from reflections off of plane-parallel plates that produce pre-pulses via nonlinear mixing with the main pulse during recompression[64], high frequency spectral phase modulations[65] within the CPA system, or even scattered light from gratings[66]. To compensate for this reduction in the TIC, various techniques can be implemented within the laser chain, including an optical parametric amplifier[127,128] (OPA), saturable absorber[129], multiple Pockels cells, and cross-polarized wave generation[69] (XPW) within a double CPA chain[60]. For petawatt-class lasers, these methods alone may not be sufficient to reduce the ASE and pre-pulse intensity below the ionization threshold of the target. Here, a "plasma mirror" setup[130,131] can be installed in vacuum between the compressor and the target to provide over a 100-fold additional improvement in the TIC.

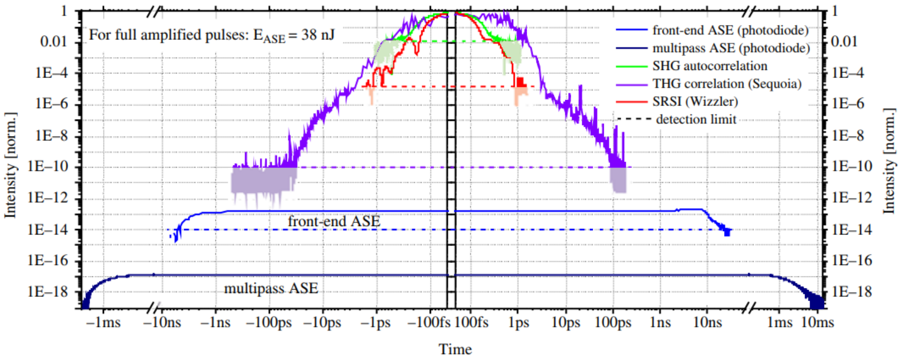

Figure 42: Temporal intensity contrast (TIC) of the POLARIS[126] laser system before the plasma mirror installation. The front-end and multi-pass ASE were characterized with calibrated photodiode measurements, while the laser pulse intensity within the ±100 ps temporal window around the main pulse was measured using SHG and THG correlation along with self-referenced spectral interferometry.

3.3.1 The POLARIS Plasma Mirror

A plasma mirror (PM) is a passive ultrashort optical switch that is capable of suppressing the energy of the ASE and pre-pulses on target by several orders of magnitude[132] with only a marginal reduction[133] in the energy of the main laser pulse. Here, the laser pulse is sent into an imaging setup consisting of two off-axis parabolas (OAP) with an anti-reflective (AR) coated substrate near the focal plane. The PM position is set such that the intensity of the pre-pulses and ASE pedestal before the main pulse are sufficiently low to avoid ionizing the untriggered PM surface, and are therefore simply transmitted through the AR-coated substrate. When the fluence within the rising edge of the main pulse – already several orders of magnitude larger than the pre-pulses or ASE pedestal – is high enough to ionize the surface of the AR-coated substrate of the PM, a plasma is formed on the surface and the PM is triggered. The following high intensity main laser pulse reflects off of the critical surface of the plasma, thereby separating it from the pre-pulses and ASE pedestal, and is then collimated by the second OAP in the imaging setup before being sent to the experimental target. The expected[134] temporal intensity contrast improvement ΔTIC induced by the plasma mirror is dependent on the initial (untriggered) surface reflectivity R_i and the plasma reflectivity R_p:

$$\Delta TIC = \frac{R_\mathrm{p}}{R_\mathrm{i}}. \tag{63}$$

In the POLARIS laser system, the imaging optics that comprise the folded 1:1 telescope within the plasma mirror setup, depicted in Fig. 43, are matching F/6 off-axis parabolas with 90 cm reflected focal length at a 6° angle of incidence. A UV fused silica (Corning 7980 0F) substrate with a $\leq 0.1\%$ AR coating, acting as the plasma mirror (Fig. 43, right), was mounted in a 5-axis motorized stage (Fig. 43, center) and set at an optimized location with respect to the laser focus. The 50 mm × 20 mm plasma mirror substrate is large enough to accommodate

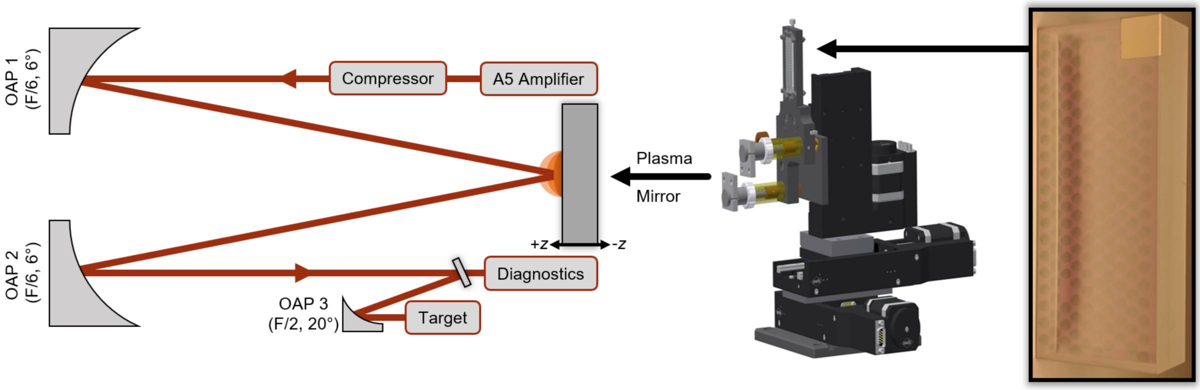

Figure 43: Plasma mirror (PM) setup at the POLARIS laser system. The PM (right) was mounted in a 5-axis motorized stage (center) and installed within a folded 1:1 imaging setup (left) consisting of two matching F/6 off-axis parabolas.

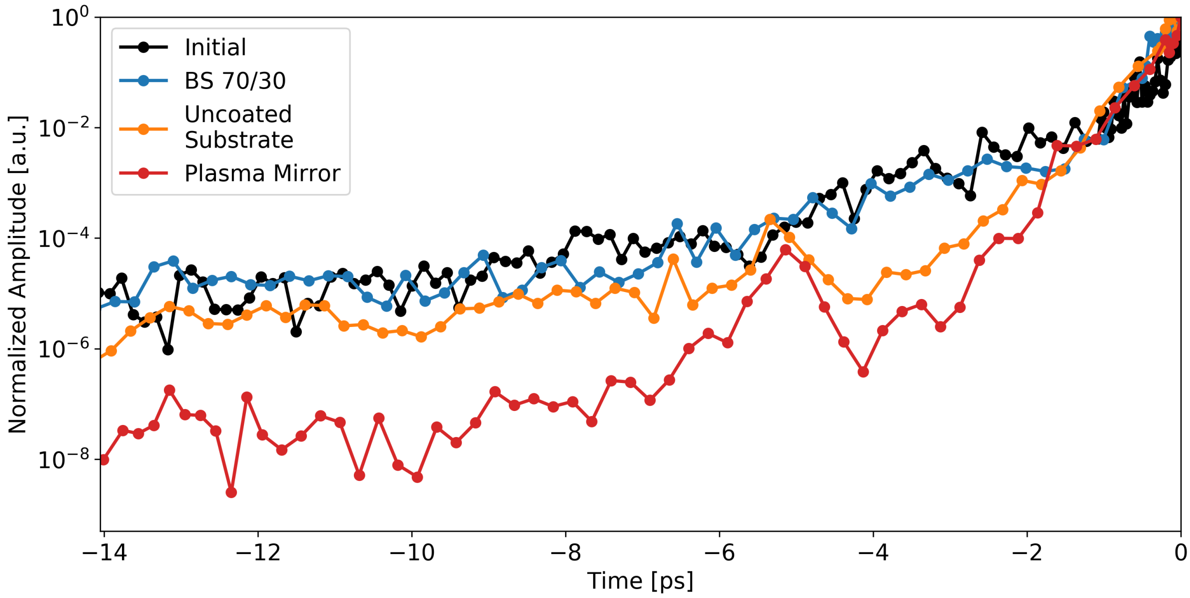

Figure 44: TIC improvement of the POLARIS laser with various (black: initial, blue: $R_\mathrm{i} = 0.7$; orange: $R_\mathrm{i} = 0.04$; red: $R_\mathrm{i} \leq 0.001$) untriggered surface reflectivities of the plasma mirror substrate placed 5 mm before the focus.

approximately 200 shots, which allows for nearly 3 hours of continuous TIC improvement at the POLARIS repetition rate of 0.02 Hz before substrate replacement is required.

To determine the operating parameters for the plasma mirror, a high dynamic temporal characterization of the POLARIS laser pulse with and without the PM was conducted using a third-order cross-correlator (Sequoia). As seen in Fig. 47 and in Eq. 63, the reflectivity of the untriggered PM surface is a dominant variable in determining the effectiveness of the plasma mirror. To confirm this, three different samples of varying surface reflectivity were utilized as the plasma mirror and placed 5 mm after the laser focus. The temporal intensity contrast utilizing a thin plate beamsplitter (BS 70/30, $R_\mathrm{i} =$ 0.7, blue) as the PM is nearly indistinguishable from the initial TIC profile without the PM. A decrease in the surface reflectivity using an uncoated fused silica substrate ($R_\mathrm{i} =$ 0.04, orange) improved the TIC by nearly an order of magnitude. Finally, by employing the AR-coated substrate ($R_\mathrm{i} \leq 0.001$, red) as the PM, a 1000-fold suppression of the ASE pedestal at 14 ps before the main pulse was achieved.

In addition to the surface reflectivity, the position of the plasma mirror along the propagation axis (z-axis) can be optimized to improve the ΔTIC. Fig. 45 displays the temporal characterization of the POLARIS laser with the AR-coated substrate placed at various positions after the laser focus, which corresponds to the position z = 0 mm. As the plasma mirror is moved away from the focus (larger negative values), the plasma formation on the PM surface occurs temporally closer to the peak of the pulse – evident by the sharp increase in the amplitude of the temporal profiles. For z = -3 mm (blue), the improvement in the TIC

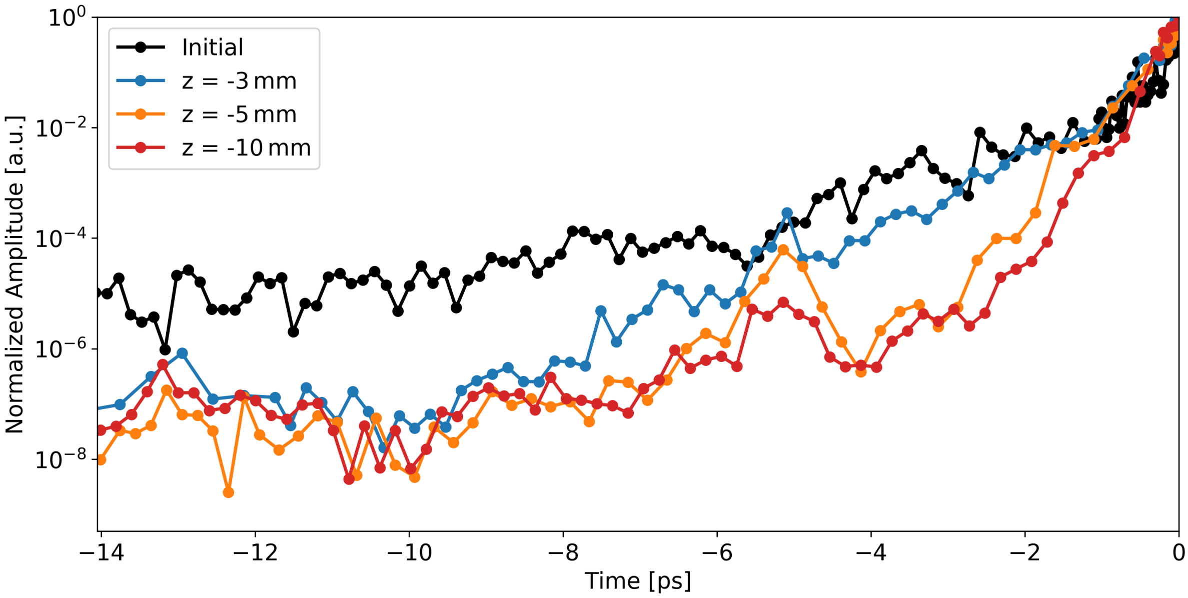

Figure 45: TIC improvement of the POLARIS laser with increasing distance (black: initial, blue: z = -3 mm; orange: z = -5 mm; red: z = -10 mm) of the plasma mirror from the focus.

is reduced starting at the trigger time of -10 ps. For z = -5 mm (orange) and -10 mm (red), however, the plasma mirror is triggered within the ps-rising edge of the laser pulse, with an additional 10-fold enhancement of the TIC improvement factor for the latter case. While the plasma mirror can significantly improve the temporal intensity contrast of the laser system, it can also lead to a slight deterioration of the spatial quality and energy of the main laser pulse. The interaction of the laser pulse with the expanded plasma and critical surface of the plasma mirror introduces high frequency distortions in the near field profile of the laser pulse, which results in a slight enlargement of the focal area of nearly 12%, as seen in Fig. 46. Despite the potential improvement in the reflected spatial quality by placing the plasma mirror closer to the laser focus – as the plasma mirror acts as a low-pass filter[135] in the Fourier plane – the results in Fig. 45 confirm that the PM performance regarding the ΔTIC increases with larger distances from the focus.

The change in the plasma reflectivity R_p, measured with calibrated calorimeters both before and after the plasma mirror, with respect to the peak intensity on the PM surface is shown in Fig. 47. The averaged R_p values over 5 shots are given in black, with the maximum and minimum values in grey. Although the peak plasma reflectivity R_p of 0.78 occurs near z = -6 mm, the optimum performance of the plasma mirror regarding the temporal intensity contrast is near the z = -10 mm position – corresponding to a peak intensity on the PM surface of 10^{15} W/cm^2 and R_p = 0.75 – as the trigger time occurs within the picosecond rising edge and near the peak of the laser pulse.

The selection of this operating point for the plasma mirror can be further justified by experimental results with laser-based ion acceleration in the radiation pressure acceleration

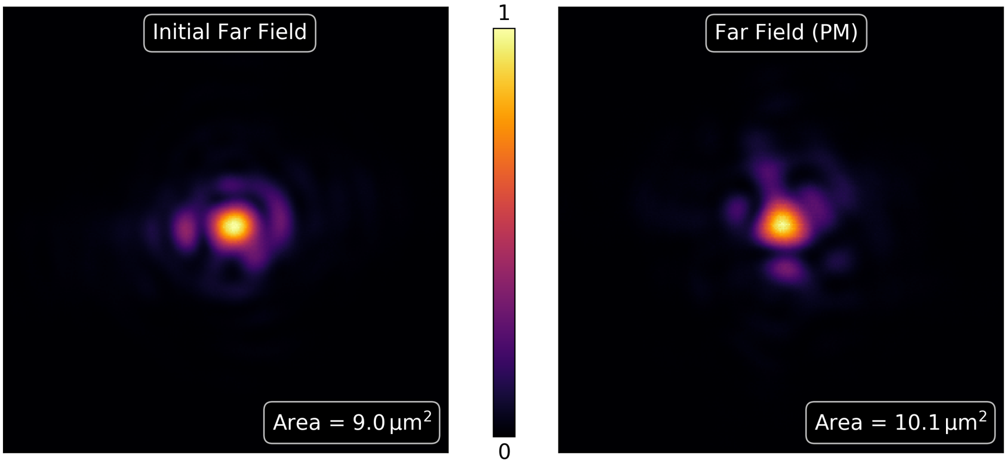

Figure 46: Influence of the plasma mirror on the far field profile (initial: left, PM: right) of the full POLARIS laser pulse, measured on a PM-diagnostic setup outside the target chamber. The area is defined by the intensity region $I > I_{\max}/2$.

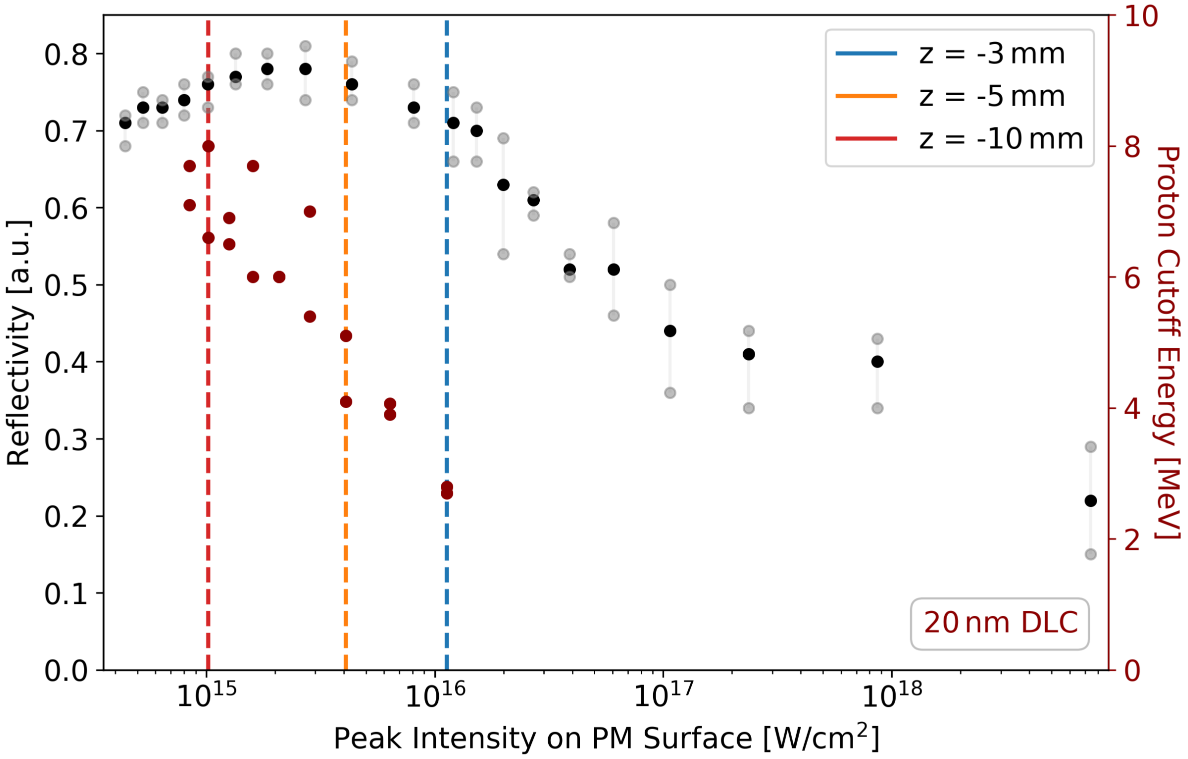

Figure 47: Variation in the plasma reflectivity with respect to the plasma mirror position. The optimal combination of high reflectivity (0.75) and ΔTIC at z $=$ -10 mm from focus directly resulted in a tripling of the proton cutoff energies in a laser-based proton acceleration experimental campaign employing 20 nm thin DLC foils.

(RPA[136,137]) regime, in which the maximum accelerated proton energy increases[138] with an improvement in the rising slope of the laser pulse, as the pre-plasma formation on the target surface before the arrival of the main pulse is suppressed. As seen in Fig. 47, accelerated proton cutoff energies from the interaction between a 20 nm thin diamond-like-carbon (DLC) target and the focused POLARIS laser pulse using the optimized plasma mirror position of z = -10 mm from focus were nearly doubled and tripled in comparison to the z = -5 mm and z = -3 mm cases, respectively.

The live performance of the optimized plasma mirror is monitored with an automated diagnostic setup located outside of the target chamber. By imaging leakage light from an HR-coated mirror placed between the plasma mirror setup depicted in Fig. 43 and the final focusing parabola before the target, the near field, far field, nanosecond contrast (via a calibrated photodiode), and reflectivity can be characterized with each shot. A mirror attached to a motorized stage installed within the target chamber allows the laser pulse to bypass the plasma mirror setup for experiments utilizing thick targets[79] for alternative laser-based charged particle acceleration schemes (e.g., TNSA[139]) or for reference measurements. Furthermore, the plasma mirror setup can be easily realigned after substrate replacement as well as during the experimental campaign by monitoring the displacement of a reflected CW laser off of the silver-coated edge on the plasma mirror (Fig. 43, right).

The plasma mirror setup within the POLARIS laser system provides a temporal intensity contrast improvement – with the TIC characterization for the optimized PM configuration given in Fig. 48 – of a factor of 1250 at -14 ps and 500 at the trigger time of -4 ps before the peak of the main pulse, while maintaining a high reflectivity of 75% with a minimal (1.1 μm^2)

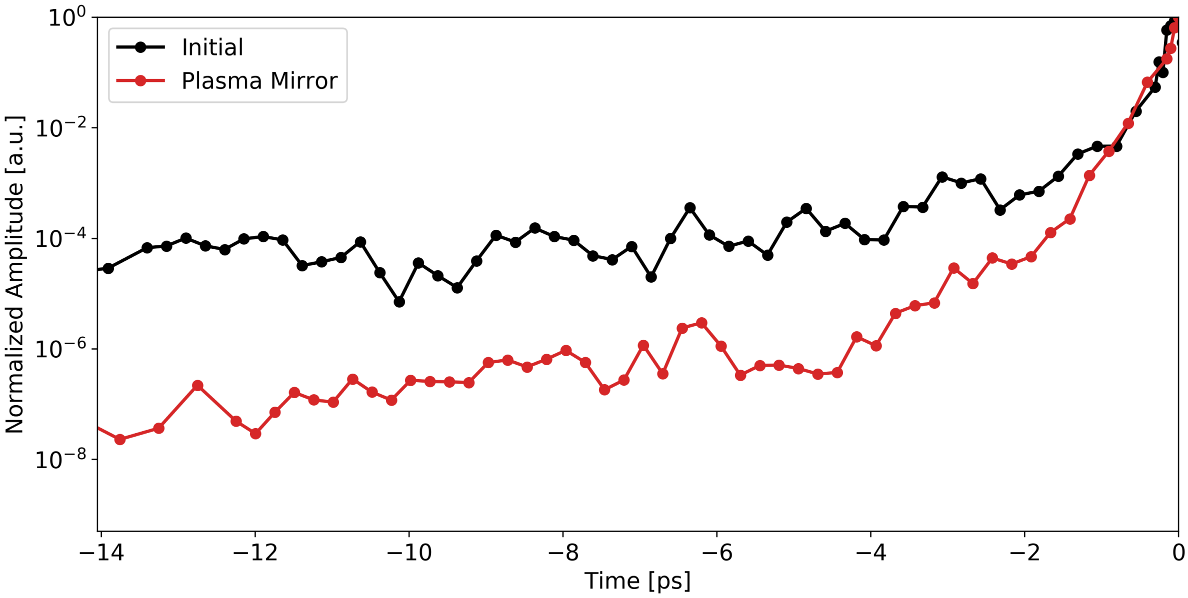

Figure 48: Optimized TIC improvement using a plasma mirror of 1250 at -14 ps and 500 at -4 ps from the main POLARIS laser pulse.

enlargement of the focal spot area. The temporal characterization of the POLARIS laser with a third-order cross-correlator (Sequoia) was utilized to determine the optimum untriggered surface reflectivity and plasma mirror position with regards to the temporal intensity contrast. The plasma reflectivity and far field profiles were characterized using a calibrated diagnostic setup. The optimum location of the plasma mirror corresponded to a peak intensity on the PM surface of 10^{15} W/cm^2 at $z = -10$ mm from the focus, which resulted in an improvement in the laser-accelerated proton cutoff energies from a 20 nm DLC foil by a factor of 3. The installation and optimization of a plasma mirror setup within a high peak power laser system such as POLARIS demonstrated an effective suppression of ASE and pre-pulses and an enhancement in the picosecond rising edge by several orders of magnitude, enabling direct access to potentially significant improvements in the experimental yields[140] of laser-plasma interactions.

4 NOPA-Based Ultrashort Optical Probe Pulse Generation

Employing a petawatt-class laser pulse as the pump laser for laser-plasma interactions allows access to multiple relativistic phenomena, such as laser-ion acceleration[141] and laser wakefield acceleration of electrons[142,143]. However, due to the complex nature of these interactions, an optimization of the laser and plasma parameters towards higher electron and proton energies is challenging. Acquiring a comprehensive understanding of relativistic laser-plasma processes requires advanced methods to resolve the spatially (µm) and temporally (fs) confined interaction regions. Here, optical probing[144–146] using an ultrashort laser pulse is a promising technique to extract critical information from the laser-plasma interaction via a direct imaging with a high spatio-temporal resolution.

An ultrashort optical probe can be utilized in conjunction with shadowgraphy or interferometric methods to image[147,148] the laser-generated plasma, determine the local plasma density profiles[112] in various experimental configurations, and investigate the existence of simulated relativistic processes such as relativistic induced transparency[149]. Examples of the applications of an ultrashort optical probe for a laser-plasma interaction with a high peak power laser pulse are given in Fig. 49, in which a plasma wave (top[112]) generated in a hydrogen gas and plasma expansion (bottom[150]) in a water droplet target are transversely probed and shadowgrams of the interaction regions are recorded. To reliably apply the high resolution optical probing method for laser-plasma interactions, multiple design constraints regarding the ultrashort laser pulse must be met.

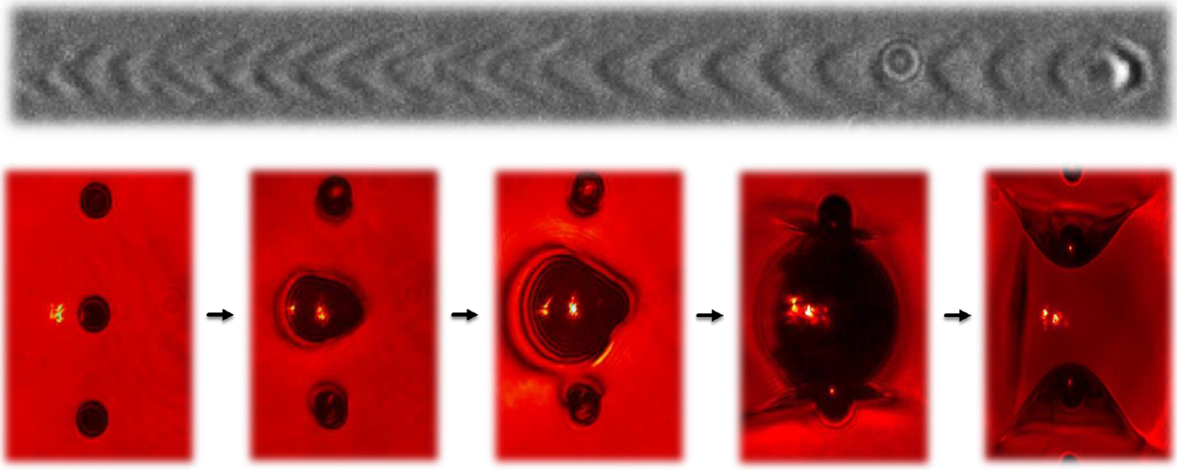

Figure 49: Shadowgrams of a plasma wave (top[112]) in a hydrogen gas target and of an expanding plasma (bottom[150]) in a water droplet target at various times (delay with respect to main pulse reaching target; from left to right: +100 fs, +64 ps, +150 ps, +440 ps, +1.275 ns).

4.1 Design Parameters of an Ultrashort Optical Probe

The design parameters of an optical probe are not only dependent on the spatial and temporal limitations of the interaction region, but also on the main pump laser (i.e., the POLARIS laser) for the laser-plasma interaction as well. The technique used to generate the ultrashort laser pulse was selected based on the following criteria:

Diameter $2w > 1\,\mathrm{mm}$: The beam diameter ($2w$ at $1/e^2$) must be large enough to fully capture the interaction region encompassing the laser focus. Additionally, the spatial profile should be free from high spatial frequencies and remain intact after meter-long propagation distances.

Pulse Duration $\tau_{\mathrm{FTL}} \leq 13\,\mathrm{fs}$: The temporal resolution of the probe pulse is given by its pulse duration τ, which should be at least an order of magnitude shorter than that of the POLARIS laser (130 fs) to resolve[112] laser-plasma phenomena within the time frame of the interaction. Furthermore, the spectral phase of the broadband probe pulse must allow for pulse compression (i.e., low magnitude higher-order dispersion) down to or near the Fourier transform limit τ_{FTL} using simple dispersive optical components, such as chirped mirrors.

Wavelength $\lambda_{\mathrm{L}} = 800\,\mathrm{nm}$: The full spectrum should not overlap with the fundamental frequency (1030 nm) and harmonics (second harmonic: 515 nm) of the POLARIS laser, due to strong plasma emission and reflection within these spectral regions[151,152] that may obscure the desired measurements using the optical probe.

Bandwidth $\Delta\lambda \geq 150\,\mathrm{nm}$: The spectral bandwidth $\Delta\lambda$ should be large enough to support ultrashort (fs) pulse durations and enable advanced spectrally resolved probing options such as chirped pulse probing[153].

Intensity $I_{\mathrm{L}} \ll 10^{12}\ \mathrm{W/cm^2}$: To avoid target deformation or undesired influences on the plasma by the probe pulse, the intensity I_{L} of the optical probe must be below the ionization threshold of the target material.

Energy $E \geq 10\,\mu\mathrm{J}$: To ensure proper illumination of the interaction region without ionizing the target due to the high intensity of the optical probe, the probe pulse energy should be within the µJ regime.

Stability $\sigma_{RMS} \leq 1\%$: For experimental reliability, the spectral bandwidth fluctuation of the probe pulse should not exceed 1% RMS. Furthermore, to minimize the temporal jitter between the POLARIS laser and the optical probe, the probing system should be seeded by the POLARIS oscillator, synchronized with the POLARIS laser pulse, and the compact, portable setup should be placed near the target chamber.

4.2 A Yb^{3+}-Based, mJ-Class Ultrashort Pump Laser for NOPAs

To fulfill the necessary criteria, the ultrashort optical probe was designed, simulated, constructed, and optimized as a POLARIS oscillator-seeded noncollinear optical parametric amplifier (NOPA) system. As described in section 2.3, noncollinear optical parametric amplification is a powerful and established method[34] for generating high peak and average power laser pulses. Through a nonlinear phase-matching mechanism[37], low energy laser pulses can be amplified with a single-pass gain[32] on the order of 10^4. The pump intensity ($\sim 100\,\mathrm{GW/cm^2}$) required to enable the large ultrabroadband gain within the nonlinear crystals can be achieved by a single mJ-class Yb:FP15 regenerative amplifier in a compact CPA setup, in which a nJ-level POLARIS seed pulse is amplified with a total gain of 10^6. Multiple techniques[31,67,154,155] utilized in the high performance Yb^{3+}-based laser systems at POLARIS were employed to develop the standalone CPA system to pump the NOPA.

4.2.1 Seed Pulse Stretching, Selection, and Control

The pump laser for the NOPA begins at the POLARIS[14] Ti:Sapphire oscillator (MIRA 900, Coherent), which utilizes passive Kerr-lens mode-locking to deliver 85 fs laser pulses at a central wavelength of 1030 nm and a pulse energy of 5 nJ. As depicted in Fig. 50, the ultrashort pulse enters the picosecond-CPA chain and is stretched from 85 fs to 20 ps in an Offner-type stretcher[67,70]. The 40 cm × 20 cm footprint ps-stretcher consists of a single gold grating

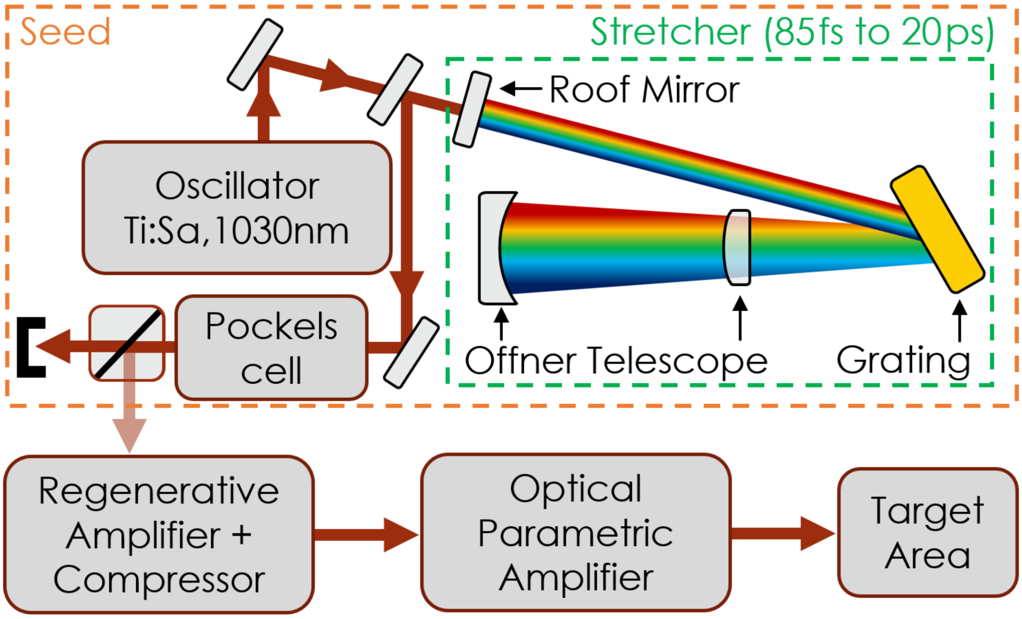

Figure 50: Setup schematic for the ultrashort seed generation and entrance to the CPA system that pumps the NOPA. The 85 fs seed is generated in a 400 mW Ti:Sa oscillator and stretched to 20 ps in an Offner stretcher. A single pulse is picked out of the 75 MHz pulse train and sent for amplification in a Yb-based regenerative amplifier.

(1200 lines/mm, 42° AOI), an Offner telescope with f = 300 mm and f = -150 mm spherical mirrors, and a roof mirror that vertically offsets and redirects the laser pulse back through the setup in a double-pass configuration.

After exiting the stretcher, a single pulse is picked out of the 75 MHz pulse train with a Pockels cell and polarizer combination at a repetition rate of 1 Hz and sent to the regenerative amplifier. To minimize the effect of seed beam pointing fluctuations on the amplifier shot-to-shot energy stability, due in part to the large propagation distance (4 laboratories and 2 stories) to the regenerative amplifier in the target area, a motorized and automated beam-steering system was developed and installed within the beamline. The seed spectrum, pulse train selection, and a screenshot of a portion of the beam-steering interface are shown in Fig. 51.

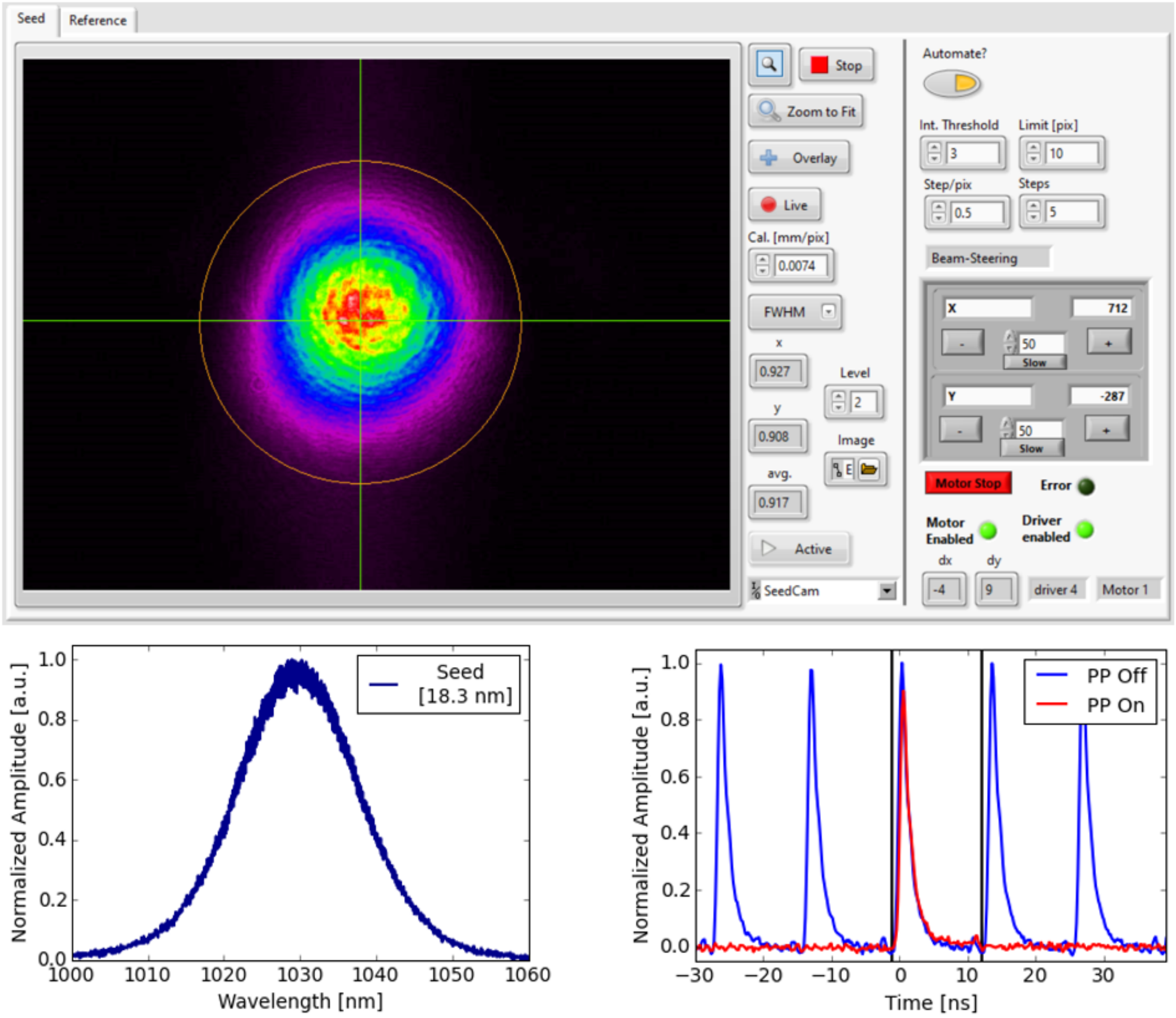
Int. Threshold 3
Limit [pix] 10
Step/pix 0.5
Steps 5
Cal. [mm/pix] 0.0074
FWHM
x 0.927
y 0.908
avg. 0.917
Level 2
X 712
50 Slow
Y -287
50 Slow
dx -4
dy 9
driver 4
Motor 1
SeedCam

Figure 51: Diagnostics and control of the seed pulse: Screenshot (top) of a portion of the beam-steering interface. Seed spectrum (bottom left) with FWHM bandwidth in the legend. Photodiode measurement (bottom right) showing the seed selection from the 75 MHz pulse train with the pulse picker ("PP").

4.2.2 Yb:FP15-Based Regenerative Amplifier

The stretched seed pulse enters the regenerative amplifier setup depicted in Fig. 52 with an input energy of 2 nJ and a pulse duration of 20 ps. The beam size was adjusted with a telescope before the input coupling to match the mode of the cavity within the amplifier. The p-polarized seed pulse is transmitted through a thin film polarizer (TFP: 65° AOI with p-polarized transmission and s-polarized reflection) and passes through a half-wave plate (HWP), through which the polarization is rotated to the s-state before it enters the Pockels cell. For the first round trip within the cavity, the Pockels cell remains inactive, such that the resulting polarization of the seed pulse is relatively unchanged – here, the slight depolarization due to the birefringence of the crystal within the Pockels cell contributes to the resonator losses via the TFPs within the setup.

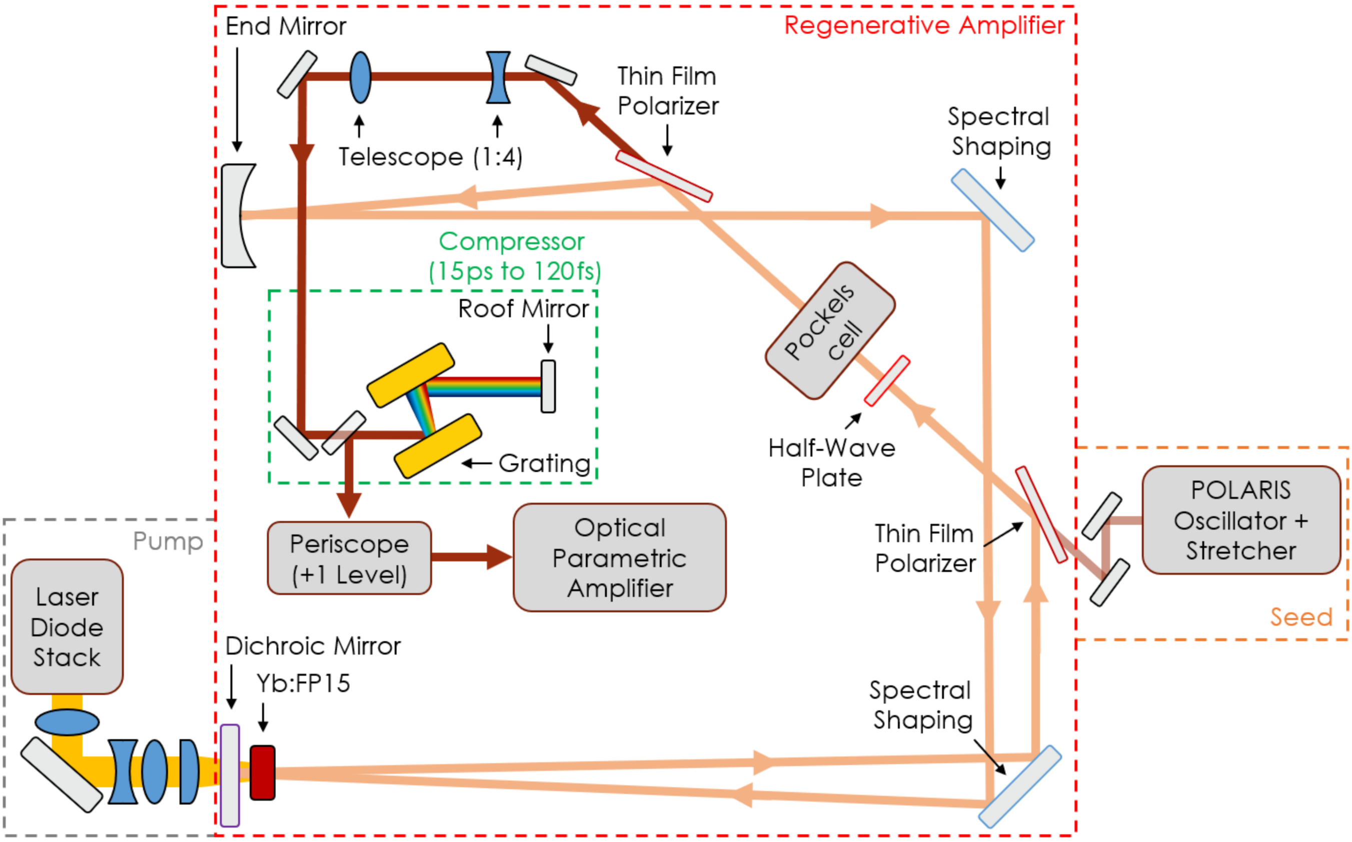

Figure 52: The seed pulse from the POLARIS oscillator enters a CPA system, where it is amplified with a total gain of 10^6 to pump the NOPA. The regenerative amplifier, shown along with the compressor in this schematic, consists of an optical cavity with a diode-pumped Yb:FP15 as the active material, spectral shaping filters to homogenize the spectral gain profile, and a Pockels cell to control the pulse input and output coupling. The amplified pulse is then compressed to 120 fs and sent upwards to the NOPA stage using a periscope.

The seed pulse exits the Pockels cell and reflects off the TFP and the end mirror (radius of curvature "ROC" = 5 m), where it is then redirected onto a pair of reflective spectral shaping filters[155] that compensate for spectral gain narrowing in the amplifier by introducing loss for the central wavelength region to flatten the spectral gain profile. After spectral shaping, the seed pulse is amplified in a pumped and water-cooled broadband Yb:FP-glass (FP15[29]). The active material was optimized to maximize the single-pass gain by choosing the proper length (1.3 cm) to balance the pump absorption ($\geq$ 90%) and seed reabsorption ($\leq$ 8%).

The pump system consists of a 3.2 kW laser diode stack operating at 940 nm that delivers 8 J pump energy within 2.7 ms pulses to the Yb:FP15. The spatial profile emitted from the 8 laser diode bars is formed into a square-shaped beam profile using a compact (folded, 30 cm total length) imaging setup with a zoom lens and a final cylindrical lens. The pump density within the active material can be easily adjusted by changing the beam size through a variation in the spacing between the zoom lens optics within the caged setup. The spatially optimized pump pulse passes through a dichroic mirror, which transmits the 940 nm pump and reflects the 1030 nm seed, and into the active material. Together, the dichroic and curved (ROC = 5 m) mirrors form the end mirrors for the cavity.

As the seed pulse is directed from the spectral shaping filters towards the dichroic mirror, it undergoes a double-pass through the pumped active material before reflecting off the surface of one of the spectral shaping filters and back onto the initial TFP to complete the round trip. In the second round trip, the Pockels cell is activated, effectively canceling the polarization rotation of the HWP and allowing the seed pulse to remain within the cavity in the s-polarized state. After 60 round trips (round trip time τ_{rt} = 11 ns) with a single-pass gain of nearly 1.3 and a total gain of 10^6, the Pockels cell is deactivated and the amplified pulse with nearly 3 mJ energy is coupled out of the regenerative amplifier in the p-polarized state.

Before the amplified pulse enters the compressor setup, the beam diameter is magnified by a factor of 4 using a Galilean telescope to avoid damage to the gratings. The compressor, which consists of two identical gold gratings (1200 lines/mm) separated by 8.5 cm and a roof mirror for a double pass through the grating pair, compensates for the spectral phase contributions from the ps-stretcher and the amplifier (e.g., active material, Pockels cell, and dielectric coatings on the cavity optics). Here, the -5.68·10^5 fs^2 GDD and 1.50·10^6 fs^3 TOD produced by the compressor setup reduces the chirped pulse duration from 15 ps – clipped from the initial 20 ps via spectral gain narrowing within the amplifier – to 120 fs. The Gaussian-like spatial profile (1.3 mm $1/e^2$ diameter before the telescope) of the amplified pulse is given in Fig. 53, along with the amplified spectrum (15 nm FWHM bandwidth) and compressed pulse duration (measured with a single-shot second order autocorrelator, TOPAG GmbH). The complete CPA chain produces high intensity (150 GW/cm^2 at the compressor output) pulses at 1 Hz of 2 mJ energy within 120 fs to pump the noncollinear optical parametric amplifier.

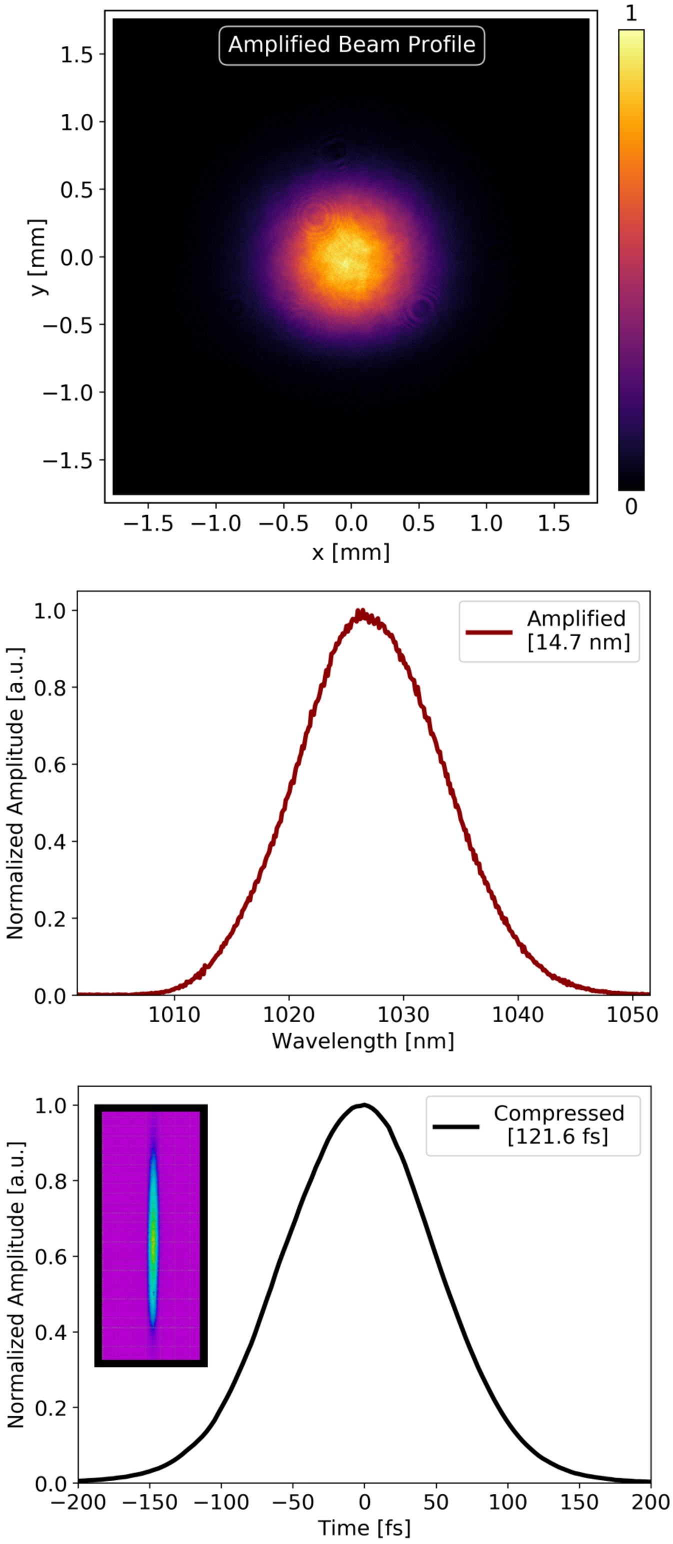

Figure 53: Amplified spatial beam profile (top, 1.3 mm $1/e^2$ diameter) of the Yb:FP15-based CPA system with spectral profile (center) and compressed pulse duration (bottom). An image of the measured signal generated in the single-shot second-order autocorrelator is displayed in the top left corner of the pulse duration measurement. Values in the legends describe the FWHM spectral bandwidth (center) and pulse duration (bottom).

4.3 Noncollinear Optical Parametric Amplifier Optimization

Using the fundamentals described in section 2.3, a noncollinear optical parametric amplifier was simulated and constructed at the POLARIS laser system. To pump the NOPA, the ultrashort POLARIS seed pulse, amplified to the millijoule-level by the Yb-based regenerative amplifier described in section 4.2.2, was separated into two unequal amplitude components to generate white light supercontinuum (WLC) and second harmonic (SH) pulses. The two pulses were then spatio-temporally overlapped within a nonlinear crystal to activate the optical parametric amplification process, which was optimized according to the phase-matching angle, pump/signal cross angle, crystal length, and temporal delay between the WLC and SH pulses to meet the performance criteria (section 4.1) required for use as an ultrashort optical probe.

4.3.1 White Light Supercontinuum Generation

To achieve the desired spectral bandwidth for the probe pulse, the NOPA must be seeded with an ultrabroadband ($\Delta\lambda > 150$ nm) pulse. Here, white light supercontinuum [156,157] (WLC) via free-electron plasma generation and ultrashort pulse self-filamentation is a promising method to generate stable [158] pulses with high spatial and temporal coherence and spectra exceeding an octave of optical frequencies [159,160]. By choosing the appropriate combination [159,161] of pump pulse numerical aperture (NA), material, and thickness, the WLC pulse can be self-guided within the material via a balancing of self-focusing and plasma defocusing. Throughout the guided nonlinear propagation, a strong broadening of the spectrum occurs due to self-phase modulation (section 2.4.3), leading to a nJ-level ultrabroadband pulse that can be amplified via NOPA [32,158,162].

To generate the WLC pulse, 0.1% (2 µJ) of the amplified pulse from the Yb:FP15-based CPA system (described in section 4.2.2) was directed into the compact "white light generator" depicted in Fig. 54. Here, YAG (yttrium aluminum garnate, $\mathrm{Y_3Al_5O_{12}}$) was employed as the WLC material due to its high damage threshold [163], lack of birefringence, and high nonlinear refractive index, which results in a large, flat continuum spectrum [156] and a reduced power threshold ($P_{\mathrm{cr}} = 1.4$ MW) for self-focusing. To produce a stable white light supercontinuum, an iterative approach was applied, in which the distance from the 50 mm focal length lens to the 5 mm thick YAG crystal along with the input intensity and numerical aperture using a variable neutral density filter (VND in Fig. 54) and iris, respectively, were adjusted. The most stable, broadband output was determined using an NA of 0.02 with the focusing lens placed 47 mm before the front surface of the YAG crystal. The VND was set to an optical density of 0.4, resulting in an input pump energy for the stable WLC of 720 nJ and an input power of 6 MW ($\sim 4.3 \cdot P_{\mathrm{cr}}$) that lies directly between two unstable power regimes [158] of the first self-focusing event (4 MW) and the filament refocusing (8 MW).

The output beam was collimated using a 12.7 mm diameter 90° off-axis parabola (OAP) with a reflected focal length of 25.4 mm. The OAP was mounted on a 5-axis manual stage for precise alignment. After collimation, the WLC pulse passes through a high-pass frequency filter (cutoff starting at 950 nm) to avoid optical parametric amplification in the spectral regime too close to that of the POLARIS main pulse ($\lambda_\mathrm{L} = 1030\,\mathrm{nm}$, $\Delta\lambda = 18\,\mathrm{nm}$ FWHM). Spectral filtering of the high-frequency components of the probe pulse near the second harmonic wavelength ($\lambda_\mathrm{L} = 515\,\mathrm{nm}$) is accomplished within the optical parametric amplification process automatically via phase-matching. The stable spatial (1.4 mm FWHM) and spectral ($\lambda_\mathrm{L} = 807\,\mathrm{nm}$, $\Delta\lambda = 287\,\mathrm{nm}$ FWHM) profiles of the WLC pulse are given in Fig. 55. For the initial alignment of the WLC pulse as well as for ultrashort temporal synchronization (described in section 4.4) purposes, the YAG crystal within the magnetic mount along with the high-pass filter can be easily removed to allow the higher power pump pulse through the NOPA setup.

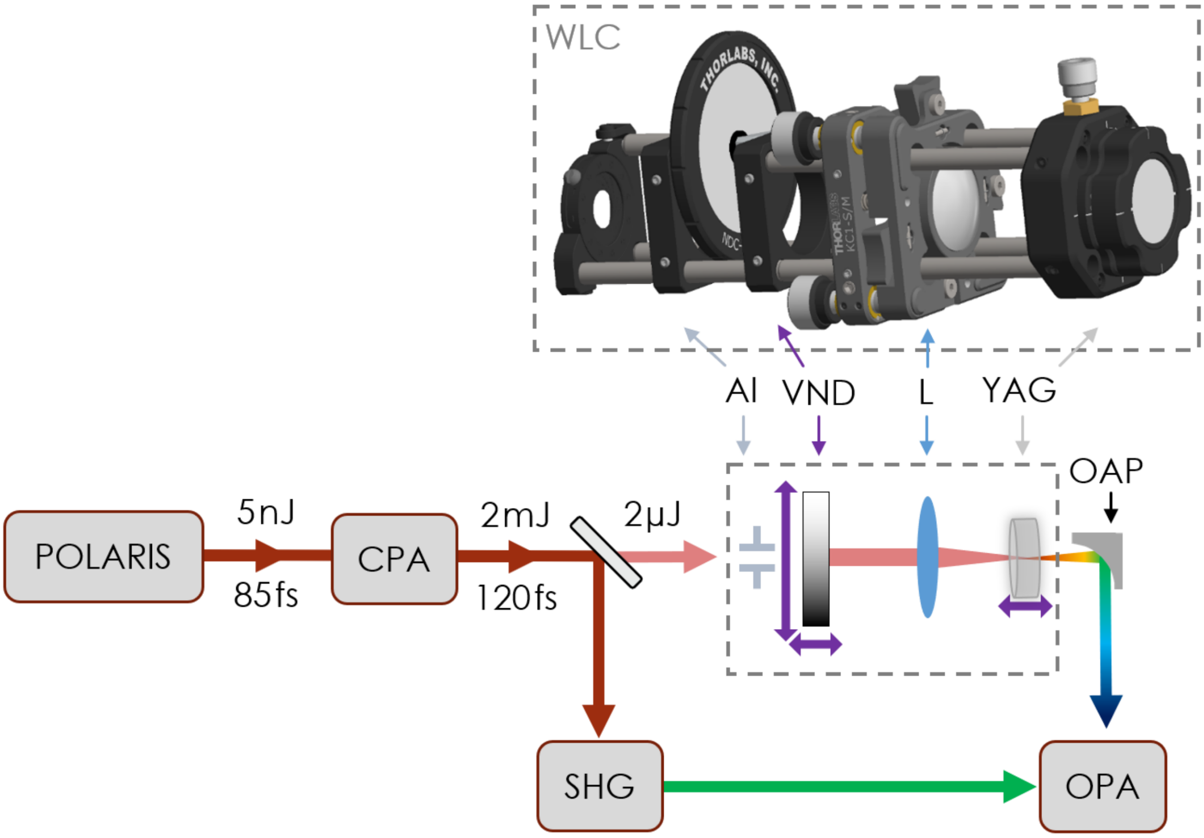

Figure 54: Schematic (bottom) of the NOPA with an emphasis on the white light supercontinuum generation. An amplified pulse originating from the POLARIS oscillator enters a "white light generator" (top) that consists of an adjustable iris (AI), variable neutral density filter (VND), 50 mm focal length lens (L) and 5 mm YAG crystal. The stable WLC pulse is collimated using a 25.4 mm focal length off-axis parabola (OAP) mounted on a 5-axis stage before being amplified in the OPA stage by the second harmonic (SH) pulse.

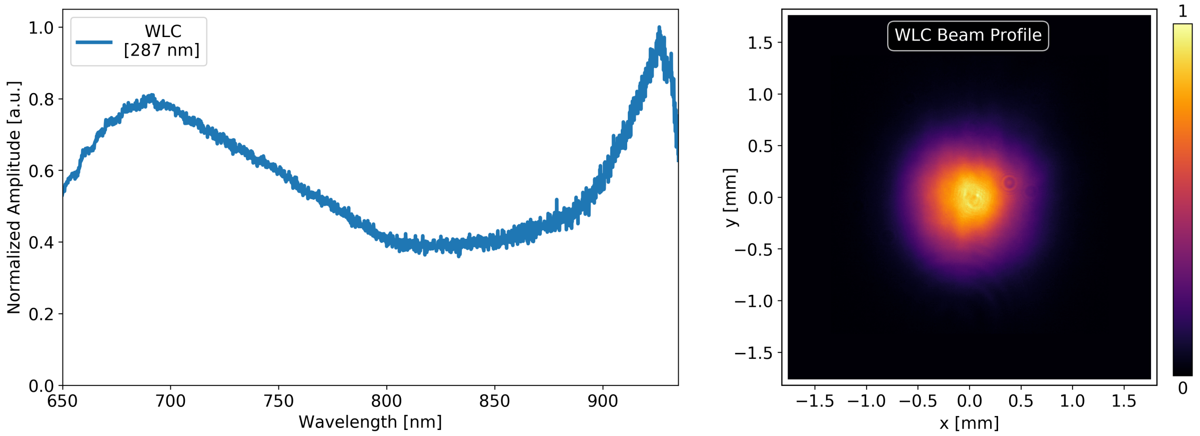

Figure 55: Measured spectral (left, $\lambda_L = 807$ nm, $\Delta\lambda = 287$ nm FWHM) and spatial (right, 1.4 mm FWHM) profiles of the WLC pulse. A large portion of the WLC spectrum, outside the measurable range of the calibrated Flame-S spectrometer and filtered above 950 nm, was not amplified within the OPA crystal to avoid overlap with the POLARIS spectrum and harmonics.

4.3.2 Second Harmonic Generation

To amplify the desired frequencies contained within the spectrum of the WLC pulse, the high intensity pump pulse (150 GW/cm^2, described in section 4.2.2) was frequency-doubled to satisfy the phase-matching conditions[17,32] (section 2.3) within the OPA crystal. As depicted in Fig. 56, the 2 mJ, 120 fs laser pulse was directed into a KDP (potassium dihydrogen phosphate, KH_2PO_4) crystal for second harmonic generation (SHG) of 1030 nm to 515 nm. To determine the proper crystal cut angle and thickness, the type I (o-o-e) SHG process was simulated using the RK4IP[39] method by solving the coupled differential equations (Eq. 44 with $\alpha = \beta = 0$) with the signal and idler wavelengths set to 1030 nm and the pump to 515 nm.

Although the effective nonlinearity d_{eff} of other popular nonlinear crystals such as BBO (β-barium borate, β-BaB_2O_4) are significantly higher[164,165], a 3 mm KDP crystal can achieve the same high conversion efficiencies with nearly 1/3$^{\text{rd}}$ the cost of a 1 mm BBO crystal. Furthermore, the effect of group velocity dispersion (70 fs^2/mm GVD) throughout the crystal thickness on the duration of the pump pulse is neglible due to the small SH bandwidth. The optimized 3 mm KDP crystal (phase-matching angle $\theta_{\text{PM}} = 41.2°$, $\phi_{\text{PM}} = 45°$) produced SH pulses ($\lambda_L = 515$ nm, $\Delta\lambda = 4$ nm FWHM) with a conversion efficiency of 65%, as seen in Fig. 57, confirming the results of the numerical simulation. By installing a telescope before the OPA crystal and adjusting the SH pulse energy to 1 mJ, the desired NOPA pump intensity of approximately 200 GW/cm^2 could be achieved. A motorized delay stage was built into the SHG path to temporally synchronize the ultrashort WLC and SH pulses within the OPA crystal.

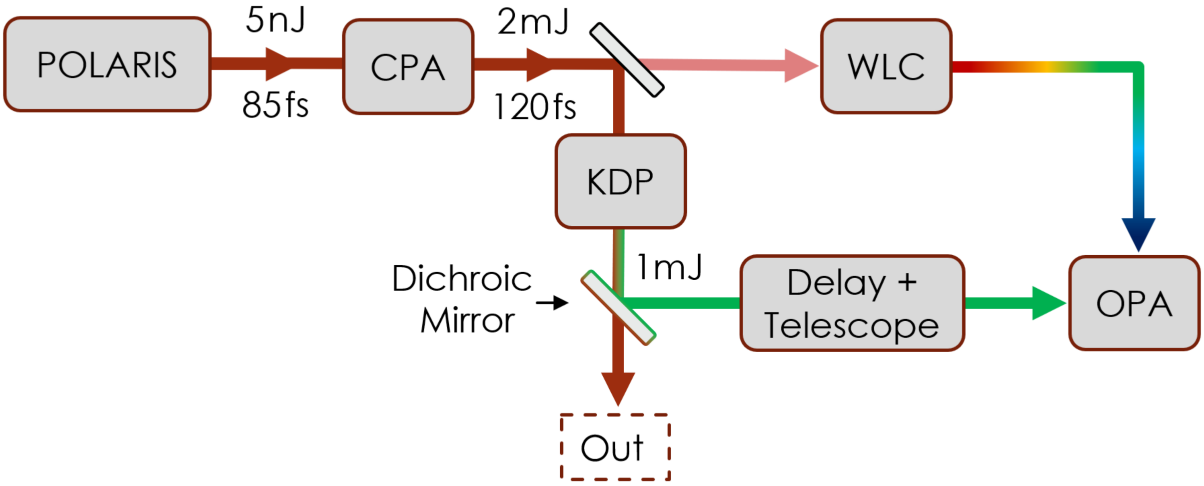

Figure 56: Schematic of the NOPA with an emphasis on the second harmonic generation. An amplified pulse originating from the POLARIS oscillator enters a 3 mm thick KDP crystal to generate a mJ-level, ultrashort pulse at 515 nm to pump the NOPA at 200 GW/cm^2. Using a motorized delay stage, the WLC and SH pulses were temporally synchronized within the OPA crystal.

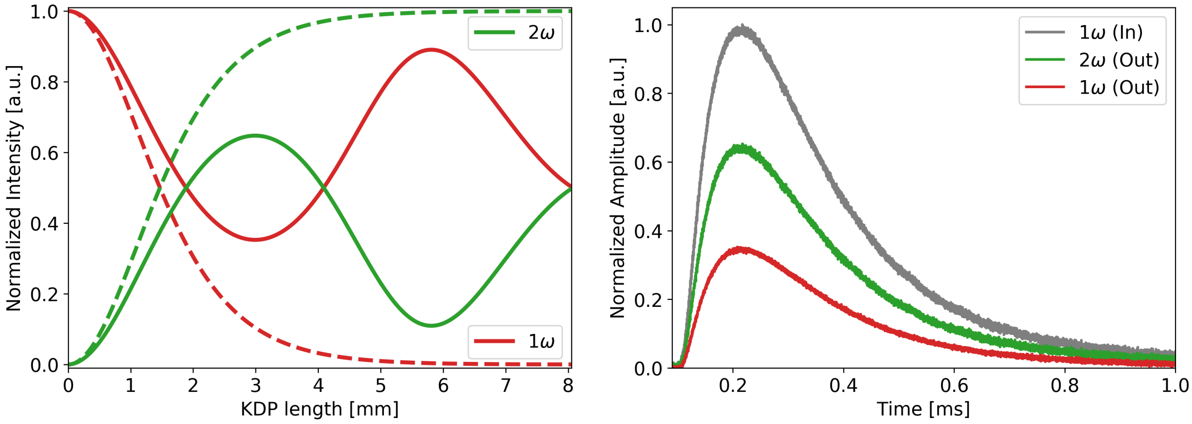

Figure 57: 1D simulation (left) of the SHG efficiency vs. KDP crystal length. The analytical calculations (dashed) neglect dephasing and dispersion, while the simulated (solid) results include all relevant nonlinear and dispersion terms. Measured SHG conversion efficiency (right) of 65% (given by the maximum value) after the 3 mm KDP crystal using a calibrated pyroelectric detector on both sides of a dichroic (1ω transmission, 2ω reflection) mirror.

4.3.3 Noncollinear Optical Parametric Amplifier

Within the nonlinear optical parametric amplification process, a high intensity pump pulse transfers its energy to a weaker signal pulse with lower frequency when the phase-matching conditions are fulfilled. As the difference in the pump and signal photon energies is utilized in the generation of an additional idler pulse, there is intrinsically no energy storage or quantum defect in OPA, allowing for energy scaling up to the multi-petawatt-class[34] at high repetition rates. Additionally, ultrabroadband pulses can be amplified with a single-pass gain of several orders of magnitude[32]. To apply this powerful process for the generation of an ultrashort optical probe, the previously described WLC and SH pulses were spatio-temporally overlapped within a highly nonlinear crystal at an optimized angle for broadband NOPA.

BBO (β-barium borate, β-BaB$_2$O$_4$) was chosen as the OPA crystal due to its optimum combination[166] of both high effective nonlinearity ($d_{\mathrm{eff}} = 2.08\,\mathrm{pm/V}$; the nonlinear gain factor G$_0$ in Eq. 34 scales exponentially with d_{eff}) and broad phase-matching bandwidth at a low noncollinear angle, unlike other nonlinear crystals[165] such as KDP (potassium dihydrogen phosphate, KH$_2$PO$_4$), LBO (lithium triborate, LiB$_3$O$_5$), and BiBO (bismuth triborate, BiB$_3$O$_6$). The main disadvantage of BBO in the context of a µJ-level ultrashort probe is the high spatial pump/signal walk-off angle of $\rho = 3.3°$[18], the impact of which on the broadband OPA gain can be partially compensated by the combination of a small pump/signal cross angle, thin crystal (stronger pumping[167] is required), and unfocused pump and signal beams.

A schematic of the realized ultrashort optical probing setup is depicted in Fig. 58. The multi-beam output simultaneously offers a 1 mJ, 120 fs fundamental pulse at $\lambda_{\mathrm{L}} = 1030\,\mathrm{nm}$ from a POLARIS oscillator-seeded CPA system (section 4.2.2), a 1 mJ second harmonic pulse, and a µJ-level, few-cycle NOPA pulse seeded with white light supercontinuum. The BBO crystal utilized within the NOPA was cut for type I (o-o-e) phase-matching ($\theta_{\mathrm{PM}} = 24.5°$, $\phi_{\mathrm{PM}} = 90°$) with a thickness of 2 mm, chosen to reduce the effects of dephasing and spatio-temporal walk-off, while still providing an anticipated ultrabroadband gain exceeding 10^4 with a pump intensity of 200 GW/cm^2. The tangential phase-matching orientation[170] of the optical axis was chosen to avoid parasitic SHG of the seed, which can significantly modulate the output spectral profile. As the pump (SH) pulse enters the θ_{PM}-cut OPA crystal, a bright parametric superfluorescence (PSF) ring is emitted (displayed in Fig. 59) in the propagation direction of the pump pulse that can be utilized as a guide for the alignment of the signal (WLC) pulse. When the pump and signal pulses are spatio-temporally overlapped in the crystal at the proper angle, the PSF ring disappears and the WLC pulse is amplified via NOPA.

As described in section 2.3, the NOPA spectral gain profile and bandwidth is strongly dependent on the pump/signal cross angle α. For the intended application of the NOPA pulse as an optical probe for relativistic laser-plasma interactions, broadband pulses with ultrashort compressible pulse durations are required. Furthermore, particularly for chirped

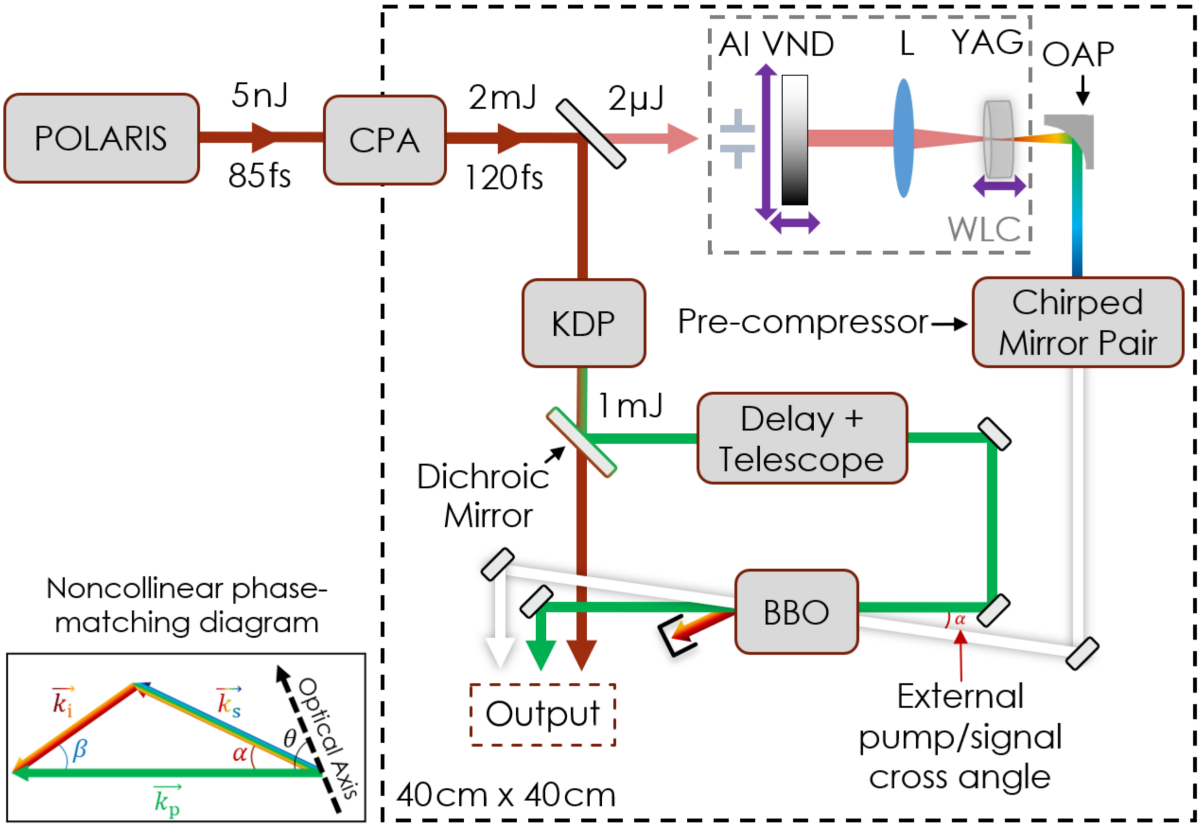

Figure 58: Schematic of the ultrashort optical probing system with mJ-class fundamental and SH pulses and an ultrabroadband μJ, few-cycle NOPA pulse. Within the NOPA setup, an amplified pulse originating from the POLARIS oscillator is utilized to generate WLC and SH pulses, which were temporally synchronized within an OPA crystal at a specific pump/signal cross angle designed for broadband WLC amplification.

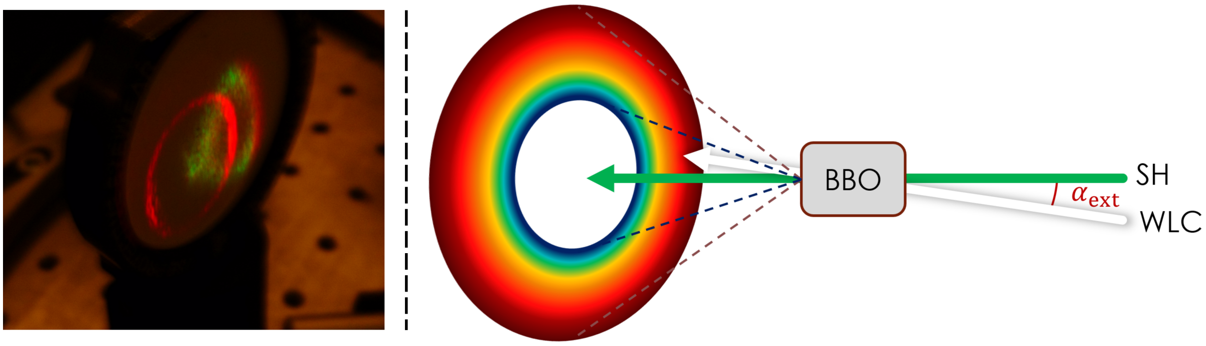

Figure 59: Image (left; captured through a low-pass filter with 550 nm cutoff to block the pump pulse) and schematic (right; colors in figure for visualization purposes only) of parametric superfluorescence (PSF) ring generation via intense pumping of an OPA crystal. The PSF ring, which disappears at the onset of NOPA, can be utilized as an optical guide for spatio-temporal alignment of the pump and signal pulses. The asymmetric spectral features within the PSF ring are due to a combination of cascaded nonlinear effects[35], optical axis orientation of the OPA crystal[168], and scattering[169].

pulse[153] and spectrally resolved probing techniques[171,172], the full spectrum of the pulse contains important spatio-temporal information[112] about the plasma dynamics that may be lost in the low energy spectral regions of the probe pulse within the plasma. Therefore, the pump/signal cross angle must be optimized to produce a homogeneous spectral gain profile for the single-pass NOPA gain exceeding 10^4.

As seen in Fig. 60, a slight detuning – even on the order of 0.1° – away from the optimized α_{int} value of 2.6°, determined within the theoretical evaluation in Fig. 9 of section 2.3.2, leads to a phase-mismatch contribution that has a drastic effect on the shape and width of the gain spectrum. However, the results of the numerical treatment of the pump/signal cross angle optimization given in Fig. 60 reveal that a smaller detuning of 0.05° offers the possibility of shaping the spectral form towards the blue or red region – allowing for a compensation for inhomogeneities within the signal spectrum – while maintaining the ultrabroadband amplifica-

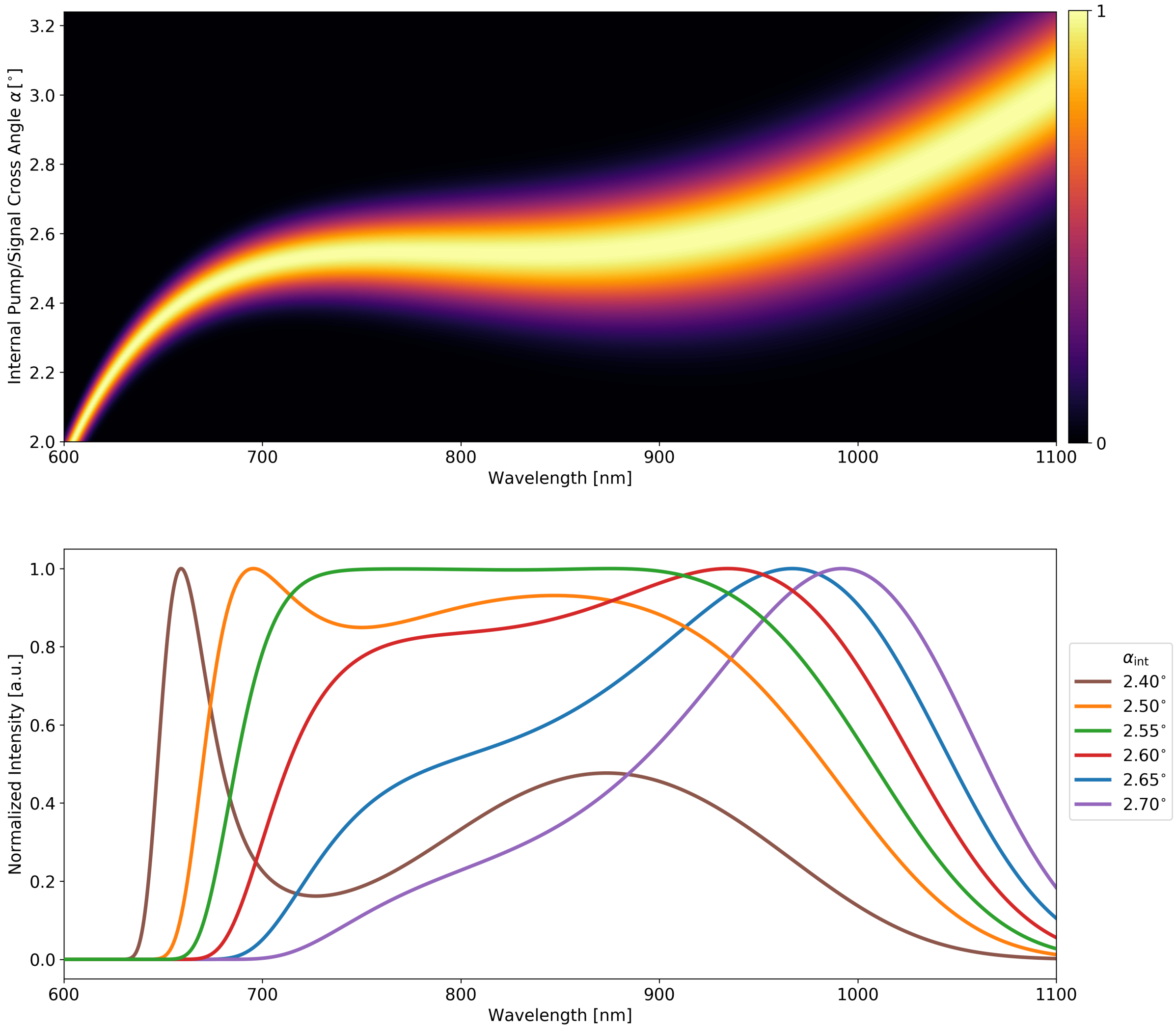

Figure 60: Numerical calculation (top) of the internal pump/signal cross angle α_{int} for the NOPA. Lineouts of the gain spectra (bottom) show that a combination of ultrabroadband amplification and spectral shaping is possible within the small range of $\alpha_{\text{int}} = 2.55^\circ \pm 0.05^\circ$.

tion. The numerical calculation using the optimized α_{int} of 2.55° produced a flat-top spectral gain profile with a unity amplification from $700 - 950\,\mathrm{nm}$, ideal for the input WLC spectrum.

Before entering the BBO crystal to initiate the optical parametric amplification, the WLC pulse was pre-compressed using a pair of chirped mirrors (-40 fs^2 per bounce at 6° AOI, Layertec GmbH) to compensate for the material dispersion within the 5 mm YAG (490 fs^2 GDD) and 2 mm BBO (150 fs^2 GDD). Additionally, this pre-compression allowed for a near-matching of the expected WLC and SH (λ_{L} = 515 nm, $\Delta\lambda_{\mathrm{L}}$ = 4 nm FWHM, $\tau \geq \tau_{\mathrm{FTL}}$ = 98 fs) pulse durations at the entrance of the BBO crystal, improving the temporal overlap. Within the NOPA setup, the BBO crystal functions not only as the nonlinear amplification medium, but also as the pulse compressor. Here, with the GDD-compensation enabled by the chirped mirrors, the amplified pulse is calculated to be nearly Fourier transform limited at the NOPA output without the need for further spectral phase modifications.

Another important consideration for the fs-NOPA is the temporal drift of the ultrashort pump and signal pulses while propagating through the OPA crystal. Here, the high dispersion of the 2 mm BBO forces a considerable temporal walk-off, as the group velocity of the WLC (signal) pulse $v_{\mathrm{g,s}}$ is higher than the group velocity $v_{\mathrm{g,p}}$ of the SH (pump) pulse. The resulting temporal displacement $\tau_{\mathrm{p,s}}$ between the pump and signal pulses at the end of the crystal with thickness L can be determined via $\tau_{\mathrm{p,s}} = L \cdot \left(v_{\mathrm{g,p}}^{-1} - v_{\mathrm{g,s}}^{-1}\right)$. For the fs-NOPA system, the temporal clipping due to an unoptimized pump/signal delay not only reduces the small signal gain, but also the spectral bandwidth. For example, when the two pulses are synchronized at the start of the crystal, the strongly chirped signal pulse experiences spectral gain narrowing throughout pulse propagation, as the slower pump pulse interacts mainly with the frequencies located in the trailing edge of the signal pulse. However, by adjusting the temporal synchronization (i.e., the initial delay) between the pump and signal pulses, the impact of the temporal walk-off of $\tau_{\mathrm{p,s}} = 100\,\mathrm{fs}$ on the small signal gain and spectral bandwidth within the crystal can be mitigated.

First, the starting location $t_1 = t_0 + \frac{\tau_{\mathrm{p}}}{2} + \frac{\tau_{\mathrm{s}}}{2}$, where the two pulse centers are estimated to be synchronized at the start of the BBO crystal, was set by changing the optical path length of the pump pulse beamline using a motorized linear stage exhibiting a resolution of 1.25 µm = 4 fs per partial step (10 µm = 33 fs per full step). Here, the coordinate t_0 represents the onset of optical parametric amplification, where the the leading edge of the pump pulse meets the trailing edge of the signal pulse at the front surface of the BBO crystal. The values τ_{p} and τ_{s} correspond to the pulse durations of the pump and signal pulses, respectively. Shifting the pump pulse to $\tau_{\mathrm{opt}} = t_1 + \tau_{\mathrm{p,s}} = 200\,\mathrm{fs}$ ahead of the signal pulse trailing edge at the crystal entrance allows for the preservation of the high ($\geq 10^4$) gain, as the pulses remain temporally overlapped throughout the majority of the crystal length. By the end of the BBO crystal, where the largest energy transfer occurs, the peak of the pump pulse is aligned with the signal pulse, which is compressed due to the GDD pre-compensation by the chirped mirrors.

For spectrally resolved probing techniques, a homogeneous or flat-top-like spectrum may be desirable. Here, the fs-NOPA offers a powerful method of spectral gain control through a combination of the pump/signal cross angle α_{int} and the pump/signal delay τ_{delay}, with the capability of compensating for the large gap in the WLC spectrum near the central wavelength in Fig. 55. To find the global optimization scheme leading to an ultrabroadband, homogeneous spectral profile, the measured WLC spectrum was inserted into the numerical simulation of the type I fs-NOPA, with α_{int} and τ_{delay} as the variables to be solved. Here, the amplified WLC spectrum could be homogenized by introducing a red-shift via angle-tuning towards larger α_{int} values and a compensating blue-shift from a slight offset of τ_{delay} with respect to τ_{opt} – effectively setting the pump further ahead of the negatively chirped signal pulse, where the blue frequencies are leading. The impact of the multiple delay configurations for the optimized case with $\alpha_{\mathrm{int}} = 2.65^\circ$ on the simulated (left) and the realized (right) NOPA spectra are given in Fig. 61. The pump/signal delay $\tau_{\mathrm{delay}} = \tau_{\mathrm{opt}}$ recovers the calculated (assuming the maximum temporal overlap) gain spectrum for $\alpha_{\mathrm{int}} = 2.65^\circ$ shown in Fig. 60. From the results of the numerical model, verified through measurements of the NOPA spectral profile, a pump delay of $+33$ fs with respect to τ_{opt} produced the broadest, flat-top-like spectrum with a FWHM bandwidth of 230 nm at a center wavelength of $\lambda_{\mathrm{L}} = 820$ nm. With this configuration, the compact (40 cm × 40 cm) setup offers an ultrabroadband, nearly Fourier transform limited NOPA pulse directly at the output of the 2 mm BBO crystal. The final spectrum and pulse duration, as seen in Fig. 62 were measured using a high resolution (HR2000+) Ocean Optics spectrometer and a WIZZLER (Fastlite, self-referenced spectral interferometry[173]). The amplified pulse energy of 20 µJ is to-date the highest pulse energy achieved within a single-pass for a femtosecond-pumped broadband NOPA system[162,174–187].

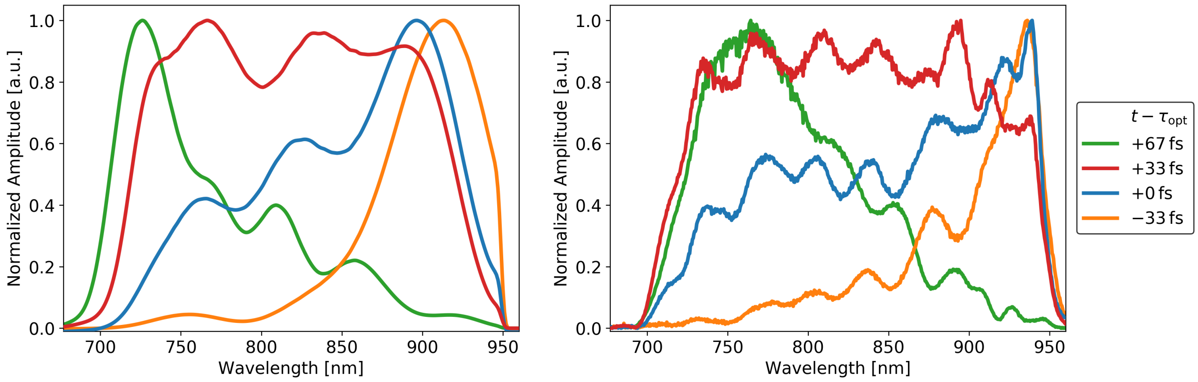

Figure 61: Simulated (left) and measured (right) NOPA spectra for various pump/signal delays, with $t = \tau_{\mathrm{delay}}$ representing the temporal alignment of the pump and signal pulses. To homogenize the amplified WLC spectrum, a global optimization resulted in a tuning of the pump/signal cross angle α_{int} to 2.65° for a red-shift and the pump/signal delay to $\tau_{\mathrm{delay}} = \tau_{\mathrm{opt}} + 33$ fs for the compensating blue-shift.

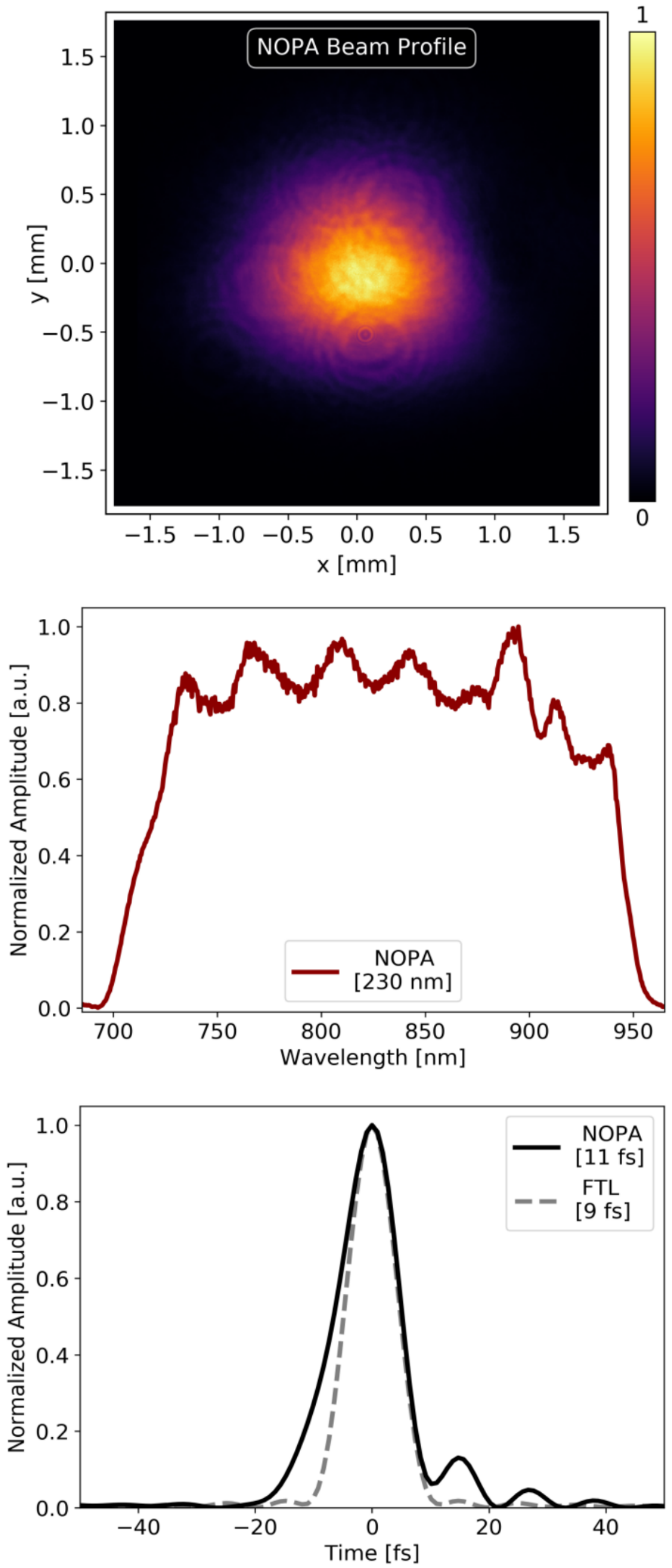

Figure 62: Spatial profile (top, 1.8 mm $1/e^2$ diameter) of the NOPA pulse with spectral profile (center) and pulse duration (bottom) directly after the BBO crystal. The output pulse duration nearly matches the FTL value without additional dispersion control. Values in the legends describe the FWHM spectral bandwidth (center) and pulse duration (bottom).

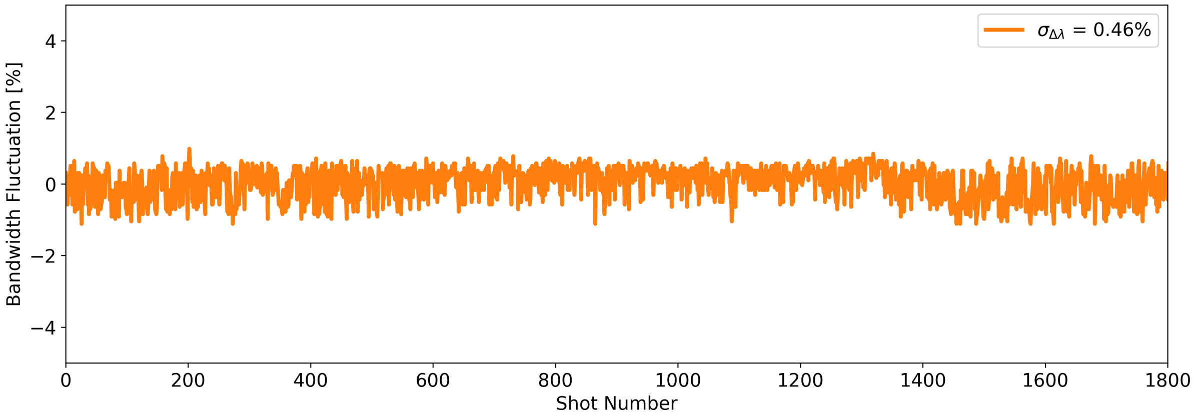

Figure 63: Spectral bandwidth fluctuation $\sigma_{\Delta\lambda}$ of the NOPA pulse over 1800 pulses at a repetition rate of 1 Hz. The NOPA spectrum maintains its bandwidth with an RMS fluctuation of 0.46%.

The results of the POLARIS oscillator-seeded, Yb:FP15-based CPA-pumped, fs-NOPA output of the multi-beam ultrashort optical probing setup simultaneously fulfill the design criteria described in section 4.1. The NOPA beam diameter of 1.8 mm $1/e^2$ (1.1 mm FWHM), slightly smaller than the WLC beam diameter due to spatial gain narrowing, is sufficient to encapsulate the interaction region. The pulse duration at the BBO output is 11 fs, with a Fourier transform limited pulse duration of 9 fs. The ultrabroadband spectrum, with central wavelength $\lambda_\mathrm{L} = 820$ nm and 230 nm FWHM bandwidth, does not overlap with the spectral regions (fundamental and second harmonic) susceptible[151,152] to plasma emission, nonlinear scattering, and reflection. Furthermore, the collimated intensity $I_\mathrm{L} < 10^{11}$ W/cm^2 of the 20 µJ NOPA pulse is below the ionization threshold of the target materials. Finally, the spectral bandwidth stability, given in Fig. 63, is particularly relevant for spectrally resolved probing of laser-plasma interactions and was measured to be 0.46% RMS over 1800 consecutive pulses.

4.4 Ultrashort Pump-Probe Synchronization

To apply the probe pulses – mJ-class 1ω and 2ω outputs along with the NOPA – to experimental campaigns utilizing the ultrashort POLARIS laser pulse, the two systems, which are seeded by two separate pulses originating from the same oscillator, must first be synchronized. Although the optical path lengths between the pulses differ by hundreds of meters, the pump (POLARIS main pulse) and probe (e.g., NOPA pulse) lasers can be temporally aligned at the target plane with a precision on the femtosecond level. Here, a measurement setup is required that is capable of monitoring several orders of magnitude of delay between the two systems.

The delay diagnostic utilizes leakage light from the POLARIS laser pulse after the plasma mirror diagnostic (Fig. 43, details in section 3.3.1) and leakage light from the multi-beam probing setup. To measure the temporal position of the two systems on the nanosecond timescale, corresponding to a precision of 30 cm optical path length difference, a Thorlabs DET36A/M photodetector coupled to a 500 MHz Tektronix (TDS3054C) oscilloscope was used. Pulses from the POLARIS laser and the probing setup were temporally aligned by first selecting the nearest probe seed pulse from the POLARIS oscillator with the pulse picker (Fig. 51) and installing a compact delay stage at the entrance and output of the probe system for fine-tuning. The delay of the probe pulse was shifted until the measured pump and probe signals on the oscilloscope overlapped. To synchronize the pulses on the picosecond timescale, multiple techniques must be employed, depending on the desired precision, displacement range, and laser wavelength. For the temporal alignment on the order of approximately 30 ps, the pulses were directed into a fiber-coupled Thorlabs DXM30BF photodetector attached to an 8 GHz Keysight (DSOV08A4) oscilloscope and synchronized using the probe delay stage.

To achieve a high resolution for measurements on the picosecond level, Fourier transform spectral interferometry[188] and an optical logic gating setup were installed into the delay diagnostic. The spectral interferometry technique combined the leakage light from the POLARIS pulse with the fundamental pulse from the probe system at the plane of a Flame-S spectrometer. When the two pulses were temporally aligned within a window of approximately 6 ps, a characteristic fringe pattern appeared on the combined spectral profile from both pulses, as seen in Fig. 64. The near-zero delay could be confirmed via a recovery of the null fringe. For the second harmonic (2ω) probe pulse, the colored glass filter OG550[189] was employed as a saturable absorber and optical logic gate[190]. Here, the POLARIS leakage pulse was converted to the second harmonic using a 3 mm KDP crystal ($\theta_{\mathrm{PM}} = 41.2°$). The 50 GW/cm^2 2ω pump pulse, separated from the fundamental light using a dichroic mirror, pumped the 2 mm OG550 sample and saturated the absorption, forcing transmission within the sample with an experimentally determined fluorescence lifetime of 1.6 ps. Within this time frame, the 2ω probe pulse could be temporally aligned using the delay stage to pass through the saturated region and onto the detector screen in Fig. 64.

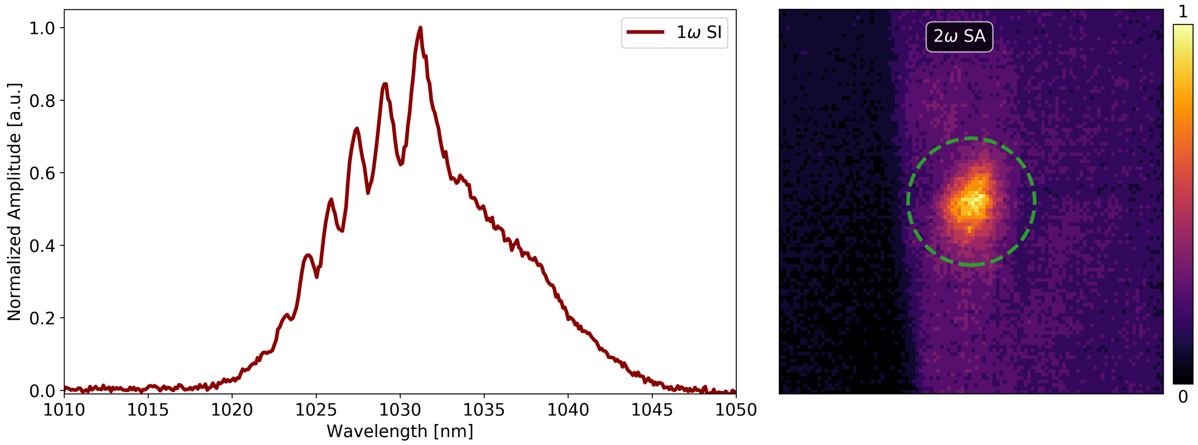

Figure 64: Characterization techniques for the picosecond synchronization between the ultrashort POLARIS and probe pulses. Spectral interferometry (SI, left) was utilized for the leakage pulses at the fundamental (1ω) frequency. When the two pulses are aligned within approximately 6 ps, a fringe pattern appears within the spectral profile that can be analyzed using the Fourier transform method to determine the temporal displacement. Here, only half (1020 nm - 1030 nm) of the POLARIS spectrum was combined with the full 1ω-probe in a temporary configuration that clearly displays the difference between the real fringes and possible high frequency spectral amplitude modulations. For the second harmonic pump and probe pulses, a saturable absorber (SA, right) operating as an optical logic gate allowed the weaker probe pulse (outlined in green) to pass through the saturated region and onto a detector screen within the fluorescence time of 1.6 ps.

To temporally synchronize the POLARIS and probe pulses on the femtosecond level, the 230 nm FWHM bandwidth of the NOPA can be used. Here, a separate, compact (40 cm × 40 cm) NOPA was installed within the diagnostic setup to provide a fs-displacement characterization that can be employed live during the experimental campaign. As seen in the schematic in Fig. 65, a small fraction of the NOPA pulse is leaked out of the probing setup and chirped using a bulk stretcher to a pulse duration of 1 ps. The leakage NOPA pulse is then directed into a BBO crystal at the internal pump/signal cross angle $\alpha = 2.55°$ for ultrabroadband noncollinear optical parametric amplification. The ultrashort POLARIS leakage pulse from the plasma mirror diagnostic setup was converted to the second harmonic to pump the 2 mm BBO crystal and amplify the stretched NOPA leakage pulse with an output central wavelength depending on the temporal alignment of the two pulses. When the amplified peak wavelength matches the central wavelength of the NOPA pulse, the two pulses are synchronized. The temporal resolution is dependent on the spectrometer, with an experimentally determined calibration of 5 fs/nm, while the temporal window is variable with the pulse duration (1 ps) of the stretched pulse. An example of the fs-delay diagnostic spectra measured at various POLARIS/NOPA delays is given in Fig. 66.

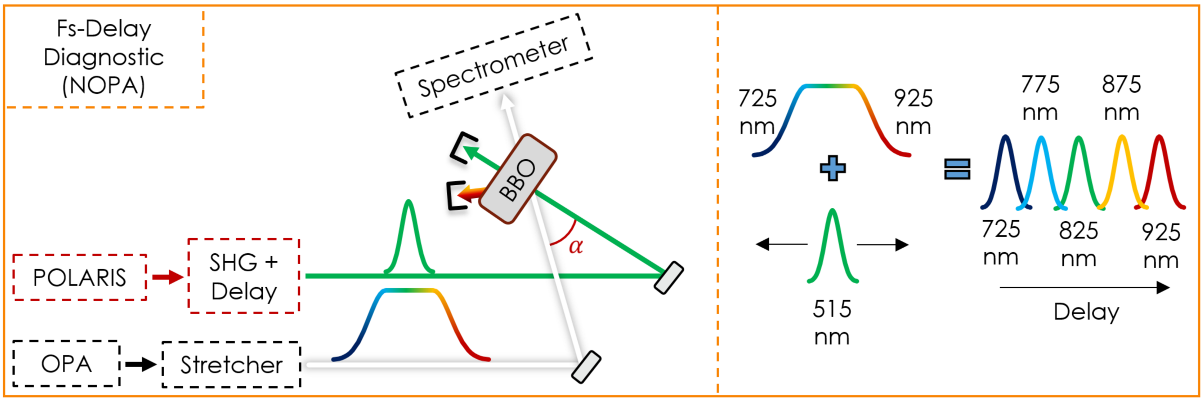

Figure 65: Schematic of the fs-delay diagnostic based on ultrabroadband NOPA. The leakage NOPA pulse is temporally stretched and amplified within a BBO crystal using the 2ω POLARIS leakage pulse under an internal pump/signal cross angle $\alpha = 2.55°$. The central wavelength of the output NOPA pulse is determined by the temporal overlap between the two pulses.

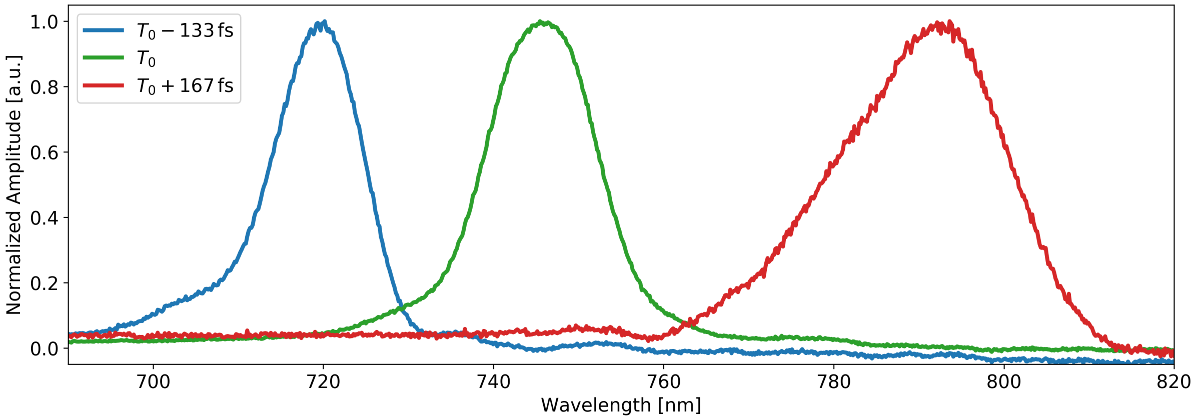

Figure 66: Results of the live fs-delay diagnostic at various POLARIS/NOPA delays. The peak wavelength of the amplified leakage NOPA pulse can be directly correlated to the temporal alignment between the pump and probe pulses. The time T_0 within the figure represents a random delay generated to test the setup; adjusting the delay stage after the probing setup allows for a correction of the temporal offset with femtosecond level precision (1.25 µm = 4 fs per partial step and 10 µm = 33 fs per full step).

4.5 Burst-Mode and Chirped Pulse Optical Probing

The multi-beam ultrashort optical probing system can be applied to a variety of pump-probe setups for investigations of laser-plasma interactions. At the POLARIS laser system, the first application will require a stretching of the few-cycle NOPA pulse from 11 fs to 1 ps using, e.g., a YAG rod and the target chamber entrance window (2.5 cm BK7). In a chirped pulse probing[153] configuration, the stretched pulse passes through the interaction region and onto an imaging spectrometer, where spatio-temporal information from the interaction is directly encoded into the spectrum within the time frame of the probe pulse duration. Here, the onset of processes such as relativistic induced transparency[149] can be resolved by analyzing the remaining amplitude of the spectral components of the probe pulse, with each corresponding to a different time frame of the laser-plasma interaction.

For investigations involving, for example, dedicated pre-plasma generation utilizing the mJ-class 1ω or 2ω pulses offered by the probing setup, the spatio-temporal information of both the nanosecond plasma expansion and the femtosecond laser-plasma interaction are critical for a more detailed understanding of the complex processes. With the advent of burst-mode optical probing techniques, multiple frames of the laser-plasma interaction across a large temporal window can be captured with a single shot[171,172]. As seen in the schematic of the proof-of-principle setup in Fig. 67, the ultrabroadband NOPA pulse is split into the desired number of pulses, each with a variable delay, using a demultiplexer-like configuration consisting of a grating and a series of adjustable mirrors within an imaging setup. After the ultrashort optical probe pulses propagate through the interaction region, they are spatially separated with a vertically displaced multiplexer and directed into a camera array for shadowgraphy or an interferometer to recover the spatio-temporal information of the laser-plasma interaction.

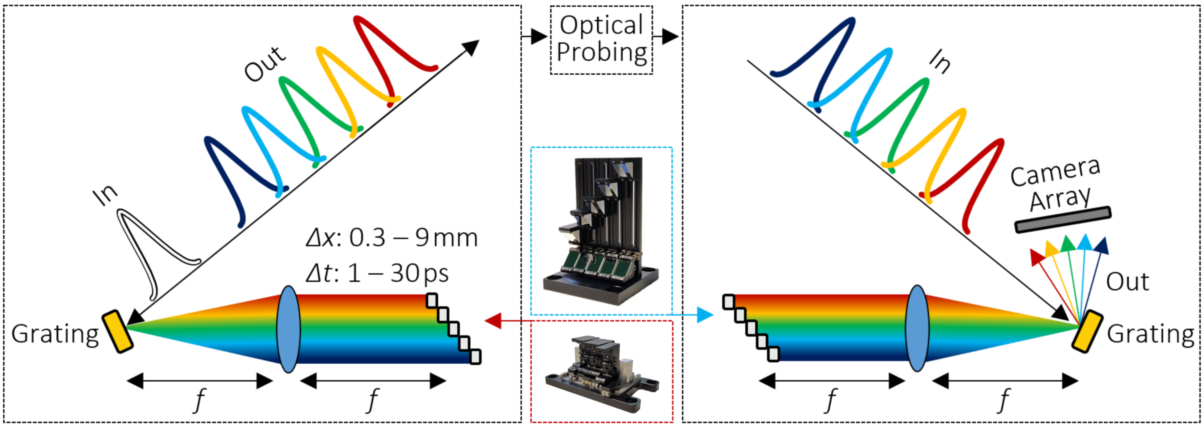

Figure 67: Schematic of the burst-mode optical probing setup. The ultrabroadband NOPA pulse is separated into multiple pulses at various delays that propagate through the interaction region. The pulses are then spatially separated and analyzed to reveal the spatio-temporal information of the laser-plasma processes over a large temporal window with adjustable intermediate time steps in a single shot.

5 Conclusion

State-of-the-art laser technology has driven progress in research topics that can enable significant improvements in a variety of scientific, medical, and commercial applications. Nowadays, the world's most powerful lasers are utilized to generate extreme states of matter within the laboratory and explore exciting regimes in relativistic laser-plasma physics. As a prominent example, the POLARIS[14] laser system at the Friedrich Schiller University and Helmholtz Institute in Jena, Germany, generates laser pulses with on-target intensities exceeding $10^{20}\,\mathrm{W/cm^2}$ that can accelerate charged particles from nanometer-thin foils towards the speed of light. The energetic protons and relativistic electrons that emerge from laser-based acceleration processes can, for example, be employed in precision cancer therapy[8] or even for high energy particle colliders[191].

The continued success[78] of such experiments demands further developments in present-day high peak power laser systems. As the laser pulse intensity is increased, however, the laser pulse's spatial and temporal distribution and temporal intensity contrast profile begin to dominate the experimental performance[79] of the laser system. Furthermore, the techniques employed to optimize these parameters must be capable of significant improvements under minimal changes to the existing and operational petawatt-class system. In addition to the laser system enhancement, higher experimental yields also require an understanding of the complex dynamics of laser-plasma interactions. Here, an ultrashort optical probing setup can be installed within the system and utilized in a pump-probe configuration with the main laser pulse to provide direct access to the intricate details – e.g., spatio-temporal evolution of the plasma density profile[112] – otherwise obscured by the intense plasma scattering[152] from the interaction region.

The work contained within this thesis explores two major themes: petawatt-class laser optimization at POLARIS and the development of a multi-beam ultrashort optical probing system. With knowledge from the fundamental concepts described in the second chapter, a broad investigation is conducted to overcome the limiting factors regarding the spatial and temporal distribution and temporal intensity contrast (TIC) profile of the POLARIS laser pulse. The third chapter begins with the development of a comprehensive spatio-temporal model[23] of both the thermal and electronic contributions to pump-induced optical path difference (OPD) profiles in Yb-doped materials. These OPDs can be produced within all pumped laser-active materials and can, if unaccounted for, lead to wavefront aberrations that significantly deteriorate the spatial profile of the amplified laser pulse. The numerical model of the pump-induced wavefront aberrations is verified using time-resolved interferometry and subsequently applied to a POLARIS joule-class multi-pass amplifier[97] with a double-sided 3D pumping configuration exhibiting an aberrated output beam profile, which restricts the maximum laser pulse fluence and focusability. The spatial profile degradations are corrected through a precise modification of the pump distribution to compensate the pump-induced high frequency spatial phase distortions, allowing for a further energy scaling of petawatt-class lasers such as POLARIS. Furthermore, the laser pulse intensity can be increased in parallel to the spatial optimization through a shortening of the pulse duration. Here, the bandwidth limitations of the laser system can be overcome by utilizing the high intensity of the pre-focus, compressed POLARIS laser pulse to enable self-phase modulation in the near field within thin, nonlinear plastics. The POLARIS pulse after the 1st CPA system was spectrally broadened in a single pass of 1 mm CR39 and recompressed to 40 fs – resulting in an intensity enhancement by a factor of three. Particularly for high peak power laser pulses with on-target intensities in excess of $10^{20}\,\mathrm{W/cm^2}$, improvements to the spatial and temporal profiles towards higher intensities must be accompanied by an additional suppression of the ASE pedestal and ps-rising edge. However, since multiple sources of TIC degradation exist within the laser system, a robust method is required to enhance the temporal intensity contrast by several orders of magnitude. For this purpose, a plasma mirror was installed and optimized at POLARIS, with a single AR-coated fused silica substrate – placed near the center of an imaging setup in the target chamber – providing a TIC improvement factor of 1250 at -14 ps before the main pulse and a factor of 500 at the trigger time of -4 ps. As a result, the experimental yield – i.e., accelerated proton cutoff energies – using a 20 nm thin DLC target was tripled.

For a more detailed understanding of the laser-plasma interactions produced by the upgraded POLARIS laser pulse, a multi-beam ultrashort optical probing system, described in chapter four, has been developed and installed in the target area. The probing system is seeded by a pulse generated within the POLARIS oscillator that is amplified in a dedicated Yb:FP15-based CPA system. The 2 mJ, 120 fs pulse is then utilized to pump a single-pass noncollinear optical parametric amplifier with an output pulse energy of 20 µJ, a spectral bandwidth of 230 nm FWHM, and a pulse duration of 11 fs. The compact probing system simultaneously offers the few-cycle NOPA pulse along with two mJ-class, ultrashort laser pulses at the POLARIS fundamental and second harmonic frequencies. All three probe pulses could be synchronized with the main laser system, which differs in optical path length by hundreds of meters, and the temporal alignment was characterized using a diagnostic setup that spans multiple orders of magnitude of temporal delay. Together, the completion of the multi-beam ultrashort optical probing system and the spatial, temporal, and temporal intensity contrast optimization of the petawatt-class POLARIS laser pulse are capable of providing the conditions for further breakthroughs in relativistic laser-plasma physics, with successful experimental campaigns having the potential to enable new applications and further drive the development of laser systems towards higher peak and average powers.

Literature

[1] T. H. Maiman, *Stimulated Optical Radiation in Ruby*, Nature **187**, 493 (1960).

[2] C. N. Danson, C. Haefner, J. Bromage, T. Butcher, J.-C. F. Chanteloup, E. A. Chowdhury, A. Galvanauskas, L. A. Gizzi, J. Hein, D. I. Hillier, N. W. Hopps, Y. Kato, E. A. Khazanov, R. Kodama, G. Korn, R. Li, Y. Li, J. Limpert, J. Ma, C. H. Nam, D. Neely, D. Papadopoulos, R. R. Penman, L. Qian, J. J. Rocca, A. A. Shaykin, C. W. Siders, C. Spindloe, S. Szatmári, R. M. G. M. Trines, J. Zhu, P. Zhu, and J. D. Zuegel, *Petawatt and exawatt class lasers worldwide*, High Power Laser Science and Engineering **7**, e54 (2019).

[3] J. W. Yoon, C. Jeon, J. Shin, S. K. Lee, H. W. Lee, I. W. Choi, H. T. Kim, J. H. Sung, and C. H. Nam, *Achieving the laser intensity of 5.5x10^{22} W/cm^2 with a wavefront-corrected multi-PW laser*, Optics Express **27**, 20412 (2019).

[4] M. D. Perry, D. Pennington, B. C. Stuart, G. Tietbohl, J. A. Britten, C. Brown, S. Herman, B. Golick, M. Kartz, J. Miller, H. T. Powell, M. Vergino, and V. Yanovsky, *Petawatt laser pulses*, Optics Letters **24**, 160 (1999).

[5] A. Azhari, S. Sulaiman, and A. K. P. Rao, *A review on the application of peening processes for surface treatment*, IOP Conference Series: Materials Science and Engineering **114**, 012002 (2016).

[6] T. Popmintchev, M.-C. Chen, P. Arpin, M. M. Murnane, and H. C. Kapteyn, *The attosecond nonlinear optics of bright coherent x-ray generation*, Nature Photonics **4**, 822 (2010).

[7] E. Esarey, C. B. Schroeder, and W. P. Leemans, *Physics of laser-driven plasma-based electron accelerators*, Reviews of Modern Physics **81**, 1229 (2009).

[8] K. Zeil, M. Baumann, E. Beyreuther, T. Burris-Mog, T. E. Cowan, W. Enghardt, L. Karsch, S. D. Kraft, L. Laschinsky, J. Metzkes, D. Naumburger, M. Oppelt, C. Richter, R. Sauerbrey, M. Schürer, U. Schramm, and J. Pawelke, *Dose-controlled irradiation of cancer cells with laser-accelerated proton pulses*, Applied Physics B **110**, 437 (2012).

[9] G. H. Miller, E. I. Moses, and C. R. Wuest, *The National Ignition Facility: enabling fusion ignition for the 21st century*, Nuclear Fusion **44**, S228 (2004).

[10] *LaserNetUS,* https://www.lasernetus.org.

[11] *Extreme Light Infrastructure,* https://www.eli-laser.eu.

[12] *Asian Symposium on Intense Laser Science,* http://www.jils.jp/ASILS7.

[13] M. Kaluza, J. Schreiber, M. I. Santala, G. D. Tsakiris, K. Eidmann, J. Meyer-Ter-Vehn, and K. J. Witte, *Influence of the laser prepulse on proton acceleration in thin-foil experiments*, Physical Review Letters **93**, 045003 (2004).

[14] M. Hornung, H. Liebetrau, S. Keppler, A. Kessler, M. Hellwing, F. Schorcht, G. A. Becker, M. Reuter, J. Polz, J. Korner, J. Hein, and M. C. Kaluza, *54 J pulses with 18 nm bandwidth from a diode-pumped chirped-pulse amplification laser system*, Optics Letters **41**, 5413 (2016).

[15] D. Strickland and G. Mourou, *Compression of amplified chirped optical pulses*, Optics Communications **56**, 219 (1985).

[16] F. Träger, *Handbook of Lasers and Optics*, Springer, 1st Ed. (2008).

[17] R. Boyd, *Nonlinear Optics*, Academic Press, 3rd Ed. (2008).

[18] A. Weiner, *Ultrafast Optics*, Wiley, 1st Ed. (2009).

[19] J. Körner, C. Vorholt, H. Liebetrau, M. Kahle, D. Klöpfel, R. Seifert, J. Hein, and M. C. Kaluza, *Measurement of temperature-dependent absorption and emission spectra of Yb:YAG, Yb:LuAG, and Yb:CaF_2 between 20° C and 200° C and predictions on their influence on laser performance*, Journal of the Optical Society of America B **29**, 2493 (2012).

[20] W. Koechner, *Solid-State Laser Engineering*, Springer, 6th Ed. (2006).

[21] S. A. Payne, L. L. Chase, L. K. Smith, W. L. Kway, and W. F. Krupke, *Infrared cross-section measurements for crystals doped with Er^{3+}, Tm^{3+}, and Ho^{3+}*, IEEE Journal of Quantum Electronics **28**, 2619 (1992).

[22] S. Chénais, F. Druon, S. Forget, F. Balembois, and P. Georges, *On thermal effects in solid-state lasers: The case of ytterbium-doped materials*, Progress in Quantum Electronics **30**, 89 (2006).

[23] I. Tamer, S. Keppler, M. Hornung, J. Körner, J. Hein, and M. C. Kaluza, *Spatio-temporal characterization of pump-induced wavefront aberrations in Yb^{3+}-doped materials*, Laser & Photonics Reviews **12**, 1700211 (2018).

[24] P. F. Moulton, *Spectroscopic and laser characteristics of Ti:Al_2O_3*, Journal of the Optical Society of America B **3**, 125 (1986).

[25] P. Mason, M. Divoký, K. Ertel, J. Pila, T. Butcher, M. Hanu, S. Banerjee, J. Phillips, J. Smith, M. De Vido, A. Lucianetti, C. Hernandez-Gomez, C. Edwards, T. Mocek, and J. Collier, *Kilowatt average power 100 J-level diode pumped solid state laser*, Optica **4**, 438 (2017).

[26] J. Körner, V. Jambunathan, J. Hein, R. Seifert, M. Loeser, M. Siebold, U. Schramm, P. Sikocinski, A. Lucianetti, T. Mocek, and M. C. Kaluza, *Spectroscopic characterization of Yb*$^{3+}$*-doped laser materials at cryogenic temperatures*, Applied Physics B **116**, 75 (2013).

[27] M. Siebold, S. Bock, U. Schramm, B. Xu, J. L. Doualan, P. Camy, and R. Moncorgé, *Yb:CaF*$_2$ *- a new old laser crystal*, Applied Physics B **97**, 327 (2009).

[28] T. Töpfer, *Diodengepumpte Hochleistungslaser*, Dissertation, Friedrich-Schiller-Universität Jena (2001).

[29] D. Ehrt and T. Töpfer, *Preparation, structure, and properties of Yb*$^{3+}$*-FP laser glass*, Proceedings of SPIE **4102** (2000).

[30] L. M. Frantz and J. S. Nodvik, *Theory of pulse propagation in a laser amplifier*, Journal of Applied Physics **34**, 2346 (1963).

[31] M. Siebold, J. Hein, M. Hornung, S. Podleska, M. C. Kaluza, S. Bock, and R. Sauerbrey, *Diode-pumped lasers for ultra-high peak power*, Applied Physics B **90**, 431 (2008).

[32] C. Manzoni and G. Cerullo, *Design criteria for ultrafast optical parametric amplifiers*, Journal of Optics **18**, 103501 (2016).

[33] S. Witte and K. S. E. Eikema, *Ultrafast optical parametric chirped-pulse amplification*, IEEE Journal of Selected Topics in Quantum Electronics **18**, 296 (2012).

[34] J. Bromage, S. W. Bahk, I. A. Begishev, C. Dorrer, M. J. Guardalben, B. N. Hoffman, J. B. Oliver, R. G. Roides, E. M. Schiesser, M. J. Shoup Iii, M. Spilatro, B. Webb, D. Weiner, and J. D. Zuegel, *Technology development for ultraintense all-OPCPA systems*, High Power Laser Science and Engineering **7**, e4 (2019).

[35] C. K. Lee, J. Y. Zhang, J. Huang, and C. L. Pan, *Generation of femtosecond laser pulses tunable from 380 nm to 465 nm via cascaded nonlinear optical mixing in a noncollinear optical parametric amplifier with a type-I phase matched BBO crystal*, Optics Express **11**, 1702 (2003).

[36] L. Hongjun, Z. Wei, C. Guofu, W. Yishan, C. Zhao, and R. Chi, *Investigation of spectral bandwidth of optical parametric amplification*, Applied Physics B **79**, 569 (2004).

[37] D. N. Schimpf, J. Rothhardt, J. Limpert, A. Tünnermann, and D. C. Hanna, *Theoretical analysis of the gain bandwidth for noncollinear parametric amplification of ultrafast pulses*, Journal of the Optical Society of America B **24**, 2837 (2007).

[38] B. Liu, R. Zhang, H. Liu, J. Ma, C. Zhu, and Q. Wang, *Investigation of spectral bandwidth of BBO-I phase matching non-collinear optical parametric amplification from visible to near-infrared*, Frontiers of Optoelectronics in China **1**, 101 (2008).

[39] J. Hult, *A fourth-order rungekutta in the interaction picture method for simulating supercontinuum generation in optical fibers*, Journal of Lightwave Technology **25**, 3770 (2007).

[40] M. D. Perry, T. Ditmire, and B. C. Stuart, *Self-phase modulation in chirped-pulse amplification*, Optics Letters **19**, 2149 (1994).

[41] F. Verluise, V. Laude, Z. Cheng, C. Spielmann, and P. Tournois, *Amplitude and phase control of ultrashort pulses by use of an acousto-optic programmable dispersive filter: pulse compression and shaping*, Optics Letters **25**, 575 (2000).

[42] R. M. Wood, *Laser induced damage thresholds and laser safety levels. Do the units of measurement matter?*, Optics & Laser Technology **29**, 517 (1998).

[43] B. C. Stuart, M. D. Feit, S. Herman, A. M. Rubenchik, B. W. Shore, and M. D. Perry, *Optical ablation by high-power short-pulse lasers*, Journal of the Optical Society of America B **13**, 459 (1996).

[44] J. F. Nye, *Physical Properties of Crystals: Their Representation by Tensors and Matrices*, Clarendon Press, 1st Ed. (1985).

[45] W. Martienssen and H. Warlimont, *Handbook of Condensed Matter and Materials Data*, Springer, 1st Ed. (2005).

[46] J. Burnett, *Stress-optical coefficients of 157 nm materials*, National Institute of Standards and Technology (2001).

[47] I. L. Snetkov, A. I. Yakovlev, and O. V. Palashov, *CaF_2, $BaF_2$and SrF_2 crystals optical anisotropy parameters*, Laser Physics Letters **12**, 095001 (2015).

[48] B. Lacroix, C. Genevois, J. L. Doualan, G. Brasse, A. Braud, P. Ruterana, P. Camy, E. Talbot, R. Moncorgé, and J. Margerie, *Direct imaging of rare-earth ion clusters in Yb:CaF_2*, Physical Review B **90**, 125124 (2014).

[49] F. Druon, S. Ricaud, D. N. Papadopoulos, A. Pellegrina, P. Camy, J. L. Doualan, R. Moncorgé, A. Courjaud, E. Mottay, and P. Georges, *On Yb:CaF*$_2$ *and Yb:SrF*$_2$*: review of spectroscopic and thermal properties and their impact on femtosecond and high power laser performance [Invited]*, Optical Materials Express **1**, 489 (2011).

[50] R. L. Aggarwal, D. J. Ripin, J. R. Ochoa, and T. Y. Fan, *Measurement of thermo-optic properties of* $Y_3Al_5O_{12}$, $Lu_3Al_5O_{12}$, $YAlO_3$, $LiYF_4$, $LiLuF_4$, BaY_2F_8, $KGd(WO_4)_2$, *and* $KY(WO_4)_2$ *laser crystals in the 80 - 300 K temperature range*, Journal of Applied Physics **98**, 103514 (2005).

[51] C. Jacinto, D. N. Messias, A. A. Andrade, S. M. Lima, M. L. Baesso, and T. Catunda, *Thermal lens and z-scan measurements: thermal and optical properties of laser glasses a review*, Journal of Non-Crystalline Solids **352**, 3582 (2006).

[52] R. Soulard, R. Moncorge, A. Zinoviev, K. Petermann, O. Antipov, and A. Brignon, *Nonlinear spectroscopic properties of Yb*$^{3+}$*-doped sesquioxides* Lu_2O_3 *and* Sc_2O_3, Optics Express **18**, 11173 (2010).

[53] R. Moncorgé, O. N. Eremeykin, J. L. Doualan, and O. L. Antipov, *Origin of athermal refractive index changes observed in Yb*$^{3+}$*-doped YAG and KGW*, Optics Communications **281**, 2526 (2008).

[54] M. Born and E. Wolf, *Principles of Optics: Electromagnetic Theory of Propagation, Interference and Diffraction of Light*, Pergamon Press, 7th Ed. (2000).

[55] O. L. Antipov, D. V. Bredikhin, O. N. Eremeykin, A. P. Savikin, E. V. Ivakin, and A. V. Sukhadolau, *Electronic mechanism for refractive-index changes in intensively pumped Yb:YAG laser crystals*, Optics Letters **31**, 763 (2006).

[56] O. L. Antipov, A. S. Kuzhelev, D. V. Chausov, and A. P. Zinovev, *Dynamics of refractive-index changes in a Nd:YAG laser crystal under excitation of Nd*$^{3+}$ *ions*, Journal of the Optical Society of America B **16**, 1072 (1999).

[57] D. F. Hotz, *Gain narrowing in a laser amplifier*, Applied Optics **4**, 527 (1965).

[58] Y. Chu, X. Liang, L. Yu, Y. Xu, L. Xu, L. Ma, X. Lu, Y. Liu, Y. Leng, R. Li, and Z. Xu, *High-contrast 2.0 petawatt Ti:sapphire laser system*, Optics Express **21**, 29231 (2013).

[59] T. Brabec and F. Krausz, *Nonlinear optical pulse propagation in the single-cycle regime*, Physical Review Letters **78**, 3282 (1997).

[60] M. P. Kalashnikov, E. Risse, H. Schönnagel, and W. Sandner, *Double chirped-pulse-amplification laser: a way to clean pulses temporally*, Optics Letters **30** (2005).

[61] A. Henig, S. Steinke, M. Schnurer, T. Sokollik, R. Horlein, D. Kiefer, D. Jung, J. Schreiber, B. M. Hegelich, X. Q. Yan, J. Meyer-ter Vehn, T. Tajima, P. V. Nickles, W. Sandner, and D. Habs, *Radiation-pressure acceleration of ion beams driven by circularly polarized laser pulses*, Physical Review Letters **103**, 245003 (2009).

[62] O. Lundh, F. Lindau, A. Persson, C. G. Wahlstrom, P. McKenna, and D. Batani, *Influence of shock waves on laser-driven proton acceleration*, Physical Review E **76**, 026404 (2007).

[63] S. Keppler, A. Sävert, J. Körner, M. Hornung, H. Liebetrau, J. Hein, and M. C. Kaluza, *The generation of amplified spontaneous emission in high-power CPA laser systems*, Laser & Photonics Reviews **10**, 264 (2016).

[64] N. V. Didenko, A. V. Konyashchenko, A. P. Lutsenko, and S. Y. Tenyakov, *Contrast degradation in a chirped-pulse amplifier due to generation of prepulses by postpulses*, Optics Express **16**, 3178 (2008).

[65] J. Bromage, C. Dorrer, and R. K. Jungquist, *Temporal contrast degradation at the focus of ultrafast pulses from high-frequency spectral phase modulation*, Journal of the Optical Society of America B **29**, 1125 (2012).

[66] C. Hooker, Y. Tang, O. Chekhlov, J. Collier, E. Divall, K. Ertel, S. Hawkes, B. Parry, and P. P. Rajeev, *Improving coherent contrast of petawatt laser pulses*, Optics Express **19**, 2193 (2011).

[67] H. Liebetrau, M. Hornung, A. Seidel, M. Hellwing, A. Kessler, S. Keppler, F. Schorcht, J. Hein, and M. C. Kaluza, *Ultra-high contrast frontend for high peak power fs-lasers at 1030 nm*, Optics Express **22**, 24776 (2014).

[68] D. N. Papadopoulos, P. Ramirez, K. Genevrier, L. Ranc, N. Lebas, A. Pellegrina, C. Le Blanc, P. Monot, L. Martin, J. P. Zou, F. Mathieu, P. Audebert, P. Georges, and F. Druon, *High-contrast 10 fs OPCPA-based front end for multi-PW laser chains*, Optics Letters **42**, 3530 (2017).

[69] A. Jullien, O. Albert, F. Burgy, G. Hamoniaux, J. P. Rousseau, J. P. Chambaret, F. Auge-Rochereau, G. Cheriaux, J. Etchepare, N. Minkovski, and S. M. Saltiel, *10^{-10} temporal contrast for femtosecond ultraintense lasers by cross-polarized wave generation*, Optics Letters **30**, 920 (2005).

[70] H. Liebetrau, M. Hornung, S. Keppler, M. Hellwing, A. Kessler, F. Schorcht, J. Hein, and M. C. Kaluza, *High contrast, 86 fs, 35 mJ pulses from a diode-pumped, Yb:glass, double-chirped-pulse amplification laser system*, Optics Letters **41**, 3006 (2016).

[71] C. Wandt, S. Klingebiel, S. Keppler, M. Hornung, M. Loeser, M. Siebold, C. Skrobol, A. Kessel, S. A. Trushin, Z. Major, J. Hein, M. C. Kaluza, F. Krausz, and S. Karsch, *Development of a Joule-class Yb:YAG amplifier and its implementation in a CPA system generating 1 TW pulses*, Laser & Photonics Reviews **8**, 875 (2014).

[72] M. Hornung, R. Bödefeld, M. Siebold, A. Kessler, M. Schnepp, R. Wachs, A. Sävert, S. Podleska, S. Keppler, J. Hein, and M. C. Kaluza, *Temporal pulse control of a multi-10 TW diode-pumped Yb:glass laser*, Applied Physics B **101**, 93 (2010).

[73] M. Hornung, R. Bodefeld, A. Kessler, J. Hein, and M. C. Kaluza, *Spectrally resolved and phase-sensitive far-field measurement for the coherent addition of laser pulses in a tiled grating compressor*, Optics Letters **35**, 2073 (2010).

[74] R. Bödefeld, M. Hornung, J. Hein, and M. C. Kaluza, *High precision elimination of angular chirp in CPA laser systems with large stretching factors or high bandwidth*, Applied Physics B **115**, 419 (2013).

[75] S. P. Mangles, C. D. Murphy, Z. Najmudin, A. G. Thomas, J. L. Collier, A. E. Dangor, E. J. Divall, P. S. Foster, J. G. Gallacher, C. J. Hooker, D. A. Jaroszynski, A. J. Langley, W. B. Mori, P. A. Norreys, F. S. Tsung, R. Viskup, B. R. Walton, and K. Krushelnick, *Monoenergetic beams of relativistic electrons from intense laser-plasma interactions*, Nature **431**, 535 (2004).

[76] H. Schwoerer, S. Pfotenhauer, O. Jackel, K. U. Amthor, B. Liesfeld, W. Ziegler, R. Sauerbrey, K. W. Ledingham, and T. Esirkepov, *Laser-plasma acceleration of quasi-monoenergetic protons from microstructured targets*, Nature **439**, 445 (2006).

[77] B. Dromey, S. Rykovanov, M. Yeung, R. Hörlein, D. Jung, D. C. Gautier, T. Dzelzainis, D. Kiefer, S. Palaniyppan, R. Shah, J. Schreiber, H. Ruhl, J. C. Fernandez, C. L. S. Lewis, M. Zepf, and B. M. Hegelich, *Coherent synchrotron emission from electron nanobunches formed in relativistic laserplasma interactions*, Nature Physics **8**, 804 (2012).

[78] A. J. Gonsalves, K. Nakamura, J. Daniels, C. Benedetti, C. Pieronek, T. C. H. de Raadt, S. Steinke, J. H. Bin, S. S. Bulanov, J. van Tilborg, C. G. R. Geddes, C. B. Schroeder, C. Toth, E. Esarey, K. Swanson, L. Fan-Chiang, G. Bagdasarov, N. Bobrova, V. Gasilov, G. Korn, P. Sasorov, and W. P. Leemans, *Petawatt laser guiding and electron beam acceleration to 8 GeV in a laser-heated capillary discharge waveguide*, Physical Review Letters **122**, 084801 (2019).

[79] J. Fuchs, P. Antici, E. dHumières, E. Lefebvre, M. Borghesi, E. Brambrink, C. A. Cecchetti, M. Kaluza, V. Malka, M. Manclossi, S. Meyroneinc, P. Mora, J. Schreiber,

T. Toncian, H. Pépin, and P. Audebert, *Laser-driven proton scaling laws and new paths towards energy increase*, Nature Physics **2**, 48 (2005).

[80] V. Malka, J. Faure, Y. A. Gauduel, E. Lefebvre, A. Rousse, and K. T. Phuoc, *Principles and applications of compact laser-plasma accelerators*, Nature Physics **4**, 447 (2008).

[81] H. Ebendorff-Heidepriem, W. Seeber, and D. Ehrt, *Spectroscopic properties of Nd^{3+} ions in phoshate glasses*, Journal of Non-Crystalline Solids **183**, 191 (1995).

[82] A. K. Cousins, *Temperature and thermal stress scaling in finite-length end-pumped laser rods*, IEEE Journal of Quantum Electronics **28**, 1057 (1992).

[83] M. Takeda, H. Ina, and S. Kobayashi, *Fourier-transform method of fringe-pattern analysis for computer-based topography and interferometry*, Journal of the Optical Society of America **72**, 156 (1982).

[84] *COMSOL,* https://www.comsol.com.

[85] *Hellma Materials, CaF$_2$ data sheet,* http://www.hellma-materials.com/text/993/en/laser-crystals.html.

[86] *Schott AG,* https://www.schott.com/english/index.html.

[87] *FLIR Systems, High speed thermal cameras,* http://www.flir.de/science/blog/details/?ID=74352.

[88] *FLIR Systems, R&D and science,* https://www.flir.com/discover/rd-science/use-low-cost-materials-to-increase-target-emissivity.

[89] B. E. Warren, *X-ray diffraction methods*, Journal of Applied Physics **12**, 375 (1941).

[90] R. C. Jones, *A new calculus for the treatment of optical systems*, Journal of the Optical Society of America **31**, 488 (1941).

[91] E. V. Ivakin, A. V. Sukhadolau, O. L. Antipov, and N. V. Kuleshov, *Transient grating measurements of refractive-index changes in intensively pumped Yb-doped laser crystals*, Applied Physics B **86**, 315 (2006).

[92] D. N. Papadopoulos, J. P. Zou, C. Le Blanc, G. Chériaux, P. Georges, F. Druon, G. Mennerat, P. Ramirez, L. Martin, A. Fréneaux, A. Beluze, N. Lebas, P. Monot, F. Mathieu, and P. Audebert, *The Apollon 10 PW laser: experimental and theoretical investigation of the temporal characteristics*, High Power Laser Science and Engineering **4**, e34 (2016).

[93] L. Antonucci, J. P. Rousseau, A. Jullien, B. Mercier, V. Laude, and G. Cheriaux, *14-fs high temporal quality injector for ultra-high intensity laser*, Optics Communications **282**, 1374 (2009).

[94] J. Körner, F. Yue, J. Hein, and M. C. Kaluza, *Spatially and temporally resolved temperature measurement in laser media*, Optics Letters **41**, 2525 (2016).

[95] H. Chi, K. A. Dehne, C. M. Baumgarten, H. Wang, L. Yin, B. A. Reagan, and J. J. Rocca, *In situ 3-D temperature mapping of high average power cryogenic laser amplifiers*, Optics Express **26**, 5240 (2018).

[96] S. Keppler, C. Wandt, M. Hornung, R. Böefeld, A. Kessler, A. Sävert, M. Hellwing, F. Schorcht, J. Hein, and M. C. Kaluza, *Multipass amplifiers of POLARIS*, Proceedings of SPIE **8780**, 1 (2013).

[97] I. Tamer, S. Keppler, J. Körner, M. Hornung, M. Hellwing, F. Schorcht, J. Hein, and M. C. Kaluza, *Modeling of the 3D spatio-temporal thermal profile of joule-class Yb*$^{3+}$*-based laser amplifiers*, High Power Laser Science and Engineering **7**, e42 (2019).

[98] A. Jullien, L. Canova, O. Albert, D. Boschetto, L. Antonucci, Y. H. Cha, J. P. Rousseau, P. Chaudet, G. Chériaux, J. Etchepare, S. Kourtev, N. Minkovski, and S. M. Saltiel, *Spectral broadening and pulse duration reduction during cross-polarized wave generation: influence of the quadratic spectral phase*, Applied Physics B **87**, 595 (2007).

[99] M. Kaumanns, V. Pervak, D. Kormin, V. Leshchenko, A. Kessel, M. Ueffing, Y. Chen, and T. Nubbemeyer, *Multipass spectral broadening of 18 mJ pulses compressible from 1.3 ps to 41 fs*, Optics Letters **43**, 5877 (2018).

[100] J. Schreiber, C. Bellei, S. P. Mangles, C. Kamperidis, S. Kneip, S. R. Nagel, C. A. Palmer, P. P. Rajeev, M. J. Streeter, and Z. Najmudin, *Complete temporal characterization of asymmetric pulse compression in a laser wakefield*, Physical Review Letters **105**, 235003 (2010).

[101] S. Y. Mironov, J. Wheeler, R. Gonin, G. Cojocaru, R. Ungureanu, R. Banici, M. Serbanescu, R. Dabu, G. Mourou, and E. A. Khazanov, *100 J-level pulse compression for peak power enhancement*, Quantum Electronics **47**, 173 (2017).

[102] G. Mourou, S. Mironov, E. Khazanov, and A. Sergeev, *Single cycle thin film compressor opening the door to zeptosecond-exawatt physics*, The European Physical Journal Special Topics **223**, 1181 (2014).

[103] V. N. Ginzburg, I. V. Yakovlev, A. S. Zuev, A. P. Korobeynikova, A. A. Kochetkov, A. A. Kuz'min, S. Y. Mironov, A. A. Shaykin, I. A. Shaykin, and E. A. Khazanov,

Compression after compressor: threefold shortening of 200-TW laser pulses, Quantum Electronics **49**, 299 (2019).

[104] L. Fornasari, F. Floris, M. Patrini, D. Comoretto, and F. Marabelli, *Demonstration of fluorescence enhancement via Bloch surface waves in all-polymer multilayer structures*, Physical Chemistry Chemical Physics **18**, 14086 (2016).

[105] K. Iiyama, T. Ishida, Y. Ono, T. Maruyama, and T. Yamagishi, *Fabrication and characterization of amorphous polyethylene terephthalate optical waveguides*, IEEE Photonics Technology Letters **23**, 275 (2011).

[106] G. Beadie, M. Brindza, R. A. Flynn, A. Rosenberg, and J. S. Shirk, *Refractive index measurements of poly(methyl methacrylate) (PMMA) from 0.4-1.6 μm*, Applied Optics **54**, F139 (2015).

[107] V. Kumar, P. K. Goyal, S. Mahendia, R. Gupta, T. Sharma, and S. Kumar, *Tuning of the refractive index and optical band gap of CR-39 polymers by heating*, Radiation Effects and Defects in Solids **166**, 109 (2011).

[108] R. Adair, L. L. Chase, and S. A. Payne, *Nonlinear refractive-index measurements of glasses using three-wave frequency mixing*, Journal of the Optical Society of America B **4**, 875 (1987).

[109] D. Milam, *Review and assessment of measured values of the nonlinear refractive-index coefficient of fused silica*, Applied Optics **37**, 546 (1998).

[110] D. Wang, Y. Leng, and Z. Xu, *Measurement of nonlinear refractive index coefficient of inert gases with hollow-core fiber*, Applied Physics B **111**, 447 (2013).

[111] A. Börzsönyi, Z. Heiner, A. P. Kovacs, M. P. Kalashnikov, and K. Osvay, *Measurement of pressure dependent nonlinear refractive index of inert gases*, Optics Express **18**, 25847 (2010).

[112] M. B. Schwab, A. Sävert, O. Jäckel, J. Polz, M. Schnell, T. Rinck, L. Veisz, M. Möller, P. Hansinger, G. G. Paulus, and M. C. Kaluza, *Few-cycle optical probe-pulse for investigation of relativistic laser-plasma interactions*, Applied Physics Letters **103**, 191118 (2013).

[113] W. T. Mohamed, J. An, and D. E. Kim, *Selected Topics on Optical Fiber Technology: Generation of Few Cycle Femtosecond Pulses via Supercontinuum in a Gas-Filled Hollow-Core Fiber*, IntechOpen, 1st Ed. (2011).

[114] S. Bashir, M. S. Rafique, W. Husinsky, A. Hobro, and B. Lendl, *Atomic force microscopy and Raman scattering studies of femtosecond laser-induced nanohillocks on CR-39*, Nuclear Instruments and Methods in Physics Research Section B: Beam Interactions with Materials and Atoms **267**, 3606 (2009).

[115] D. Pietroy, Y. Di Maio, B. Moine, E. Baubeau, and E. Audouard, *Femtosecond laser volume ablation rate and threshold measurements by differential weighing*, Optics Express **20**, 29900 (2012).

[116] M. Balu, J. Hales, D. Hagan, and E. Van Stryland, *White-light continuum z-scan technique for nonlinear materials characterization*, Optics Express **12**, 3820 (2004).

[117] M. Yin, H. P. Li, S. H. Tang, and W. Ji, *Determination of nonlinear absorption and refraction by single z-scan method*, Applied Physics B: Lasers and Optics **70**, 587 (2000).

[118] S. Venugopal Rao, N. K. M. Naga Srinivas, and D. Narayana Rao, *Nonlinear absorption and excited state dynamics in Rhodamine B studied using z-scan and degenerate four wave mixing techniques*, Chemical Physics Letters **361**, 439 (2002).

[119] R. Sutherland, *Handbook of Nonlinear Optics*, Marcel Dekker, 2nd Ed. (2003).

[120] S. V. Rao, N. K. M. N. Srinivas, D. N. Rao, L. Giribabu, B. G. Maiya, R. Philip, and G. R. Kumar, *Studies of third-order optical nonlinearity and nonlinear absorption in tetra tolyl porphyrins using degenerate four wave mixing and z-scan*, Optics Communications **182**, 255 (2000).

[121] M. Samoc, A. Samoc, B. Luther-Davies, Z. Bao, L. Yu, B. Hsieh, and U. Scherf, *Femtosecond z-scan and degenerate four-wave mixing measurements of real and imaginary parts of the third-order nonlinearity of soluble conjugated polymers*, Journal of the Optical Society of America B **15**, 817 (1998).

[122] J. Wheeler, *Efficient extreme light compression and its application*, Extreme Light Scientific & Socio-Economic Outlook - IZEST Annual Meeting (2016).

[123] C. Dorrer, R. G. Roides, J. Bromage, and J. D. Zuegel, *Self-phase modulation compensation in a regenerative amplifier using cascaded second-order nonlinearities*, Optics Letters **39**, 4466 (2014).

[124] A. Henig, D. Kiefer, K. Markey, D. C. Gautier, K. A. Flippo, S. Letzring, R. P. Johnson, T. Shimada, L. Yin, B. J. Albright, K. J. Bowers, J. C. Fernandez, S. G. Rykovanov, H. C. Wu, M. Zepf, D. Jung, V. Liechtenstein, J. Schreiber, D. Habs, and B. M.

Hegelich, *Enhanced laser-driven ion acceleration in the relativistic transparency regime*, Physical Review Letters **103**, 045002 (2009).

[125] A. J. Mackinnon, Y. Sentoku, P. K. Patel, D. W. Price, S. Hatchett, M. H. Key, C. Andersen, R. Snavely, and R. R. Freeman, *Enhancement of proton acceleration by hot-electron recirculation in thin foils irradiated by ultraintense laser pulses*, Physical Review Letters **88**, 215006 (2002).

[126] M. Hornung, H. Liebetrau, A. Seidel, S. Keppler, A. Kessler, J. Körner, M. Hellwing, F. Schorcht, D. Klöpfel, A. K. Arunachalam, G. A. Becker, A. Sävert, J. Polz, J. Hein, and M. C. Kaluza, *The all-diode-pumped laser system POLARIS – an experimentalists tool generating ultra-high contrast pulses with high energy*, High Power Laser Science and Engineering **2**, e20 (2014).

[127] Y. Huang, C. Zhang, Y. Xu, D. Li, Y. Leng, R. Li, and Z. Xu, *Ultrashort pulse temporal contrast enhancement based on noncollinear optical-parametric amplification*, Optics Letters **36**, 781 (2011).

[128] J. M. Mikhailova, A. Buck, A. Borot, K. Schmid, C. Sears, G. D. Tsakiris, F. Krausz, and L. Veisz, *Ultra-high-contrast few-cycle pulses for multipetawatt-class laser technology*, Optics Letters **36**, 3145 (2011).

[129] S. Fourmaux, S. Payeur, S. Buffechoux, P. Lassonde, C. St-Pierre, F. Martin, and J. C. Kieffer, *Pedestal cleaning for high laser pulse contrast ratio with a 100 TW class laser system*, Optics Express **19**, 8486 (2011).

[130] H. C. Kapteyn, M. M. Murnane, A. Szoke, and R. W. Falcone, *Prepulse energy suppression for high-energy ultrashort pulses using self-induced plasma shuttering*, Optics Letters **16**, 490 (1991).

[131] B. Dromey, S. Kar, M. Zepf, and P. Foster, *The plasma mirror – A subpicosecond optical switch for ultrahigh power lasers*, Review of Scientific Instruments **75**, 645 (2004).

[132] C. Thaury, F. Quéré, J. P. Geindre, A. Levy, T. Ceccotti, P. Monot, M. Bougeard, F. Réau, P. d'Oliveira, P. Audebert, R. Marjoribanks, and P. Martin, *Plasma mirrors for ultrahigh-intensity optics*, Nature Physics **3**, 424 (2007).

[133] C. Ziener, P. S. Foster, E. J. Divall, C. J. Hooker, M. H. R. Hutchinson, A. J. Langley, and D. Neely, *Specular reflectivity of plasma mirrors as a function of intensity, pulse duration, and angle of incidence*, Journal of Applied Physics **93**, 768 (2003).

[134] C. Rödel, M. Heyer, M. Behmke, M. Kübel, O. Jäckel, W. Ziegler, D. Ehrt, M. C. Kaluza, and G. G. Paulus, *High repetition rate plasma mirror for temporal contrast*

enhancement of terawatt femtosecond laser pulses by three orders of magnitude, Applied Physics B **103**, 295 (2010).

[135] G. Doumy, F. Quere, O. Gobert, M. Perdrix, P. Martin, P. Audebert, J. C. Gauthier, J. P. Geindre, and T. Wittmann, *Complete characterization of a plasma mirror for the production of high-contrast ultraintense laser pulses*, Physical Review E **69**, 026402 (2004).

[136] A. Macchi and C. Benedetti, *Ion acceleration by radiation pressure in thin and thick targets*, Nuclear Instruments and Methods in Physics Research Section A: Accelerators, Spectrometers, Detectors and Associated Equipment **620**, 41 (2010).

[137] A. Macchi, M. Borghesi, and M. Passoni, *Ion acceleration by superintense laser-plasma interaction*, Reviews of Modern Physics **85**, 751 (2013).

[138] T. Esirkepov, M. Borghesi, S. V. Bulanov, G. Mourou, and T. Tajima, *Highly efficient relativistic-ion generation in the laser-piston regime*, Physical Review Letters **92**, 175003 (2004).

[139] M. Passoni, L. Bertagna, and A. Zani, *Target normal sheath acceleration: theory, comparison with experiments and future perspectives*, New Journal of Physics **12**, 045012 (2010).

[140] H. Daido, M. Nishiuchi, and A. S. Pirozhkov, *Review of laser-driven ion sources and their applications*, Reports on Progress in Physics **75**, 056401 (2012).

[141] K. Zeil, S. D. Kraft, S. Bock, M. Bussmann, T. E. Cowan, T. Kluge, J. Metzkes, T. Richter, R. Sauerbrey, and U. Schramm, *The scaling of proton energies in ultrashort pulse laser plasma acceleration*, New Journal of Physics **12**, 045015 (2010).

[142] W. P. Leemans, B. Nagler, A. J. Gonsalves, C. Tóth, K. Nakamura, C. G. R. Geddes, E. Esarey, C. B. Schroeder, and S. M. Hooker, *GeV electron beams from a centimetre-scale accelerator*, Nature Physics **2**, 696 (2006).

[143] C. G. Geddes, C. S. Toth, J. Van Tilborg, E. Esarey, C. B. Schroeder, D. Bruhwiler, C. Nieter, J. Cary, and W. P. Leemans, *High-quality electron beams from a laser wakefield accelerator using plasma-channel guiding*, Nature **431**, 538 (2004).

[144] L. Gremillet, F. Amiranoff, S. D. Baton, J. C. Gauthier, M. Koenig, E. Martinolli, F. Pisani, G. Bonnaud, C. Lebourg, C. Rousseaux, C. Toupin, A. Antonicci, D. Batani, A. Bernardinello, T. Hall, D. Scott, P. Norreys, H. Bandulet, and H. Pépin, *Time-resolved observation of ultrahigh intensity laser-produced electron jets propagating through transparent solid targets*, Physical Review Letters **83**, 5015 (1999).

[145] B. T. Vu, O. L. Landen, and A. Szoke, *Time-resolved backside optical probing of picosecond-laser-pulse-produced plasma in solid materials*, Physical Review E **47**, 2768 (1993).

[146] R. Evans, A. D. Badger, F. Fallies, M. Mahdieh, T. A. Hall, P. Audebert, J. Geindre, J. Gauthier, A. Mysyrowicz, G. Grillon, and A. Antonetti, *Time- and space-resolved optical probing of femtosecond-laser-driven shock waves in aluminum*, Physical Review Letters **77**, 3359 (1996).

[147] S. Feister, J. A. Nees, J. T. Morrison, K. D. Frische, C. Orban, E. A. Chowdhury, and W. M. Roquemore, *A novel femtosecond-gated, high-resolution, frequency-shifted shearing interferometry technique for probing pre-plasma expansion in ultra-intense laser experiments*, Review of Scientific Instruments **85**, 11D602 (2014).

[148] J. P. Geindre, P. Audebert, A. Rousse, F. Fallies, J. C. Gauthier, A. Mysyrowicz, A. D. Santos, G. Hamoniaux, and A. Antonetti, *Frequency-domain interferometer for measuring the phase and amplitude of a femtosecond pulse probing a laser-produced plasma*, Optics Letters **19**, 1997 (1994).

[149] F. Cattani, A. Kim, D. Anderson, and M. Lisak, *Threshold of induced transparency in the relativistic interaction of an electromagnetic wave with overdense plasmas*, Physical Review E **62**, 1234 (2000).

[150] G. A. Becker, M. B. Schwab, R. Lötzsch, H. Schlenvoigt, M. Rehwald, D. Klöpfel, J. Polz, A. Sävert, U. Schramm, and M. C. Kaluza, *Laser-Ion-Acceleration using Water Droplets and Optical Probing @ JETI40*, IOQ Seminar, Friedrich Schiller University (2016).

[151] U. Teubner and P. Gibbon, *High-order harmonics from laser-irradiated plasma surfaces*, Reviews of Modern Physics **81**, 445 (2009).

[152] G. A. Becker, M. B. Schwab, R. Lötzsch, S. Tietze, D. Klöpfel, M. Rehwald, H. Schlenvoigt, A. Sävert, U. Schramm, M. Zepf, and M. C. Kaluza, *Characterization of laser-driven proton acceleration from water microdroplets*, Scientific Reports **9**, 17169 (2019).

[153] D. Polli, D. Brida, S. Mukamel, G. Lanzani, and G. Cerullo, *Effective temporal resolution in pump-probe spectroscopy with strongly chirped pulses*, Physical Review A **82**, 053809 (2010).

[154] S. Keppler, R. Bödefeld, M. Hornung, A. Sävert, J. Hein, and M. C. Kaluza, *Prepulse suppression in a multi-10-TW diode-pumped Yb:glass laser*, Applied Physics B **104**, 11 (2011).

[155] S. Keppler, M. Hornung, P. Zimmermann, H. Liebetrau, M. Hellwing, J. Hein, and M. C. Kaluza, *Tunable filters for precise spectral gain control in ultra-short-pulse laser systems*, Optics Letters **41**, 4708 (2016).

[156] A. Dubietis, G. Tamoauskas, R. uminas, V. Jukna, and A. Couairon, *Ultrafast supercontinuum generation in bulk condensed media*, Lithuanian Journal of Physics **57**, 113 (2017).

[157] A. Couairon and A. Mysyrowicz, *Femtosecond filamentation in transparent media*, Physics Reports **441**, 47 (2007).

[158] L. Indra, F. Batysta, P. Hribek, J. Novak, Z. Hubka, J. T. Green, R. Antipenkov, R. Boge, J. A. Naylon, P. Bakule, and B. Rus, *Picosecond pulse generated supercontinuum as a stable seed for OPCPA*, Optics Letters **42**, 843 (2017).

[159] M. Bradler, P. Baum, and E. Riedle, *Femtosecond continuum generation in bulk laser host materials with sub-μJ pump pulses*, Applied Physics B **97**, 561 (2009).

[160] M. Vengris, N. Garejev, G. Tamosauskas, A. Cepenas, L. Rimkus, A. Varanavicius, V. Jukna, and A. Dubietis, *Supercontinuum generation by co-filamentation of two color femtosecond laser pulses*, Scientific Reports **9**, 9011 (2019).

[161] J. B. Ashcom, R. R. Gattass, C. B. Schaffer, and E. Mazur, *Numerical aperture dependence of damage and supercontinuum generation from femtosecond laser pulses in bulk fused silica*, Journal of the Optical Society of America B **23**, 2317 (2006).

[162] M. Pergament, M. Kellert, K. Kruse, J. Wang, G. Palmer, L. Wissmann, U. Wegner, and M. J. Lederer, *High power burst-mode optical parametric amplifier with arbitrary pulse selection*, Optics Express **22**, 22202 (2014).

[163] S. Xu, J. Qiu, T. Jia, C. Li, H. Sun, and Z. Xu, *Femtosecond laser ablation of crystals SiO_2 and YAG*, Optics Communications **274**, 163 (2007).

[164] R. C. Eckardt, H. Masuda, Y. X. Fan, and R. L. Byer, *Absolute and relative nonlinear optical coefficients of KDP, KD*P, BaB_2O_4, $LiIO_3$, MgO:$LiNbO_3$, and KTP measured by phase-matched second-harmonic generation*, IEEE Journal of Quantum Electronics **26**, 922 (1990).

[165] D. Nikogosyan, *Nonlinear Optical Crystals: A Complete Survey*, Springer, 1st Ed. (2005).

[166] R. Akbari and A. Major, *Optical, spectral and phase-matching properties of BIBO, BBO and LBO crystals for optical parametric oscillation in the visible and near-infrared wavelength ranges*, Laser Physics **23**, 035401 (2013).

[167] J. Rothhardt, S. Demmler, S. Hadrich, J. Limpert, and A. Tunnermann, *Octave-spanning OPCPA system delivering CEP-stable few-cycle pulses and 22 W of average power at 1 MHz repetition rate*, Optics Express **20**, 10870 (2012).

[168] T. Stanislauskas, I. Balinas, V. Tamuliene, R. Budrinas, and A. Varanaviius, *Analysis of parametric fluorescence amplified in a noncollinear optical parametric amplifier pumped by the second harmonic of a femtosecond Yb:KGW laser*, Lithuanian Journal of Physics **56**, 1 (2016).

[169] G. Wu, W. Li, E. Wu, and H. Zeng, *Generation of correlated UV and visible rainbows*, Optics Express **18**, 1000 (2010).

[170] J. Bromage, J. Rothhardt, S. Hadrich, C. Dorrer, C. Jocher, S. Demmler, J. Limpert, A. Tunnermann, and J. D. Zuegel, *Analysis and suppression of parasitic processes in noncollinear optical parametric amplifiers*, Optics Express **19**, 16797 (2011).

[171] K. Nakagawa, A. Iwasaki, Y. Oishi, R. Horisaki, A. Tsukamoto, A. Nakamura, K. Hirosawa, H. Liao, T. Ushida, K. Goda, F. Kannari, and I. Sakuma, *Sequentially timed all-optical mapping photography (STAMP)*, Nature Photonics **8**, 695 (2014).

[172] T. Suzuki, F. Isa, L. Fujii, K. Hirosawa, K. Nakagawa, K. Goda, I. Sakuma, and F. Kannari, *Sequentially timed all-optical mapping photography (STAMP) utilizing spectral filtering*, Optics Express **23**, 30512 (2015).

[173] T. Oksenhendler, S. Coudreau, N. Forget, V. Crozatier, S. Grabielle, R. Herzog, O. Gobert, and D. Kaplan, *Self-referenced spectral interferometry*, Applied Physics B **99**, 7 (2010).

[174] A. Shirakawa, I. Sakane, and T. Kobayashi, *Pulse-front-matched optical parametric amplification for sub-10-fs pulse generation tunable in the visible and near infrared*, Optics Letters **23**, 1292 (1998).

[175] A. Baltuska, T. Fuji, and T. Kobayashi, *Visible pulse compression to 4 fs by optical parametric amplification and programmable dispersion control*, Optics Letters **27**, 306 (2002).

[176] T. Kobayashi and A. Baltuska, *Sub-5 fs pulse generation from a noncollinear optical parametric amplifier*, Measurement Science and Technology **13**, 1671 (2002).

[177] C. Manzoni, D. Polli, and G. Cerullo, *Two-color pump-probe system broadly tunable over the visible and the near infrared with sub-30 fs temporal resolution*, Review of Scientific Instruments **77**, 023103 (2006).

[178] C. Homann, C. Schriever, P. Baum, and E. Riedle, *Octave wide tunable UV-pumped NOPA: pulses down to 20 fs at 0.5 MHz repetition rate*, Optics Express **16**, 5746 (2008).

[179] J. Bromage, C. Dorrer, and J. D. Zuegel, *Angular-dispersion-induced spatiotemporal aberrations in noncollinear optical parametric amplifiers*, Optics Letters **35**, 2251 (2010).

[180] M. Emons, A. Steinmann, T. Binhammer, G. Palmer, M. Schultze, and U. Morgner, *Sub-10-fs pulses from a MHz-NOPA with pulse energies of 0.4 µJ*, Optics Express **18**, 1191 (2010).

[181] R. Antipenkov, A. Varanavicius, A. Zaukevicius, and A. P. Piskarskas, *Femtosecond Yb:KGW MOPA driven broadband NOPA as a frontend for TW few-cycle pulse systems*, Optics Express **19**, 3519 (2011).

[182] H. Shen, S. Adachi, T. Horio, and T. Suzuki, *Two-color deep-ultraviolet 40-fs pulses based on parametric amplification at 100 kHz*, Optics Express **19**, 22637 (2011).

[183] C. Homann, M. Breuer, F. Setzpfandt, T. Pertsch, and E. Riedle, *Seeding of picosecond and femtosecond optical parametric amplifiers by weak single mode continuous lasers*, Optics Express **21**, 730 (2013).

[184] R. Riedel, M. Schulz, M. J. Prandolini, A. Hage, H. Hoppner, T. Gottschall, J. Limpert, M. Drescher, and F. Tavella, *Long-term stabilization of high power optical parametric chirped-pulse amplifiers*, Opt Express **21**, 28987 (2013).

[185] M. Bradler and E. Riedle, *Sub-20 fs µJ-energy pulses tunable down to the near-UV from a 1 MHz Yb-fiber laser system*, Optics Letters **39**, 2588 (2014).

[186] T. Stanislauskas, R. Budriunas, R. Antipenkov, A. Zaukevicius, J. Adamonis, A. Michailovas, L. Giniunas, R. Danielius, A. Piskarskas, and A. Varanavicius, *Table top TW-class OPCPA system driven by tandem femtosecond Yb:KGW and picosecond Nd:YAG lasers*, Optics Express **22**, 1865 (2014).

[187] R. Budriunas, T. Stanislauskas, and A. Varanaviius, *Passively CEP-stabilized frontend for few cycle terawatt OPCPA system*, Journal of Optics **17**, 094008 (2015).

[188] L. Lepetit, G. Chériaux, and M. Joffre, *Linear techniques of phase measurement by femtosecond spectral interferometry for applications in spectroscopy*, Journal of the Optical Society of America B **12**, 2467 (1995).

[189] *Schott AG, OG550 data sheet,* Optical Filter Glass Properties - 2014.

[190] C. P. Singh and K. S. Bindra, *Saturation and reverse saturable absorption in semiconductor doped glass and its application to parallel logic gates*, Optical and Quantum Electronics **47**, 3313 (2015).

[191] C. B. Schroeder, E. Esarey, C. G. R. Geddes, C. Benedetti, and W. P. Leemans, *Physics considerations for laser-plasma linear colliders*, Physical Review Special Topics - Accelerators and Beams **13**, 101301 (2010).

Publications

I. Tamer, S. Keppler, M. Hornung, J. Körner, J. Hein, and M. C. Kaluza, *Spatio-temporal characterization of pump–induced wavefront aberrations in Yb^{3+}-doped materials*, Laser & Photonics Reviews **12**, 1700211 (2018).

I. Tamer, S. Keppler, J. Körner, M. Hornung, M. Hellwing, F. Schorcht, J. Hein, and M. C. Kaluza, *Modeling of the 3D spatio-temporal thermal profile of joule-class Yb^{3+}-based laser amplifiers*, High Power Laser Science and Engineering **7**, E42 (2019).

I. Tamer, M. Hornung, L. Lukas, S. Keppler, M. Hellwing, R. Van Hull, J. Hein, M. Zepf, and M. C. Kaluza, *Characterization and application of nonlinear plastic materials for post-CPA pulse compression*, submitted to Optics Letters (2020).

I. Tamer, M. Hellwing, Y. Azamoum, M. Hornung, S. Keppler, F. Schorcht, J. Hein, and M. C. Kaluza, *Few-cycle fs-pumped NOPA with passive ultrabroadband spectral shaping*, submitted to Optics Express (2020).

S. Keppler, N. Elkina, G. A. Becker, I. Tamer, M. Mäusezahl, M. Hornung, C. Rödel, M. Zepf, and M. C. Kaluza, *Contrast dependent intensity scaling of laser-driven proton acceleration in the TNSA-regime*, in preparation.

Conference Proceedings

I. Tamer, S. Keppler, M. Hornung, J. Körner, J. Hein, and M. C. Kaluza, *Spatio-temporal characterization of pump-induced wavefront aberrations in Yb^{3+}-doped materials*, International Committee of Ultrahigh Intensity Lasers (ICUIL), Lindau, Germany (09/2018).

I. Tamer, S. Keppler, J. Körner, M. Hornung, M. Hellwing, F. Schorcht, J. Hein, and M. C. Kaluza, *Pump-induced wavefront aberrations in Yb^{3+}-doped materials*, High Intensity Lasers and High Field Phenomena (HILAS), Strasbourg, France (03/2018).

Ehrenwörtliche Erklärung

Ich erkläre hiermit ehrenwörtlich, dass ich die vorliegende Arbeit selbständig, ohne unzulässige Hilfe Dritter und ohne Benutzung anderer als der angegebenen Hilfsmittel und Literatur angefertigt habe. Die aus anderen Quellen direkt oder indirekt übernommenen Daten und Konzepte sind unter Angabe der Quelle gekennzeichnet.

Weitere Personen waren an der inhaltlich-materiellen Erstellung der vorliegenden Arbeit nicht beteiligt. Insbesondere habe ich hierfür nicht die entgeltliche Hilfe von Vermittlungs-bzw. Beratungsdiensten (Promotionsberater oder andere Personen) in Anspruch genommen. Niemand hat von mir unmittelbar oder mittelbar geldwerte Leistungen für Arbeiten erhalten, die im Zusammenhang mit dem Inhalt der vorgelegten Dissertation stehen.

Die Arbeit wurde bisher weder im In- noch im Ausland in gleicher oder ähnlicher Form einer anderen Prüfungsbehörde vorgelegt.

Die geltende Promotionsordnung der Physikalisch-Astronomischen Fakultät ist mir bekannt.

Ich versichere ehrenwörtlich, dass ich nach bestem Wissen die reine Wahrheit gesagt und nichts verschwiegen habe.

Jena, den 6.12.2019
Issa Tamer

Danksagung

An dieser Stelle möchte ich mich bei allen bedanken, die zum Gelingen dieser Arbeit beigetragen haben. Mein besonderer Dank gilt

- **Prof. Dr. Malte C. Kaluza** für die Vergabe des interessanten Themas sowie für seine Zeit, die er schon während dieser Jahren verbraucht hat, um meine wichtige (und unwichtige) Fragen zu beantworten. Bevor ich nach Jena angekommen bin, konnte ich mich nicht vorstellen, dass ich mit solchen interessanten Projekten mich beschäftigen könnte, als was die relativistische Laserphysik Forschungsgruppe anbietet.
- **Dr. Marco Hornung** für seine Betreuung und fantastische Arbeitseinstellung. Man findet kaum einen Mensch, der sich mehrmals darum kümmert, zu überprüfen, ob ein Doktorand mit seinem Projekt völlig zufrieden ist.
- **Prof. Dr. Matt Zepf** für sein offenes Ohr und seine Hilfsbereitschaft. Ich war immer sehr gespannt, meine gute sowie schlechte Ideen mit ihm zu diskutieren und verbessern.
- **Dr. Sebastian Keppler** für die kontinuierliche Unterstützung und viele Erklärungen, wann es insbesondere mal wieder länger gedauert hat.
- **Marco Hellwing** für seine umfassende Expertise, die er mit mir geteilt hat.
- **Georg Becker** für die vielen tollen Empfehlungen und lustigen Gesprächen.
- **Den gesamten POLARIS- und RLP-Arbeitsgruppen** inklusiv Frank Schorcht, Alexander Kessler, Dr. Jörg Körner, Dr. Joachim Hein, Yasmina Azamoum, Matthew Schwab sowie alle anderen für das angenehme Arbeitsklima. Die gute Zusammenarbeit der letzen Jahre schätze ich sehr.
- **Max Opolka und Florian Seifert** für die letzten Jahre, die zu einer unvergesslichen Zeit für mich wurden, sowie für die dauerhafte Mühe sie gegeben haben, mir deutsche kultur beizubringen.
- **alla mia ragazza Letizia D'Amico** per l'insostituibile compagnia (e letizia) che mi ha regalato negli ultimi cinque anni e in anticipo per gli anni a venire.

Most of all, I would like to thank my mother Marlene Hanna and brother Issam Tamer, who have 100% supported me throughout all of my endeavors, regardless of how crazy or difficult they were (even if it meant traveling over 5000 miles, across an ocean, to a country where I had no prior knowledge of the native language, just to be a part of the field I'm passionate about). I'm greatly indebted to you both.